ADDITIVE MANUFACTURING FOR RF ELECTRONICS PACKAGING

By

Christopher Ryan Oakley

A DISSERTATION

Submitted to
Michigan State University
in partial fulfillment of the requirements
for the degree of

Electrical Engineering – Doctor of Philosophy

2020

ABSTRACT

ADDITIVE MANUFACTURING FOR RF ELECTRONICS PACKAGING

By

Christopher Ryan Oakley

From the development of the first wireless communications systems, there has been growing demand for ever smaller, lighter weight, lower cost devices. Electronics packaging techniques have evolved with this demand, with a variety of process to create compact, high functional density systems. Recent developments in additive manufacturing technologies have enabled the application of low cost, rapid fabrication techniques to the development of radio frequency (RF) electronics. Using available direct-write technologies such as inkjet and aerosol jet printing, a wide range of electronic components, from RF devices to sensors and antennas, can be combined to form functional systems quickly and affordably.

The purpose of this thesis is to investigate the application of a variety of additive manufacturing process to the packaging of radio frequency electronics operating into the mm-wave (30 GHz to 300 GHz) frequency range and beyond. Applications of aerosol jet printing for fabrication of passive circuit components operating in the THz frequency regime have been demonstrated, as well as limitations of this process, and potential improvements. A process for rapid prototyping of RF circuits operating in the X-band (8 GHz to 12 GHz), combining commercially available materials and packaged components, was developed. Wide-bandwidth printed interconnections to devices have been demonstrated, enabling the packaging of bare integrated circuits with very low loss, and low cost. Finally, a self-packaging process combining multiple additive manufacturing techniques is demonstrated for fabrication of a Ku-band (12 GHz - 18 GHz) transmitter. These packaging techniques pave the way for low cost fabrication of circuits and systems, while minimizing unwanted parasitic effects, enabling efficient operation beyond 100 GHz.

For my parents, Robert and Patricia.

ACKNOWLEDGEMENTS

This work is funded by the Department of Energy's Kansas City National Security Campus, operated by Honeywell Federal Manufacturing & Technologies, LLC under contract number DE-NA0002839.

TABLE OF CONTENTS

LIST OF TABLES

LIST OF FIGURES

CHAPTER 1

INTRODUCTION

1.1 Electronics Packaging Processes

From the invention of the first transistor at Bell Labs in 1947, and the first integrated circuit (IC) patented by Jack Kilby in 1959 [5], electronics have transitioned from large pieces of heavy, specialized equipment, to being integral parts of our daily lives in the form of computers, televisions, and cellular phones, to small items such as watches, banking and identification cards.

Electronics packaging techniques have evolved alongside the circuits they contain. These packages provide essential functions such as physical protection of the device, as well as thermally conductive pathways for heating and cooling. Basic integrated circuit packages are formed from a metal, plastic or ceramic body with leads connecting power and digital or analog input and output between the IC and the board to which it is mounted. An example of this package is shown in Figure 1.1. While providing a convenient method to protect ICs during transportation, as well as handling during assembly, the long leads passing through the package body, as well as the bonding wires connecting these leads to the die, introduce significant parasitic inductance, capacitance and resistance, limiting high-frequency performance of the circuit [6].

Chip-on-board (CoB) assembly provides an alternate process to connect an IC to a larger

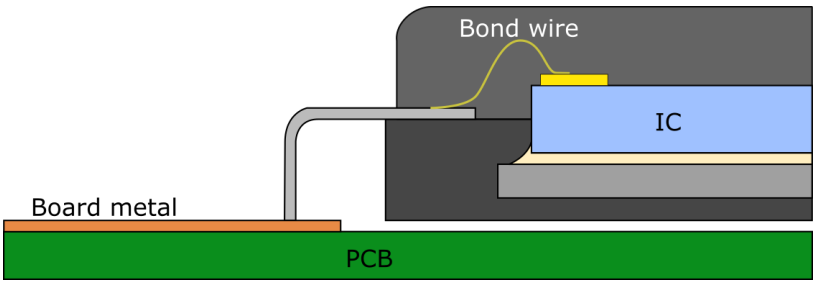

Figure 1.1: Typical packaged integrated circuit with bonding wires.

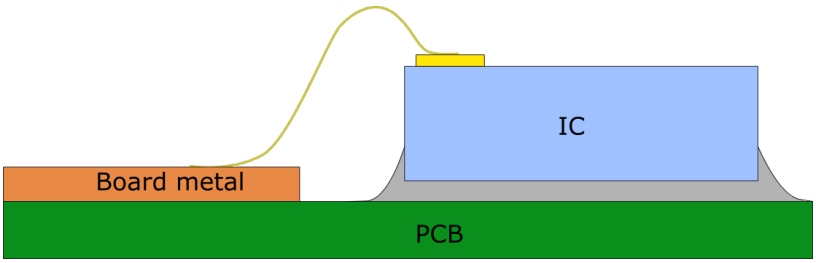

Figure 1.2: Chip-on-board style construction with bonding wire.

circuit board, eliminating some of the undesirable characteristic of a larger package. In this process, as illustrated in Figure 1.2, individual die are attached directly to a circuit board, either at the surface or within a recess formed in the board, and are subsequently connected to metal traces by bonding wires. Though these bond wires still introduce some unwanted parasitic effects, they are greatly reduced compared to their packaged counterparts. These effects can be further reduced by using multiple bond wires in parallel, or with wide ribbons of wire [7, 8].

With interest in radio frequency electronics moving from the microwave regime to millimeter and sub-millimeter ranges, further reductions in unwanted parasitic effects due to packaging are required. The flip-chip assembly process eliminates bonding wire entirely, instead utilizing a solder bump or micro-bump, to form connections between individual pads on an IC die and the board to which it is attached. Figure 1.3 shows an example of flip-chip style connections. In addition to a reduction in unwanted parasitic interactions, this process also allows for increased circuit density due to the small outline of typical devices used. Though effects such as detuning of sensitive components on the die can occur as a result of interactions with adjacent metal and dielectric materials, this process provides low-loss, impedance matched connections operating beyond 60 GHz [9, 10, 11]. Fan-out wafer-level packaging further improves on this process, fanning out the on-chip connections with a redistribution layer (RDL), eliminating the need for chip under-fill materials [12] typically required to provide additional mechanical support to the IC.

Reducing or eliminating losses associated with connections to an individual device is ben-

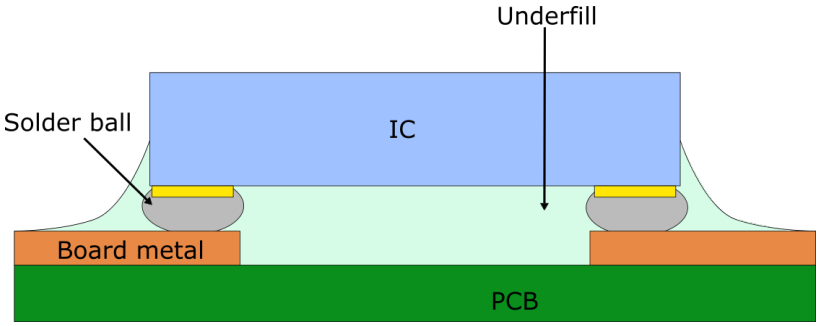

Figure 1.3: Flip-chip style construction with solder balls.

eficial; however, rarely are these devices used individually. In the digital domain, microprocessors and microcontrollers are commonly combined with external memories and interfaces for signal conditioning and sampling. In radio systems, amplifiers, filters, mixers, oscillators and other components are combined to create functional transmitter and receiver chains. While each of these pieces can be attached to a circuit board individually, high connection density may make the PCB fabrication process prohibitively expensive. Excessively long connections between critical components, such as between microprocessors and high speed memory, can suffer from dispersion effects and dielectric losses of the substrate, as well as resistive losses incurred in the metal trace of the circuit board. By combining these components into multi-chip modules (MCMs), critical connections between devices can be formed with well-controlled impedances, as well as time or phase delay, while providing external connections for less critical signals and power. For high power applications, substrate choice becomes important as some materials, such as aluminum nitride, are better able to conduct heat than others [13]. Cooling channels can also be fabricated throughout the substrate, allowing for integration of higher power devices with efficient cooling mechanisms [14].

System-on-Package (SoP) and System-in-Package (SiP) processes build on the MCM concept, taking advantage of unused space to increase functional density. SoP processes take advantage of space available within the substrate, incorporating passive components such as resistors, inductors and capacitors [15, 16], as well as antenna networks [17, 11, 18] which may otherwise be impractical to implement on a die. SiP further reduces interconnection

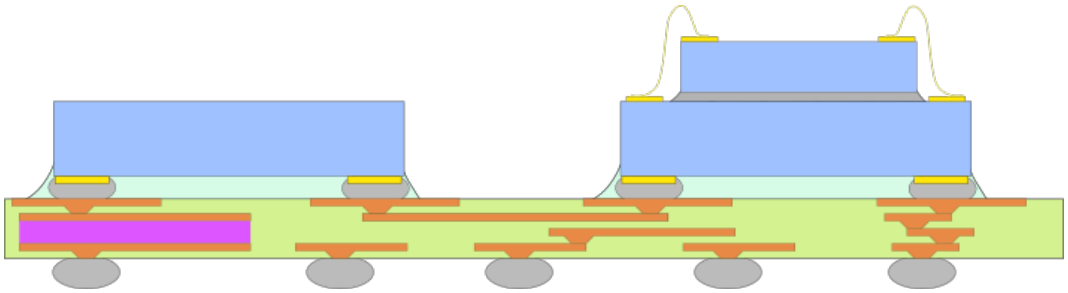

Figure 1.4: Example of MCM construction incorporating both SoP and SiP processes.

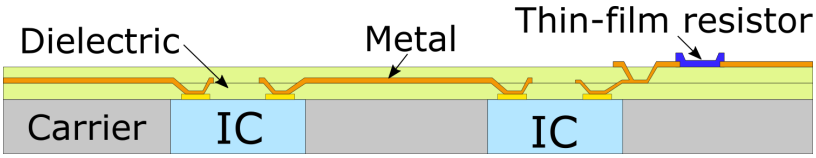

Figure 1.5: Example of chip-first construction.

length between devices by stacking die vertically, with direct connections between bonding pads of devices [19]. Figure 1.4 shows an example of a multi-chip module incorporating both SoP and SiP processes.

Chip-first fabrication processes, in which a device is embedded within the substrate, while additional dielectric and metal layers are deposited and patterned, can further shorten critical path lengths between devices. This process was first patented by the Phillips Corporation in the 1960s, embedding a die in a flexible substrate with metal interconnects contacting bonding pads on the device directly [20]. General Electric created a High Density Overlay process by patterning a suitable carrier in which devices are attached and encapsulated in an epoxy material, with dielectric layers and metal interconnections are subsequently deposited [21]. As layers are added, additional devices can be included, allowing for greater levels of integration than by including devices in only a single plane [22]. Figure 1.5 shows an example of a chip-first stackup.

1.2 Additive Manufacturing Overview

Additive manufacturing, the processes by which material is deposited layer-by-layer to form three-dimensional objects, has made its way from the laboratory to a wide range of uses

in manufacturing today. Where traditional subtractive manufacturing technologies such as lathes and mills have been the mainstay of fabricating intricate objects, additive processes are now being leveraged to fabricate products for a wide range of industries, from automotive and aircraft components [23], to prosthetic limbs [24], tissue regeneration [25], medication delivery [26] and beyond. By directly depositing the build material, rather than removing excess material from an existing object, intricate features can be fabricated which would be otherwise difficult, if not impossible, to achieve with traditional machining processes, while minimizing material waste.

As interest in additive manufacturing has grown over the past decades, the number of additive processes has also increased, each with their own unique set of advantages and considerations. The materials available for these processes is also widely varied, from extruded plastics, to photopolymers, ceramics and metals. Stereolithographic printing (SLA) has been in use as far back as 1982, first reported by Hideo Kodama [27]. In this process, a build platform is submerged in a photopolymer resin, while a laser draws a pattern over this surface. The build platform moves to prepare for deposition of the next layer, and the process is repeated until the print is complete. While this process can be time consuming for particularly large objects, finer print resolution is achievable than with other additive processes, typically less than 50 µm, enabling the fabrication of structures with small features such as microfluidic systems [28]. Digital light projection (DLP) processes can be applied to improve the standard SLA process, imaging complete layers in a single exposure rather than drawing each layer with a single laser point, greatly improving printing speeds.

While SLA printing processes can produce high quality parts, long print times and the high cost typically associated with these systems have created a need for lower cost printing technologies. Fused deposition modeling (FDM), also known as free form fabrication (FFF), provides a simple, low cost method to fabricate mechanical structures. In this method, a thermoplastic is passed through a heated nozzle, partially melting the material, extruding and depositing it on a build platform. Common materials for this printing process include

Nylon, acrylonitrile butadiene styrene (ABS), and polycarbonate, among others. Despite the low print resolution, typically greater than 200 µm, due to their low cost and rapid fabrication time, printers using the FDM process have found extensive use both among casual home users, as well as in laboratory settings, such as reconstruction of dental castings [29], where models can be digitally stored for printing at a later time, when the physical object is needed.

Similar to SLA printing, polyjet printing processes utilize photopolymers to create objects. Rather than employing a resin tank in which the build platform and object are submerged, polyjet printing selectively deposits the polymers which are cured when exposed to a UV light source, reducing the amount of material required to initiate the build process. This selective deposition enables the printing of multiple photopolymers simultaneously, allowing for fabrication of a wider range of structures which would otherwise need to be created separately and subsequently assembled. By depositing soft or soluble materials, removable structures can be created to facilitate the printing of overhangs or other unsupported features which would be difficult to achieve using the SLA printing technique. Using the polyjet process, objects such as compliant mechanisms have been fabricated [30], as well as shape changing structures [31].

Powder-based printing processes function similarly to that of SLA printing, using powdered material rather than a liquid resin. In binder jetting, a binder material is deposited on the powder bed, additional powder is deposited for the next layer, and the process is repeated to completion. Parts are then sintered in a post-processing step, removing the binder material and fusing the powder [32]. Selective laser sintering (SLS) eliminates the need for binder materials, by directly heating the powder material with a laser. This process has been used for printing a wide range of materials including metals, ceramics and polymers [33]. These processes have been used to fabricate both wire antennas [34], as well as horn antennas [35].

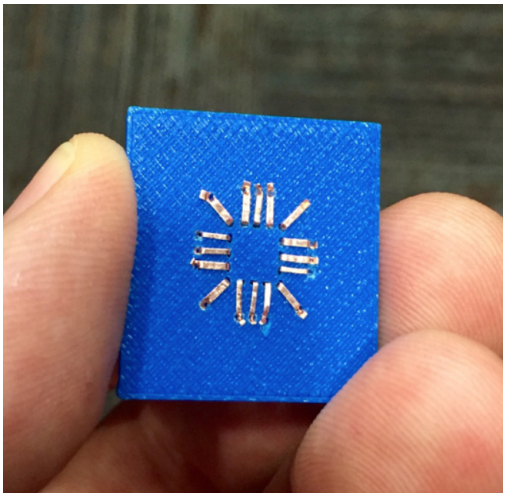

Figure 1.6: FDM printed piece with embedded metal [1].

1.3 Additive Manufacturing for Electronics

With the continuing trend towards additive manufacturing supplementing and/or replacing traditional subtractive processes, attention has turned toward applying these techniques to the fabrication of electronic devices and systems. Several simple, low cost approaches to creating electrical connections between components have been developed over recent decades. Embedding metal traces, by placing metal strips in the object during printing, or by embedding wires in the printed object after printing is completed [1, 36], provide simple methods to create conductive paths between electrical components. By modifying parts to include recesses for metallic traces, either by machining printed pieces in a post-processing step, or modifying the structure to be printed, conductive metallic inks can be applied to form interconnections throughout the final printed object [36].

As operating frequencies increase for both analog and digital systems, new techniques for metallization of printed components become necessary to achieve the features required for high-frequency operation. Waveguide structures, which require smooth metallic surfaces to achieve minimal transmission losses, have been fabricated using SLA printing and subsequent metallization. Metal layers are formed by the deposition of a metallic seed layer by way of sputter coating, evaporative coating, or electroless deposition. Additional metal can then be

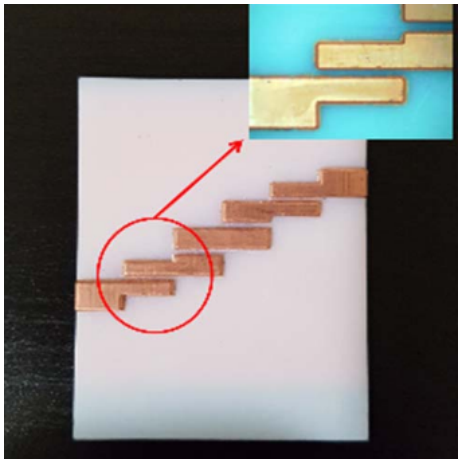

Figure 1.7: SLA printed part metalized using damascene-like process from [2].

deposited over this seed layer by using an electrolytic plating processes to obtain a sufficiently thick conductive layer [37, 38, 39]. This blanket metallization process provides good large area coverage, but is insufficient for realization of fine features without additional processing. By modifying the structure of the object to be printed, elevating areas in which copper metal is unwanted, a damascene-like process can be employed to remove excess metal by mechanical polishing [40]. By taking advantage of the SLA printing processes ability to deposit multiple materials during printing, finer features can be realized without the need to modify the structure of the printed object. Sacrificial material can be printed over areas in which metal is unwanted, enabling the use of a lift-off process to remove unwanted metal which has been blanket deposited over the printed part [40, 2].

While FDM and SLA processes can be combined with blanket metalization for fabrication of electrical components by employing both lift-off and damascene-like processes, the feature sizes which can be achieved by these methods are limited by printer resolution. With interest in wireless systems moving from the microwave frequency range to mm-wave and beyond, the resolution of these printing technologies poses a significant challenge in achieving desired operation characteristics. Inkjet and aerosol jet printing technologies have been proven to overcome some of these limitations, enabling deposition of smaller features, as well as the ability to deposit metallic inks along with a variety of other materials, while sacrificing

printing speed and build area.

Inkjet printing has been used widely for printing both dielectric materials, as well as inks containing metal nanoparticles. However, the materials available for this method have been limited to low viscosities, typically in the range of 10 to 30 cP. Though inks can be formulated to comply with this limitation, this typically increases the time required to print a part, as loading factors of materials may be low, requiring additional passes to deposit the required amount of material. Inkjet printing has been used in the fabrication of a wide range of objects, from ceramic dental crowns [41], to polymer transistor circuits [42]. Complete inkjet printing of polymer and metal materials have been demonstrated in the creation of inductors and capacitors [43, 44], antennas [45], and filters [46]. Inkjet printing has also been used to deposit structures operating in the sub-millimeter wave frequency range, such as polymer-based beam splitters [47], and metamaterials printed with silver nanoparticle ink [48].

Aerosol jet printing has recently proven to also provide a convenient means to deposit materials while achieving good print resolution. Where inkjet printable materials are limited to somewhat low viscosities, aerosol jet printing can utilize materials with viscosities up to 1000 cP. Inkjet and aerosol jet printing are both capable of depositing thin layers of materials, typically in the range of several hundred nanometers, as well as narrow features down to 10 µm or less. However, aerosol jet printing can also be configured to deposit individual features as wide as several millimeters, providing an increase in printing speed when large areas of metalization are required, at the sacrifice of fine resolution. Aerosol jet printing has been used to fabricate of a wide range of electrical circuits, including transmission lines operating beyond 100 GHz [49], coupled line filters [50], as well as antennas [51], inductors, capacitors and resistors [52]. Unlike other printing technologies such as inkjet printing, aerosol jet printing has a large stand-off distance between the work surface and the print head, enabling printing on non-planar surfaces [3]. Figure 1.8 shows an example of a circuit printed on a tank with the aerosol jet printing process.

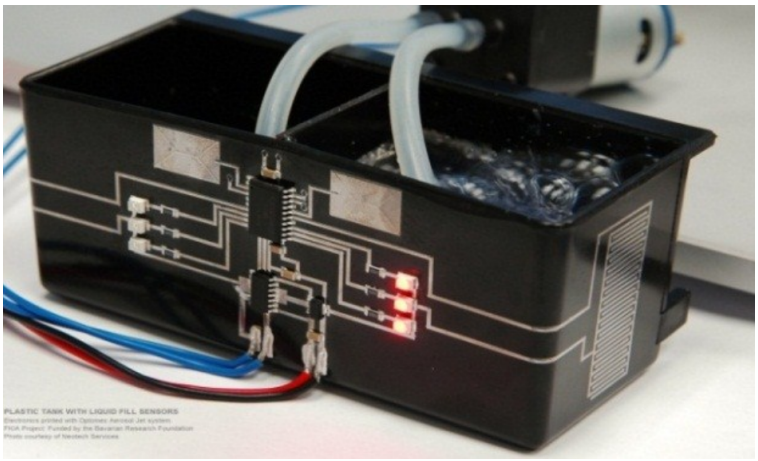

Figure 1.8: Aerosol jet printed fill level sensor on bucket [3].

1.4 Electronics Packaging by Additive Manufacturing

Additive manufacturing techniques present a new step in the evolution of electronics packaging. By providing a low cost means of rapidly producing prototype circuits necessary during design stages, as well as a low cost method for fabricating devices, electronic systems will continue to be integrated in our daily activities. While fabrication process such as wire bonding have provided easy means of connecting integrated circuits to boards and carriers, [53] demonstrates that bonding to printed metal traces can be difficult to achieve. Processes to directly connect printed metal traces to device bonding pads must be developed to facilitate further advancements in additive packaging processes. A benefit to fabricating these interconnections by direct-write methods, parasitic effects of the connections can be greatly reduced, enabling operation into millimeter wave and sub-millimeter wave frequency ranges.

Some processes to package electronics utilizing additive manufacturing techniques have already been demonstrated. Packaged electronics have been embedded within printed objects, connected by wires or by traces formed from post-processing of the printed substrate [36]. By embedding devices in an object during the print process, blanket metallization has been employed to create tunable resonators and antennas operating through 7 GHz [54].

With their finer feature resolution and wider range of printable materials, inkjet and

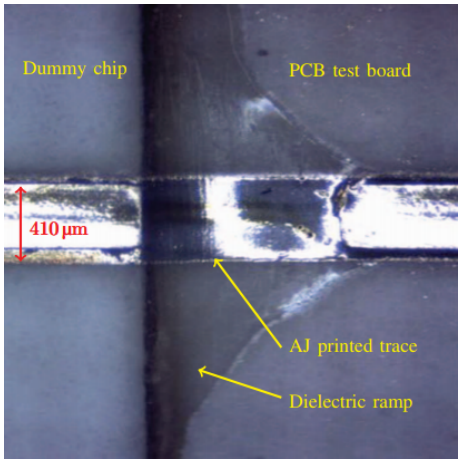

Figure 1.9: Aerosol jet printed chip-to-board connection over dielectric ramp [4].

aerosol jet printing can be used to package bare integrated circuits. Aerosol jet printing of chip-to-chip connections have been demonstrated in [55]. In this process, devices are attached to a carrier substrate and encapsulated in an epoxy material. The epoxy is subsequently patterned by laser ablation, followed by aerosol jet printing of silver connections between the bonding pads of the device. Though effective, this process does require a degree of planarity of the individual die, which may be difficult to ensure. Aerosol jet printing has also been used for fabrication of chip-to-board interconnections. With a large stand-off distance of 3 mm or more between the print head and work piece, substrates can be manipulated and rotated to expose surfaces for printing which would be difficult to perform using processes such as inkjet printing. Due to the thin layers of material typically deposited by aerosol jet printing (< 1 µm), and the significantly greater device thicknesses typically encountered (> 100 µm), dielectric ramps are necessary to provide a surface over which metallic inks can be deposited. By depositing these fillets, electrical contact can be formed with devices, enabling a chip-on-board style construction using additive processes [56]. These bond wire replacements have been shown to perform well, reducing losses associated with such connections compared to typical bonding wires [4, 57]. Figure 1.9 shows an aerosol jet printed connection over dielectric ramp demonstrated in [4].

Figure 1.10 illustrates a possible additively manufactured package. Printed dielectric

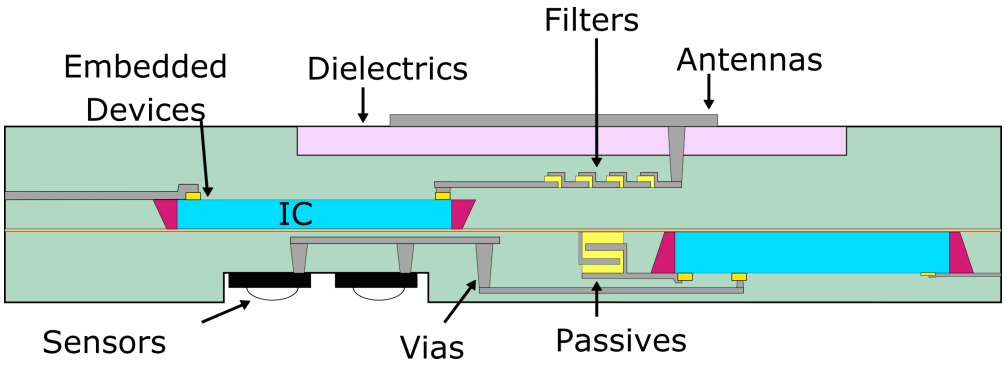

Figure 1.10: Additively manufactured packaging concept.

materials can enable localized fan-out of high-density interconnections, a process which traditionally requires a complex printed circuit board with multiple layers to achieve. Printed dielectrics can be tailored for localized deposition of materials with varied dielectric constants, enabling antennas and passive components to exist within the same substrate needed for component protection, heat dissipation, and signal and power distribution.

1.5 Dissertation Outline

The objective of this work is to develop processes for packaging electronics operating from the microwave frequency range into the terahertz spectrum utilizing additive manufacturing techniques. This work is organized as follows:

In chapter 2, high frequency limitations of the aerosol jet printing process are investigated. Band-pass and band-stop filters are designed, fabricated and measured, operating from 200 GHz through 550 GHz. Polarizing screens are demonstrated from 100 GHz to beyond 700 GHz. Impacts of line dimensions of aerosol jet printed silver traces are demonstrated. Effects of electroless plating processes on printed filter performance is investigated. The performance of each of these filters and polarizers are measured using a commercial frequency-domain terahertz system.

In chapter 3, a fixed-frequency oscillator is designed and fabricated using aerosol jet printing. Designed for operation at 10.1 GHz, performance of aerosol jet printed distributed microwave circuit elements is easily measured. Processes for via fabrication using both

conventional mechanical drilling, as well as reactive ion etching, and their compatibility with aerosol jet printed metal traces, are demonstrated.

Chapter 4 demonstrates aerosol jet printed interconnections to bare-die integrated circuits embedded within a commercially available substrate. By embedding devices within a substrate, undesirable parasitic effects due to interconnection length are minimized. Processes for embedding devices within a substrate are demonstrated. The ability to iterate the printing process to repair failed interconnections is also demonstrated. Finally, undesirable effects of printing metal interconnections over a bare semiconductor material are investigated.

Chapter 5 combines two additive manufacturing processes, aerosol jet printing and selective laser annealing, in the fabrication of a completely packaged system-on-antenna. By combining additive processes, a complete system can be developed and deployed quickly and at low cost, using the antenna body as the protective package for the electronics contained within. This process utilizes SLA printing for the fabrication of a passive Vivaldi antenna, with aerosol jet printing of connections to devices embedded using processes demonstrated in chapter 4. An additional polymer ink is developed and characterized to improve the transition from the substrate to the bonding pads of the integrated circuits.

CHAPTER 2

HIGH FREQUENCY APPLICATIONS OF AEROSOL JET PRINTING

2.1 Introduction

Over the last two decades, interest has grown in the development of systems operating in the frequency range of 100 GHz to 10 THz, commonly referred to as the terahertz (THz) spectrum. Systems operating in the THz frequency range have a wide array of applications, including medical imaging [58], biology [59], substance detection and imaging for security [60, 61], among many more.

Traditionally, fabrication of components operating in the THz spectrum employ processes such as micromachining, and other lithographic techniques [62], as well as the use of dedicated machinery such as that used to fabricate polarizing screens [63], [64]. These processes typically require cleanroom facilities, multiple pieces of dedicated equipment, as well as highly skilled technicians to fabricate intricate THz components. While subtractive processes such as laser machining have been demonstrated in the fabrication of polarizing screens [65], such a process is difficult to adopt in the fabrication of free-standing or layered structures.

Additive manufacturing (AM) has been touted as a replacement to traditional methods in the fabrication of THz components. Advantages of AM include fast prototyping, low material loss and low hazardous waste generation. With AM, a single tabletop system is sufficient to fabricate a wide range of components, rather than requiring multiple machines, each dedicated to a specific fabrication task. Recently, a range of 3D printed THz components have been demonstrated using AM technologies. This includes the use of FDM to fabricate focusing grating couplers [66], focusing lenses for near-field microscopy [67], as well as gradient-refractive-index lenses [68]. SLA processes have been used to fabricate ribbon waveguides, power splitters and micro-lens arrays [69, 70]. SLA has also been used to

produce molds for the injection molding of THz components using high-density polyethylene [71], allowing for the fabrication of THz components using low-loss dielectrics that are difficult to print directly using other AM techniques.

Inkjet printing has also been used as another low cost method to print thin film structures, especially conductive inks on planar substrates, such as polarizer screens [72, 73]. High resolution structures having 5 µm resolution have been demonstrated using this approach [74]. Similarly, laser printing has been demonstrated in the fabrication of metamaterial structures in the THz frequency spectrum [75]. Electrohydrodynamic jet printing can produce smaller features, and has been shown as a potential method to fabricate THz metamaterials [76], as well as sensors for detection of biological materials [77]. While these techniques work well for depositing fine features, they are difficult to implement for printing structures on non-planar surfaces.

With a much greater standoff distance compared to inkjet printing technologies, aerosol jet printing is capable of depositing materials with great accuracy, enabling printing on a much greater variety of substrates. Aerosol jet printing has been successfully used to fabricate planar circuits operating at 160 GHz [78], as well as the fabrication of multilayer passive circuitry [79]. More recently, aerosol jet printing has been demonstrated for fabrication of terahertz passive components [80, 81].

Figure 2.1 depicts the critical components in the aerosol jet printing process. A silver nanoparticle ink, as an example, is atomized by an ultrasonic transducer, and is carried to the print head by means of a nitrogen gas stream. In the print head, the aerosolized nanoparticle stream is combined with a focusing sheath gas, creating a well formed column of ink which is then deposited on the substrate material of choice. While inkjet printing typically requires inks with low viscosity (10 - 30 cP), the aerosol jet process can utilize inks with viscosity ranging from 1 - 1000 cP, enabling the deposition of a wider range of materials. However, due to the aerosolization process, particle size of materials dispersed in these inks is typically limited to less than 200 nm. Adhesion of inks to substrate materials introduces

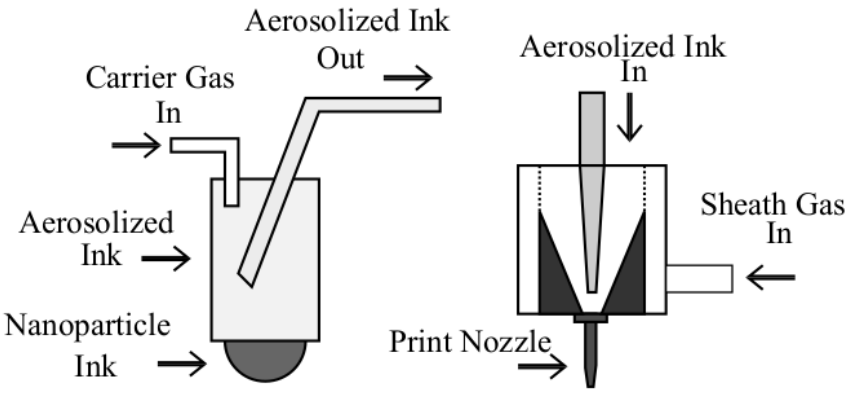

Figure 2.1: Aerosol jet system components. Left: ultrasonic atomizer. Right: print head with nozzle.

additional constraints, limiting the material choice for both inks and substrates.

The goal of this chapter is to investigate the performance of aerosol jet printed components compared to lithographic fabrication for use in the THz frequency regime. Jahn et al. recently demonstrated aerosol jet printed resonant structures in [81]. In contrast, the structures presented in this chapter demonstrate the applicability of aerosol jet printing to larger, more complex designs, and these are compared to their counterpart fabricated using conventional photolithography. Three filter designs are used for this study, including a band-pass filter designed to operate at 250 GHz, and two band-stop filters, one operating at 250 GHz and the other at 550 GHz. In addition, polarizing screens having fine line resolution with long continuous lines are investigated. Finally, reduction in loss characteristics of printed structures by means of an electroless copper plating system using aerosol printed silver ink as a seed layer is demonstrated. These structures demonstrate printing of components requiring maximum surface coverage with metal (band-pass filters), minimal surface coverage (band-stop) and long fine line structures (polarizers).

2.2 Design and Simulation

Several components have been fabricated to evaluate high-frequency performance of aerosol jet printed structures on flexible organic materials. Each of the components has been fabricated on a liquid crystal polymer (LCP) substrate, Rogers Ultralam 3850HT. While

other materials such as quartz are traditionally used in the fabrication of THz components due to their excellent dielectric properties, this cannot be flexed to conform to other surfaces. Additionally, the particular ink used in this work does not adhere well to quartz after sintering, resulting in poor performance. LCP has been selected for its low loss characteristics in the frequency range of interest [82], its compatibility with the silver nanoparticle ink to be printed, and its thermal stability at the temperatures required for sintering of the silver ink. To reduce the impact of substrate loss on transmission characteristics, the thinnest available substrate, 25.4 µm, is used here for all the designs. Several constraints are considered in the design of each component to be fabricated. Due to the limitations of low cost masks available for photolithography, no features smaller than 40 µm will be considered for performance comparison between aerosol jet printed structures and lithographically fabricated structures.

2.2.1 Printed Silver Characterization

Printed silver nanoparticle ink requires a post-print processing step to yield a metal layer with acceptable electrical conductivity. Thermally sintering printed silver is a simple process, typically requiring little more than a heat source. By varying both time and temperature, a range of electrical conductivity can be easily achieved [83]. The range of suitable substrate materials is further reduced due to the need for this additional thermal process. While the chosen LCP substrate material has a melting temperature beyond 300 °C, due to differences in coefficient of thermal expansion between the substrate and the printed metal, substrate deformation has been observed beyond 200 °C. As a result, a post-print sintering process is performed at 180 °C for 3 hours.

Figure 2.2 shows the layout of a structure used for measuring conductivity of sintered printed silver metal. Four pads measuring 0.5 mm x 0.5 mm allow for contact by a four-point probe. At the outer two conductors, a current is applied across the metal trace, with the inner two conductors allowing for measurement of the voltage drop between these pads. Conductivity of the sintered metal can be calculated as:

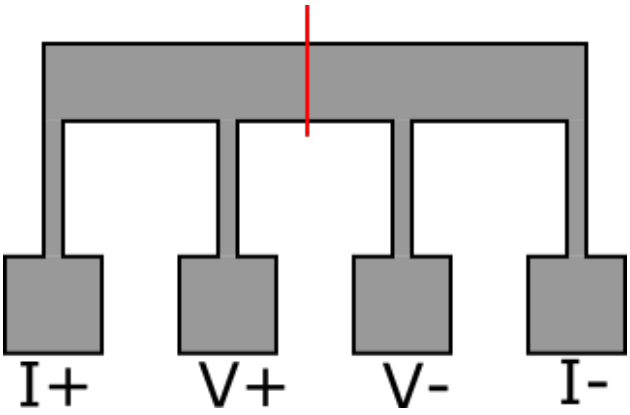

Figure 2.2: Pattern for printed silver conductivity measurement.

$$\sigma = \frac{lI}{AV} \tag{2.1}$$

where σ is the metal conductivity, l is the length of the line between voltage measurement pads, V is the measured voltage drop, A is the cross sectional area of the line, and I is the test current injected into the structure. The cross sectional area of the line under measurement can be measured using a variety of techniques. Figure 2.3 shows the cross-sectional area of a silver metal trace printed on a glass microscope slide, measured using a NanoMap-500LS contact surface profilometer. Using the above sintering process, conductivity as high as 1.75 x 10^7 S/m has been achieved. Due to process variations throughout the duration of a print, simulations are performed using a lower conductivity of 1.2 x 10^7 S/m to ensure adequate performance of the final fabricated structure.

Performance of both filters and polarizer screens may be degraded due to insufficient metal thickness. Skin depth, defined by Equation 2.2 [84], where f is the frequency of operation, μ is the magnetic permeability of the material, and σ is the DC conductivity of the material, is the depth at which the current density in a metal has decreased to e^{-1}, or approximately 36.8%, of its maximum at the metal surface.

$$\delta = \frac{1}{\sqrt{\pi f \mu \sigma}} \tag{2.2}$$

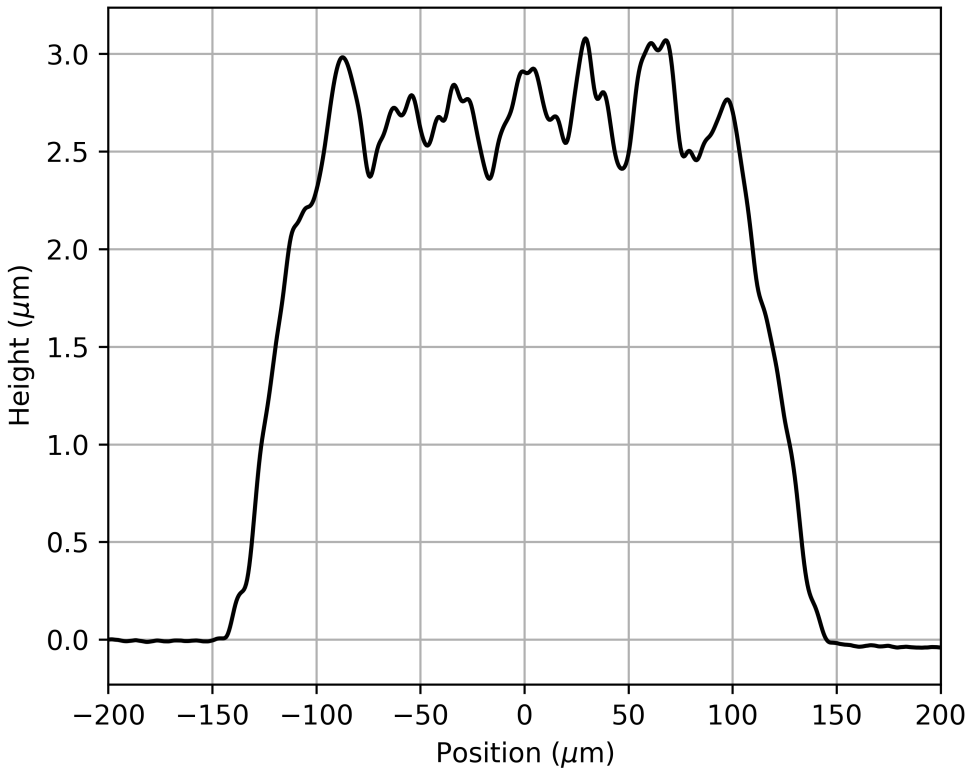

Figure 2.3: Measured silver cross-sectional area of printed metal conductivity measurement structure.

To minimize filter and polarizer degradation due to insufficient metal thickness, metal layers approximately 5 skin-depths (δ) in thickness as calculated at 100 GHz are used. For copper metal, which has a conductivity of approximately 5.8 x 10^7 S/m, this corresponds to a thickness of 1 µm, and approximately 2 µm of metal for aerosol jet printed silver.

2.2.2 Filters

Three filters have been designed, providing band-pass and band-stop behavior, to demonstrate applicability of aerosol jet printing for the THz frequency spectrum. Each of these filters are designed for both fabrication by photolithography of copper metal, and aerosol jet printed silver metal.

Each of the designed band-stop filters is formed using a cross-like unit cell metal structure. Band-pass filters are formed by the inverse of this structure, where each cross is formed by an

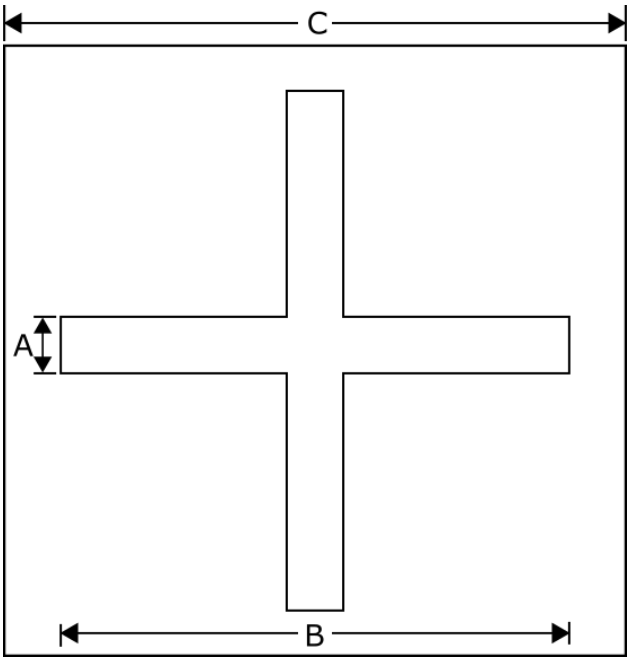

Figure 2.4: Schematic representations of band-stop and band-pass filter unit cell. A: filter line width, B: filter line length, C: filter unit cell width and length.

opening in a metallic sheet. Simulation of each of these filters is performed by designing each filter as a unit cell, and applying the Floquet Theorem, approximating a two-dimensional structure of infinite size. Figure 2.4 depicts the unit cell geometry of each filter. The cross structure used for each of these is necessary, due to the elliptically polarized radiation of the measurement system which will be used to verify each design. Simulation of each filter is performed using ANSYS High Frequency Structure Simulator (HFSS).

A band-stop filter has been designed for operation at 250 GHz. This filter is formed by a metal cross with line widths (A) of 50 µm, line lengths (B) of 433 µm, and a unit cell width and length (C) of 473 µm. These dimensions are summarized in Table 2.1. Simulation of this filter, both for copper metal and aerosol jet printed silver metal, can be seen in Figure 2.5. Simulated results of each of these filters are similar, demonstrating resonance at 250 GHz, with a transmission coefficient of approximately -30 dB for both copper metal and printed silver.

The geometry of the 250 GHz band-stop filter can be modified to achieve operation at

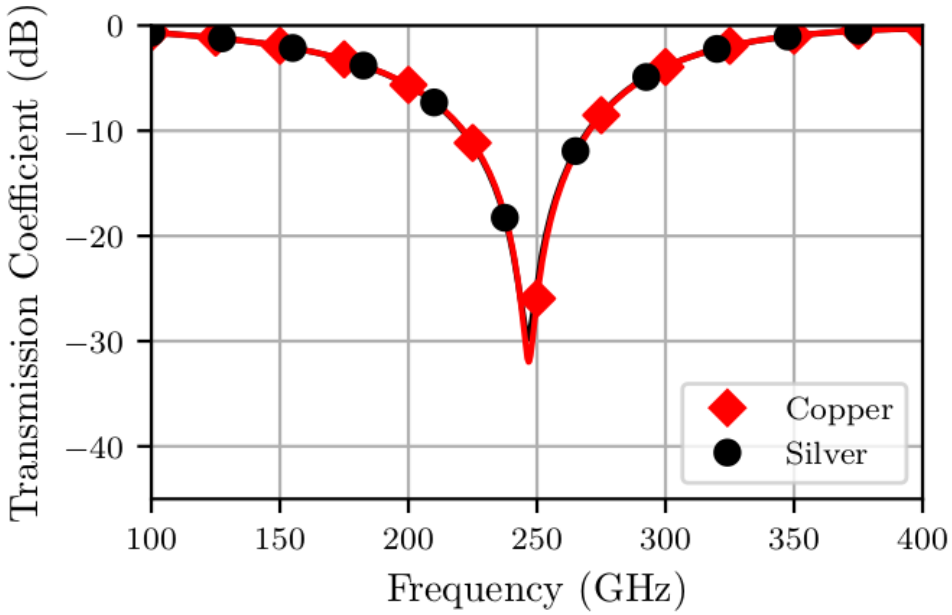

Figure 2.5: Simulated transmission coefficient of 250 GHz band-stop filters.

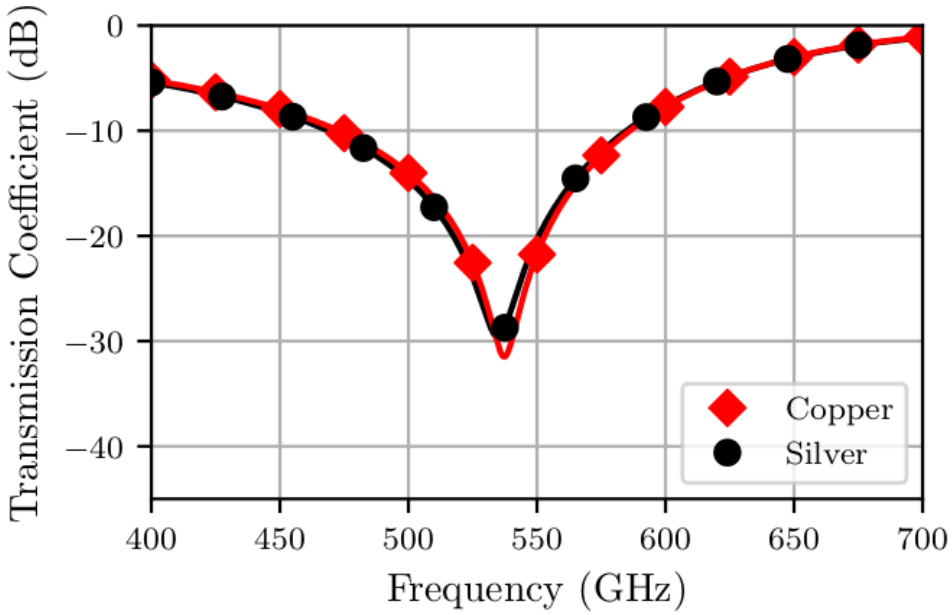

Figure 2.6: Simulated transmission coefficient of 550 GHz band-stop filters.

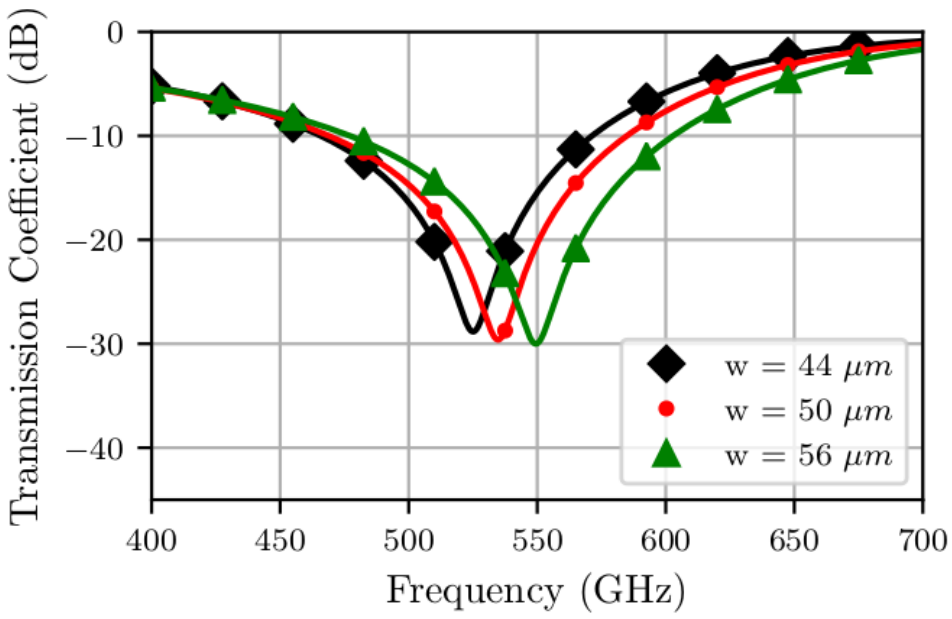

Figure 2.7: Simulated transmission coefficient of 550 GHz band-stop filters of different line widths.

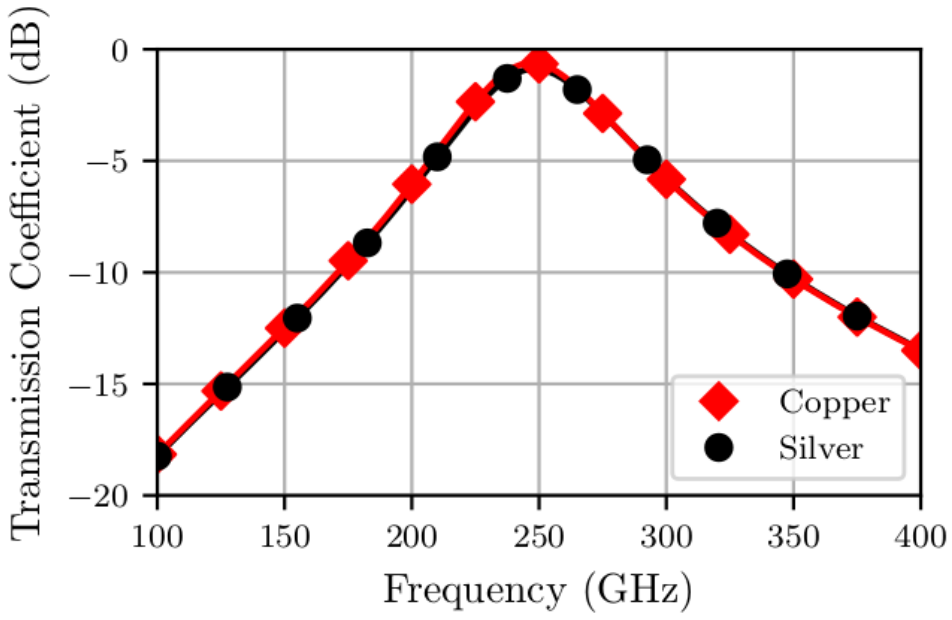

Figure 2.8: Simulated transmission coefficient of 250 GHz band-pass filters.

a higher frequency. For operation at 550 GHz, the cross line width is maintained at 50 µm, while the line length is reduced to 209 µm, and the unit cell length and width are reduced to 249 µm. These dimensions are summarized in Table 2.2. Figure 2.6 shows simulation results of this filter. While the resonance frequency is not centered on 550 GHz, this filter will be more sensitive to dimensional variation due to the fabrication process. Figure 2.7 shows simulation results for line widths varied by ±6 µm, resulting in a shift in resonance between 530 and 550 GHz. The transmission coefficient for this configuration both in copper metal and printed silver metal simulations are similar. Each of these filters results in resonance at 535 GHz with a transmission coefficient of -30 dB.

A band-pass filter designed for operation at 250 GHz is formed by the inverse of the band-stop configuration, where each cross is formed from a void in a solid metal sheet. This filter is formed with a line width of 50 µm, a line length of 454 µm, and a unit cell length and width of 494 µm. These dimensions are summarized in Table 2.3. Simulation results of this filter are shown in Figure 2.8. The pass-band transmission coefficient of this filter configuration is approximately -0.6 dB for copper metal, while silver metal results in a slightly higher pass-band transmission coefficient of -0.9 dB.

2.2.3 Polarizers

Two polarizers have been designed, formed by a wire screen. Design and simulation of these polarizers is performed in a similar manner to that which has been used for the design of each of the filters above, by simulating a single unit cell approximating a structure of infinite size in two dimensions. Figure 2.9 shows a schematic representation of this unit cell structure.

Each polarizer is designed with identical line widths (D), and line separations (E). A pair of polarizers, fabricated from copper metal as well as aerosol jet printed silver, are designed with line widths and spacings of 40 µm. The unit cell width and length (F) of each of these polarizers is 400 µm. Performance of each polarizer is characterized by the ability of the polarizer to extinguish electromagnetic waves which are polarized parallel to the wire

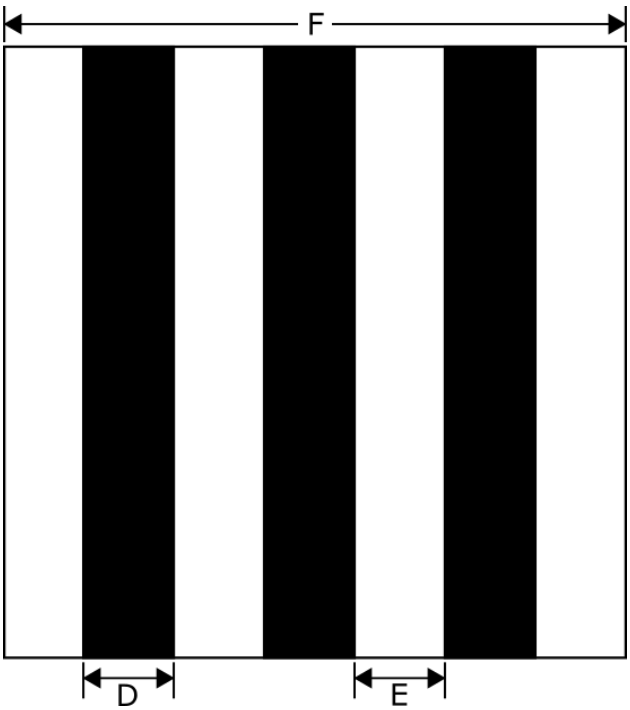

Figure 2.9: Schematic representations of polarizer unit cell. D: polarizer line width, E: line separation, F: unit cell width and length.

orientation. This extinction ratio can be expressed as:

$$E_r = 10\log(\frac{P_{tm}}{P_{te}}) \tag{2.3}$$

where P_{te} is the power of the incident wave polarized parallel to the wire grid, and P_{tm} is the wave polarized perpendicular to the wire grid. Simulation results of these polarizers are shown in Figure 2.10. The extinction ratio of each of these polarizers is approximately 30 dB at 200 GHz, decreasing with frequency to approximately 20 dB at 700 GHz.

An additional polarizer has been designed for fabrication only by aerosol jet printing. This polarizer is formed with line widths and spacings of 10 µm, and unit cell lengths and widths of 100 µm. Figure 2.10 shows simulation results of this polarizer. Simulation results of this polarizer demonstrate a significant improvement over the simulated results of the 40 µm polarizers, with an extinction ratio of approximately 45 dB at 200 GHz, to approximately 32 dB at 700 GHz.

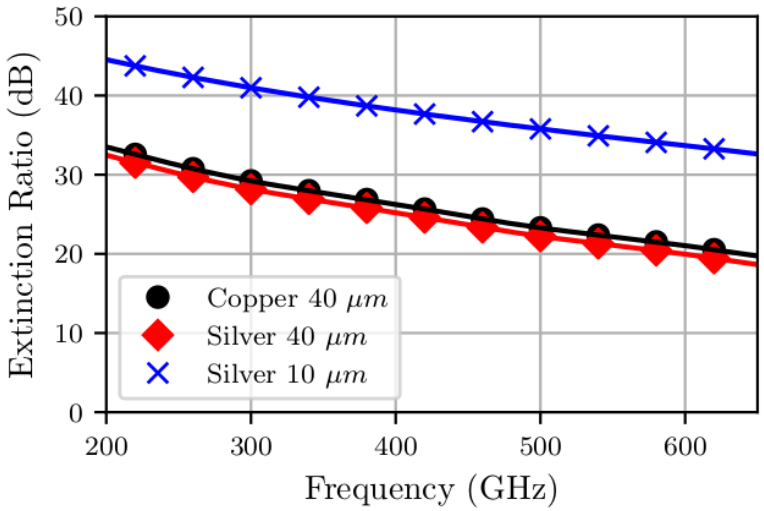

Figure 2.10: Simulated polarizer extinction ratios.

2.3 Fabrication and Measurement

Fabrication of each structure begins with preparation of the substrate material to be used. The LCP material as provided has a 9 µm thick copper metal laminate on both the front and back side. This copper metal is chemically removed in a sodium persulfate bath, and subsequently cleaned in deionized water to remove residue. After drying, this bare LCP substrate can be used without any further processing for aerosol jet printing.

For structures which are to be fabricated with a lithographic process, a copper metal layer 1 µm thick is deposited on a single side of each substrate piece to be used, by means of a Denton Desk Top Pro sputtering system. A tape-peel adhesion test was performed to verify the deposited copper metal would remain attached to the LCP material without the need for additional processing of the substrate. A photoresist material is applied by spin coating, which is then patterned by UV exposure. Each structure is etched in a sodium persulfate bath, and subsequently rinsed in deionized water and dried.

Each of the substrates to be patterned by aerosol jet printing is affixed to a ceramic plate to facilitate handling throughout both the printing and sintering processes. Clariant Prelect TPS 50 G2 silver nanoparticle ink has been selected to fabricate each of the aerosol

jet printed filters. This ink consists of silver nanoparticles which are dispersed in ethylene glycol. The ultrasonic atomization process requires a low viscosity ink, typically less than 10 cP. As provided by the manufacturer, the ink used has a viscosity of approximately 30 cP. To reduce the viscosity to an acceptable range, 1 mL of nanoparticle ink is diluted into 3 mL of deionized water.

Each aerosol jet printed filter has been fabricated using a print nozzle 200 µm in diameter, an atomizer gas flow rate of 22 SCCM, and a focusing sheath gas flow rate of 90 SCCM. The print stage velocity is limited to 1.5 mm/s, to allow for individual printed layers of approximately 1 µm thickness to be deposited per pass. 2 metal layers are printed, to yield a final metal thickness of approximately 2 µm.

Performance of each fabricated structure has been measured on an Emcore PB-7200 frequency-domain THz system. This system is capable of measuring transmittance over a frequency range of 100 GHz to approximately 1.7 THz. This system has frequency measurement resolution of 100 MHz, and amplitude error of approximately 1 dB. The THz radiation is generated by an optically excited photo-conductive switch, and focused through a silicon lens. An off-axis parabolic mirror directs this well collimated beam to the sample to be measured. Due to the spiral shape of the antenna coupled to the photo-conductive switch, the radiation generated by this system is elliptically polarized. In each measurement, only the normal angle of incidence is considered, with each sample fixed to the receiver head unit to ensure proper orientation. In an effort to reduce the size of each filter and to ensure normal incidence of the THz beam, a window of 9 mm x 9 mm was cut from a piece of thick stock copper-clad circuit board material. This window is placed over the receiving head. Figure 2.11 illustrates this measurement configuration. The transmission coefficient of each measured filter is calculated by:

$$TC_{filter} = 10\log(\frac{P_{filter}}{P_{background}}) \tag{2.4}$$

where P_{filter} is the measured power transmitted through the filter, and $P_{background}$ is the

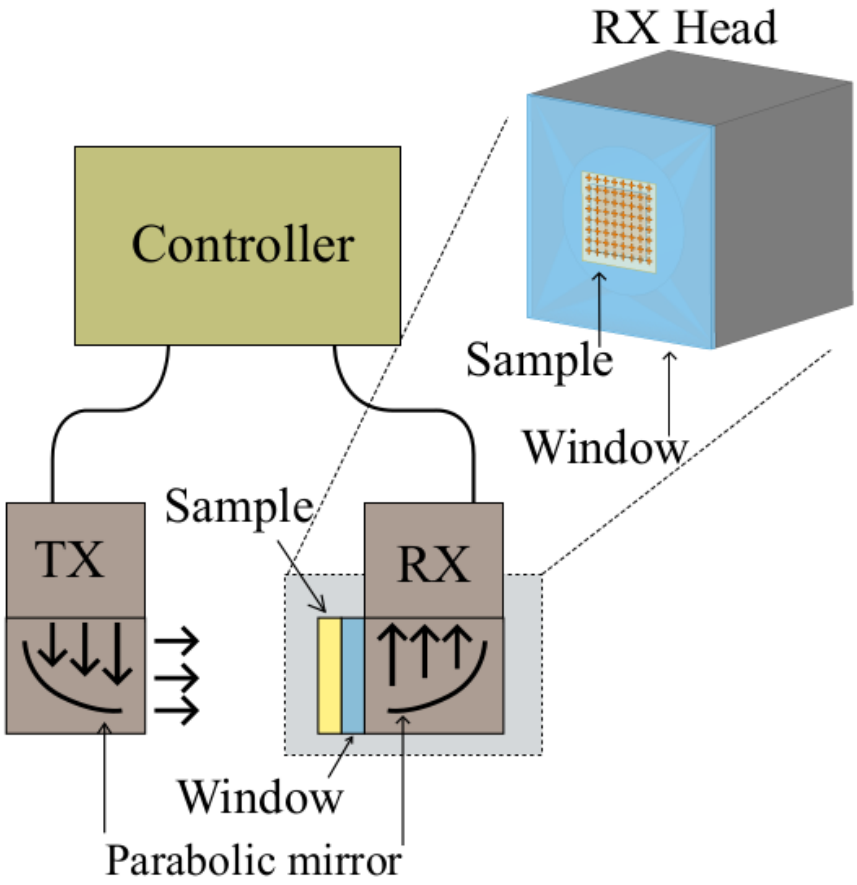

Figure 2.11: THz frequency domain measurement setup.

measured transmitted power with no filter in the signal path.

2.3.1 Filters

Figure 2.12 shows an image of a unit cell of the final fabricated band-stop filters designed for operation at 250 GHz. The copper metal structure can be seen on the left, with the aerosol jet printed structure on the right. Measured dimensions of the fabricated copper metal filter show a line width (A) of 40 µm, and line length (B) of 430 µm. Measured dimensions of the aerosol jet printed filter show a line width (A) of 30 µm, and line length (B) of 430 µm. These dimensions are summarized in Table 2.1.

Figure 2.13 shows measured results of each of the 250 GHz band-stop filters, as well as simulation results utilizing measured dimensions of each fabricated filter. The filter fabri-

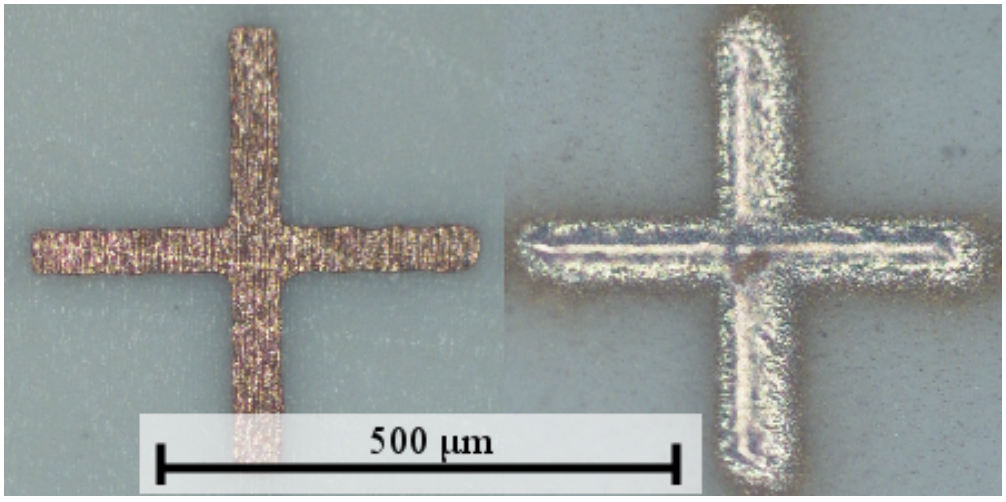

Figure 2.12: Unit cell of fabricated 250 GHz band-stop filters. Left: Copper metal with lithographic process. Right: Aerosol jet printed.

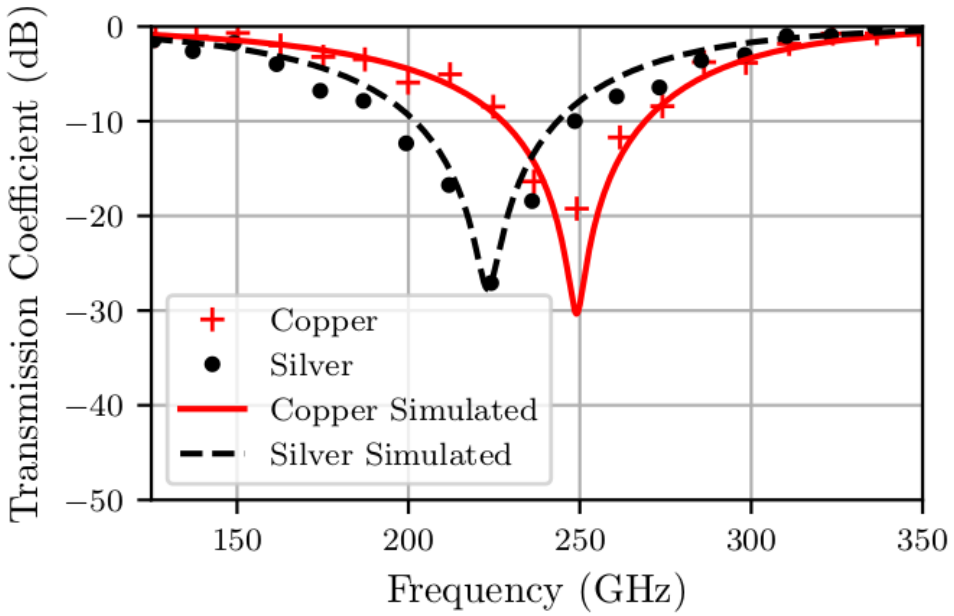

Figure 2.13: Measured transmission coefficient of 250 GHz band-stop filters.

cated from copper metal demonstrates resonance at 250 GHz, with a transmission coefficient of -30 dB at resonance. The aerosol jet printed filter results in resonance of approximately 225 GHz, with a transmission coefficient of -27 dB. As can be observed, the shift in resonance of the aerosol jet printed filter is due to each arm of the cross being both shorter and narrower than the design goal.

Filter		250 GHz Band-Stop	
		Copper	Silver
Line Width (A) (um)	Designed	50	50
	Fabricated	40	30
Line Length (B) (um)	Designed	433	430
	Fabricated	430	430
Unit Cell (C) (um)	Designed	473	473
	Fabricated	480	480

Table 2.1: 250 GHz band-stop filter dimensions.

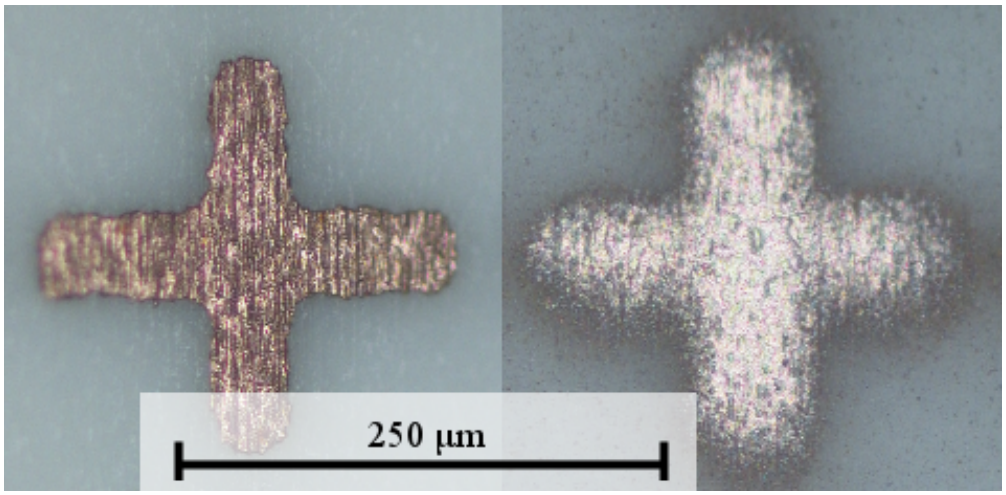

Figure 2.14: Fabricated 550 GHz band-stop filter unit cells. Left: Copper metal with lithographic process. Right: Aerosol jet printed.

Figure 2.14 shows an image of a unit cell of the final fabricated filters designed for operation at 550 GHz, with simulation results utilizing dimensions of the fabricated filters. The measured line width of the copper metal filter is 45 µm, line length is 198 µm. The filter fabricated from aerosol jet printed silver has a line width of 50 µm, line length of 205 µm. Measured performance of these filters can be seen in Figure 2.15. Each of these filters has resonance close to the target frequency of 550 GHz.

Figure 2.16 shows an image of a unit cell of each of the fabricated 250 GHz band-pass filters. Final measured dimensions of the copper metal filter include a line width of 70 µm and line length of 471 µm. Dimensions of the fabricated silver metal filter include a line width of 50 µm, and line length of 490 µm. Measured performance of each of these filters, as well as simulation results using dimensions of each fabricated filter, can be seen in Figure

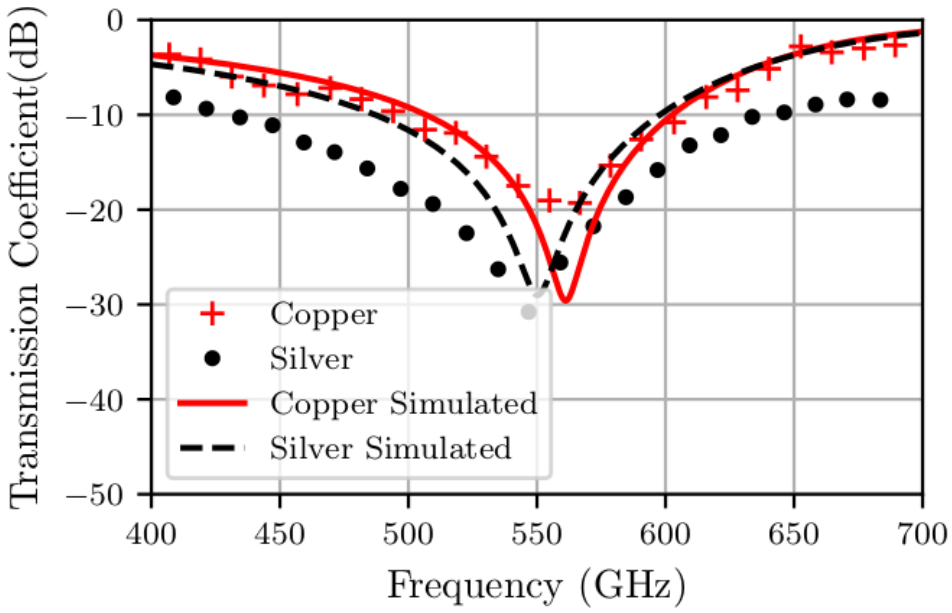

Figure 2.15: Measured transmission coefficient of 550 GHz band-stop filters.

Filter		550 GHz Band-Stop	
		Copper	Silver
Line Width (A) (um)	Designed	50	50
	Fabricated	45	50
Line Length (B) (um)	Designed	209	209
	Fabricated	198	205
Unit Cell (C) (um)	Designed	249	249
	Fabricated	250	250

Table 2.2: 550 GHz band-stop filter dimensions.

2.17. While these offer similar performance, their resonance is slightly lower than the desired frequency of 250 GHz. The measured transmission coefficients of each filter are within the amplitude error of the measurement system.

2.3.2 Polarizers

Aerosol jet printed polarizers have been fabricated utilizing different parameters to achieve different line dimensions. Aerosol jet printed polarizers designed with line widths and spacings of 40 µm utilize the same parameters chosen to fabricate the filters. To fabricate

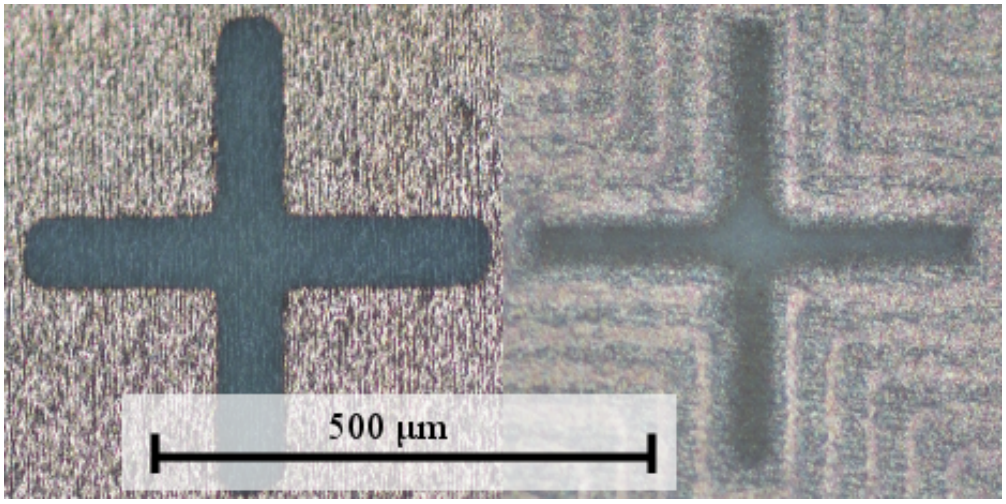

Figure 2.16: Unit cell of fabricated 250 GHz band-pass filters. Left: Copper metal with lithographic process. Right: Aerosol jet printed.

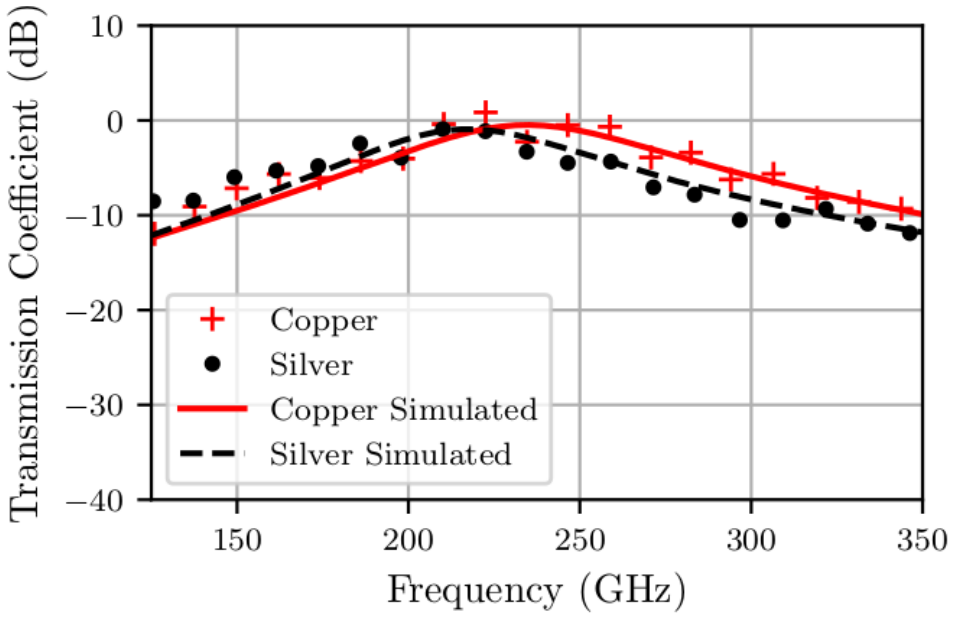

Figure 2.17: Measured transmission coefficient of 250 GHz band-pass filters.

Filter		250 GHz Band-Pass	
		Copper	Silver
Line Width (A) (um)	Designed	50	50
	Fabricated	70	50
Line Length (B) (um)	Designed	454	454
	Fabricated	471	490
Unit Cell (C) (um)	Designed	494	494
	Fabricated	500	500

Table 2.3: 250 GHz band-pass filter dimensions.

polarizers with line widths and spacings of 10 µm, a nozzle with a 100 µm diameter is utilized, with an atomizer gas flow rate of 20 SCCM, and a focusing sheath gas flow rate of 35 SCCM.

Measurement of polarizers requires a linearly polarized source; however, the measurement system used to characterize these structures generates an elliptically polarized wave. To achieve linear polarization, a polarizer with a high extinction ratio must be placed between the source and the component under measurement. Initially, a pair of aerosol jet printed polarizers with 10 µm line widths and spacings has been measured to evaluate their performance. All subsequent measurements have been performed with one of these high extinction ratio polarizers on the measurement source, to ensure adequate linear polarization of the wave incident on the samples under test.

Figure 2.18 shows both copper metal and aerosol jet printed polarizers designed for 40 µm line widths and spacings. Measured dimensions of each of these polarizers show a final line width of 30 µm, resulting in an extinction ratio approximately 5 dB less than the design goal. This deviation in line width also impacts high frequency performance, as the wider gap is electrically larger at higher frequencies. Figure 2.19 shows the final aerosol jet printed polarizer with line widths of 10 µm. The final measured line width of this polarizer is approximately 9 µm. This deviation in line width does not significantly impact the measured extinction ratio of this polarizer over the frequency range of interest. Final measured results, compared to simulated results of each polarizer utilizing these measured line dimensions, can

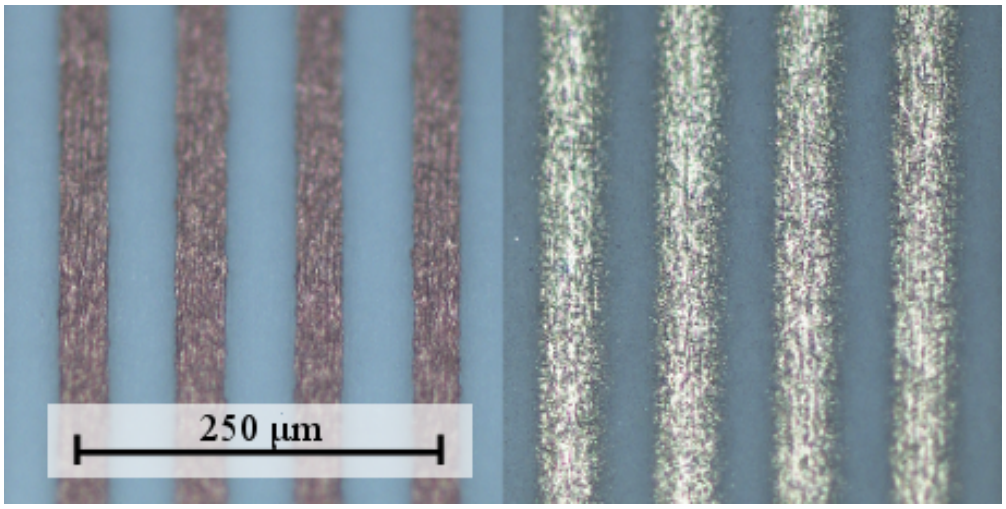

Figure 2.18: Unit cell of fabricated 40 µm polarizer grid. Left: Copper metal with lithograph process. Right: Aerosol jet printed.

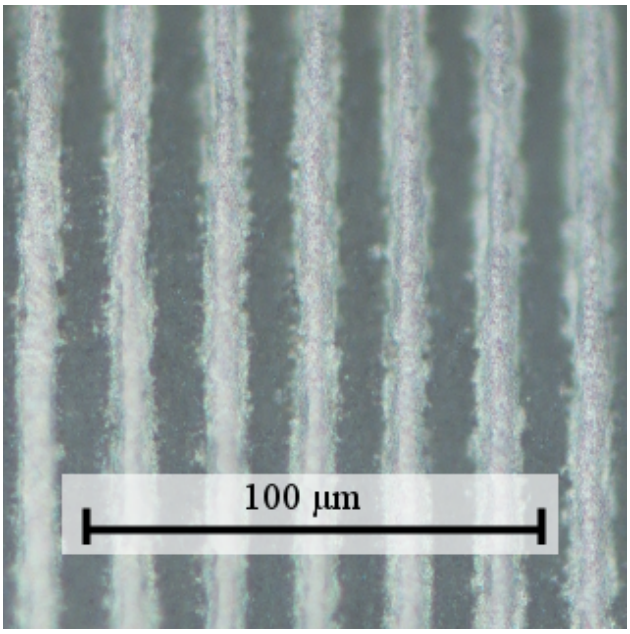

Figure 2.19: Unit cell of fabricated 10 µm aerosol jet printed polarizer grid.

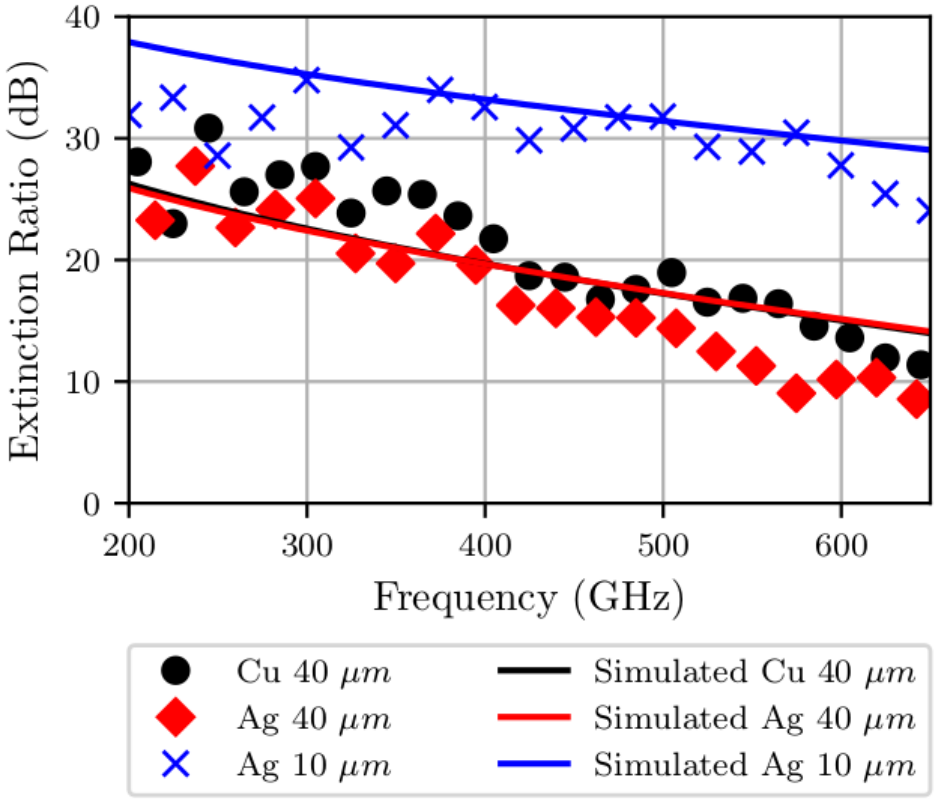

Figure 2.20: Simulated and measured polarizer rejection ratios.

be seen in Figure 2.20. Both the copper and aerosol jet printed polarizers designed for 40 µm line widths show almost identical performance over the measured frequency range, while the aerosol jet printed polarizer designed for 10 µm line widths shows a significant improvement in extinction ratio of approximately 12 dB compared to the 40 µm line width design.

2.4 Electroless Plating

While aerosol jet printing is capable of depositing features as small as 10 µm reliably, thick metal layers can be difficult to achieve while maintaining this fine line resolution. One possible method to reduce the time required to fabricate structures with sufficiently thick metal layers while maintaining fine line resolution is to combine aerosol jet printing with a metal plating process. Electroless plating of metal provides a means to deposit additional metal layers over a printed seed metal layer, without any design modification.

To demonstrate the feasibility of this method, a band-stop filter designed for operation

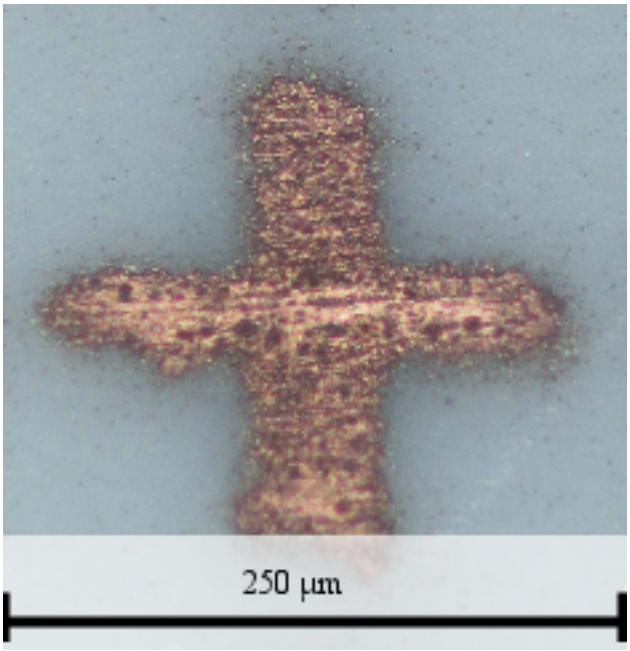

Figure 2.21: Unit cell of 550 GHz band-stop filter after electroless copper plating.

at 550 GHz has been aerosol jet printed in a single layer, at a print velocity of 2 mm/s, yielding a metal layer thickness of approximately 600 nm. Measured performance of this structure before plating can be seen in Figure 2.22. Next, this filter has been submerged in an electroless copper plating solution from Caswell Plating for 30 minutes, depositing an additional 2.5 µm of copper metal over the existing printed silver seed layer. A closeup view of final plated structure can be seen in Figure 2.21. As can be seen in Figure 2.22, while the unmodified structure results in a filter with poor performance, after plating performance improves drastically, with attenuation comparable to that of a filter printed with a much thicker metal layer. This process can be utilized to thicken the metal layer, and improve conductivity while reducing aerosol print time. Dimensions of the filter before and after plating are listed in Table 2.4.

2.5 Summary

Aerosol jet printing can provide a wide range of flexibility in fabrication of THz components. A number of materials can be deposited in layers from several hundred nanometers

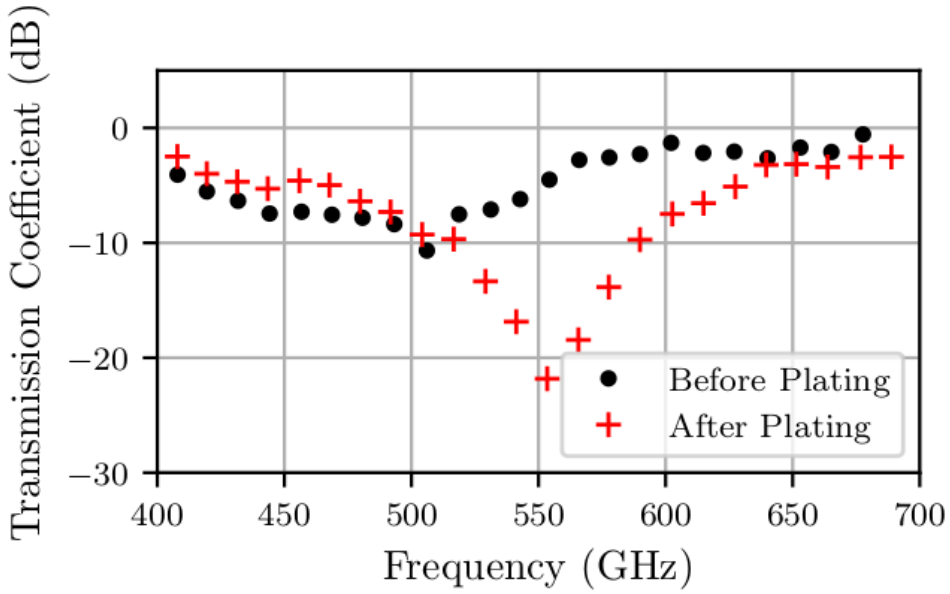

Figure 2.22: Measured transmission coefficient of 550 GHz band-stop filter, before and after electroless copper plating.

Filter		550 GHz Band-Stop	
		Before	After
Line Width (A) (um)	Designed	50	50
	Fabricated	31	34
Line Length (B) (um)	Designed	209	209
	Fabricated	199	203
Unit Cell (C) (um)	Designed	249	249
	Fabricated	249	249

Table 2.4: Electroless copper plated 550 GHz band-stop filter dimensions.

thick, to tens of microns. Aerosol jet printed silver metal has been shown to provide adequate performance in the fabrication of band-pass and band-stop filters, as well as polarization screens for operation to at least 700 GHz. Additionally, fabrication time can be significantly reduced by combining aerosol jet printing techniques with electroless plating of other metals to achieve the desired final metal thickness. The combination of methods presented, as well as the flexibility of aerosol jet printing, can provide a path for fabrication of a wide range of components operating in the THz frequency spectrum.

CHAPTER 3

RAPID PROTOTYPING OF RF OSCILLATOR WITH AEROSOL JET PRINTING

3.1 Introduction

Rapid component prototyping significantly reduces product development time and cost, as well as enables the fabrication of structures which would otherwise not be easily created through traditional subtractive manufacturing techniques. Recently, there has been focus on using additive manufacturing for development of radio frequency components such as antennas [85, 86, 45], passive circuit elements [87, 79, 88], as well as integration of active and passive elements [89].

With their ability to deposit a wide range of conductive and polymer materials, inkejt and aerosol jet printing technologies present a new technique for rapid production of RF circuits and systems. With the large standoff distance of aerosol jet printing, complete metallization of out-of-plane features can be achieved, enabling complete circuit fabrication without the need for additional processes typically seen in traditional circuit board fabrication. By reducing the time and cost associated with prototyping and small production quantities, designs can quickly be iterated to converge on an optimal solution.

In this chapter, two aerosol jet printed passive circuit elements are presented, as well as a printed oscillator circuit. The passive circuit elements, a transmission line and a microstrip resonator, form the fundamental building blocks necessary for the realization of the final oscillator circuit. Complete metallization of the oscillator circuit, including metallization of drilled via walls, will be accomplished through aerosol jet printing. This method of fabrication will allow for quick turn-around prototype fabrication on commercially available substrate material using packaged, off the shelf components.

3.2 Passive Circuit Elements

Two passive circuit elements have been simulated, printed and measured. These are a 50 Ω microstrip transmission line, and a microstrip resonator. The performance of these structures have been first designed and simulated using Ansys HFSS full-wave electromagnetic simulation software.

3.2.1 Microstrip Transmission Line Simulation and Fabrication

A microstrip transmission line has been designed for a characteristic impedance of 50 Ω. This line forms one of the fundamental building blocks necessary for the fabrication of the desired oscillator, as well as serve to verify metal layer conductivity and surface roughness models for design and simulation of other printed structures.

The 50 Ω microstrip transmission line (MSTL) is 231 µm wide, and 17.4mm in length. Reported conductivities of sintered silver nanoparticle metal layers can range from 10^6 S/m to 10^7 S/m, as reported in [87, 45, 90]. A silver conductivity of 10^7 S/m, as well as metal layer thickness of 2 µm with 0.5 nm of surface roughness are used to simulate the transmission line.

This MSTL was fabricated by printing four layers of silver nanoparticle ink. The line was printed using a deposition nozzle with a 200 µm diameter, and a standoff height of approximately 3.5 mm and a printing stage velocity of 1 mm/s, resulting in a metal layer approximately 2 µm thick. Ground pads have been printed on either side of the transmission line, to facilitate probing of the transmission line with Ground-Signal-Ground (GSG) probes. The final printed transmission line can be seen in the inset in Fig. 3.1. The printed metal is sintered at 200 °C for 1 hour, to achieve a highly conductive layer.

The performance of the printed transmission line was measured on a MPI TS150-THZ on-wafer probe station utilizing a Keysight N5227A PNA Microwave Network Analyzer, over a frequency range of 1 GHz to 40 GHz. Measured insertion loss at 10 GHz was approxi-

mately .037 dB/mm, while the simulated insertion loss at this frequency was approximately 0.043 dB/mm. At 40 GHz, measured insertion loss is approximately .12 dB/mm. Similarly sized transmission lines at this frequency fabricated from copper have shown reported insertion loss of approximately .06 dB/mm [91]. Fig. 3.1 compares measured vs simulated insertion loss of this transmission line. The top surface of the final printed transmission line has approximately 0.5 µm of surface roughness, as measured by a NanoMap-500LS Surface Profilometer.

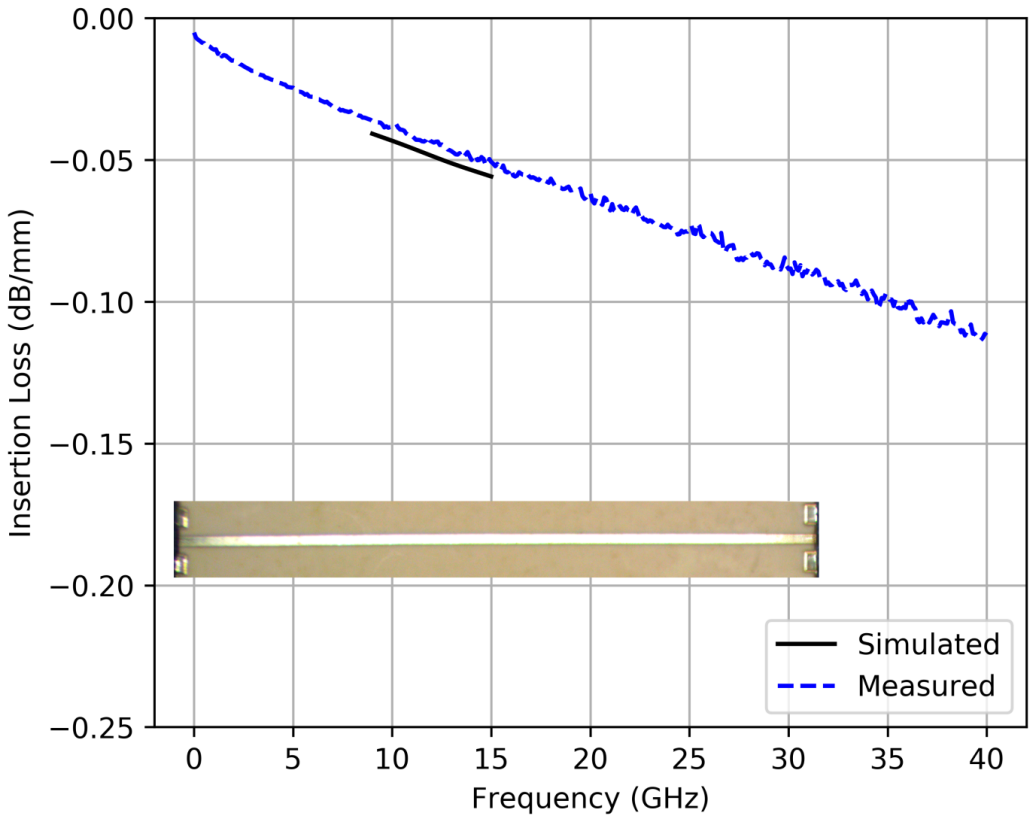

Figure 3.1: Simulated vs measured insertion loss printed transmission line. Inset: 17 mm transmission line with GSG pads.

3.2.2 Microstrip Resonator Simulation and Fabrication

A microstrip resonator has been designed for use as a resonant structure for an X-band fixed-frequency oscillator. This resonant structure is designed to have a band-stop characteristic,

which is necessary for proper operation of the final desired oscillator.

The structure is capacitively coupled to a MSTL. This is accomplished by printing a line which is 200 µm wide and approximately 6 mm long, separated from the transmission line by a 60 µm gap. The rest of the resonator is formed by a 200 µm wide line, 1.82 mm long, connected to a half-circle 2.42 mm in diameter, which forms a parallel-plate capacitor with the ground plane. The structure of the final printed resonator can be seen in Fig. 3.3.

Simulation was performed both by approximating the metal as a perfectly conducting layer, as well as a 2 µm thick layer with a conductivity of 10^7 S/m and surface roughness of 0.5 µm, as was measured for the final printed transmission line. The resonant frequency of the structure using a perfectly conducting metal layer was approximately 10.24 GHz, with an insertion loss of 20.78 dB. However, when simulated using parameters for printed silver, the resonant frequency shifted to 9.32 GHz, with an insertion loss of 3.73 dB.

The resonator was then printed with four metal layers, providing a final metal thickness of approximately 2 µm. The measured resonant frequency of this structure is 10.3 GHz, with an insertion loss of 4.3 dB. This measured resonance corresponds to the same structure simulated utilizing a perfectly conducting metal layer, however the insertion loss corresponds to simulation with a finite conductivity and 0.5 µm of surface roughness.

3.3 X-Band Oscillator

Using the simulated and measured transmission line and resonator results, an oscillator has been designed and fabricated for operation in the X-band frequency range. This is a fixed-frequency oscillator, fabricated on 4 mil (approximately 102 µm) thick Rogers Ultralam 3850HT LCP substrate material. All metal layers have been printed using the aerosol jet printing method.

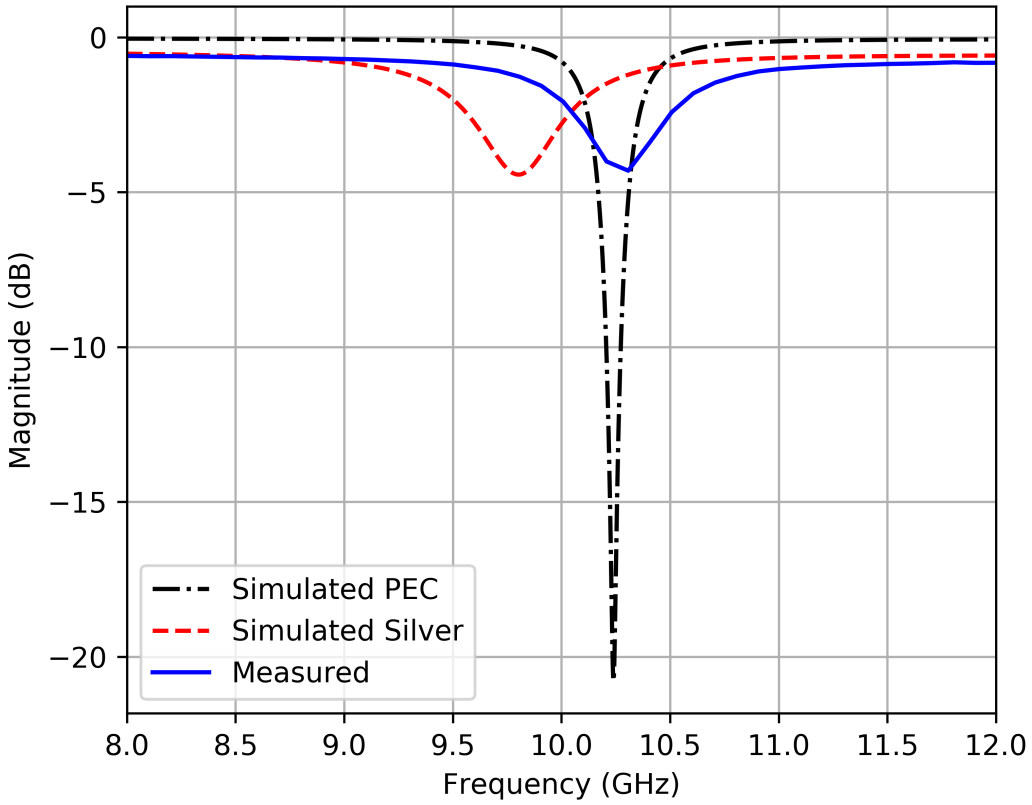

Figure 3.2: Simulated vs measured insertion loss of printed microstrip resonator.

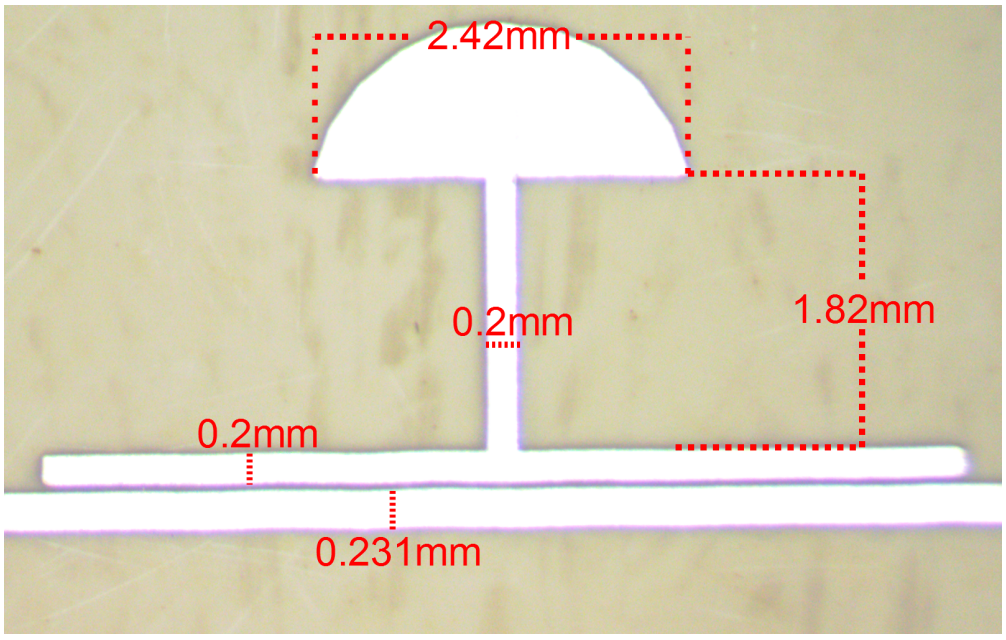

Figure 3.3: A photograph of the printed microstrip resonator.

3.3.1 Design and Simulation

The X-band oscillator design utilizes and Avago Technologies ATF-36163 pHEMT low noise transistor. S-parameters of the device have been simulated using a device model provided by Avago Technologies, for Keysight's Advanced Design System (ADS). The device is being operated in an unstable condition by means of adding a small inductance of a few nH between the source pins and ground. A load reflection coefficient of $\Gamma_L = 0.1 + j0.2$ has been selected to provide sufficient instability for oscillation. A microstrip matching network has been designed to transform a 50 Ω load impedance to this desired value. An additional impedance matching network has been designed to transform the source impedance presented by the resonator to match the input impedance of the transistor.

Time-domain simulation of this circuit results in a fundamental resonance at 10.1 GHz, with an output power of approximately -3 dBm. The power of the second harmonic at 20.2 GHz is approximately 12 dB lower than the fundamental frequency of oscillation.

3.3.2 Fabrication

Using the microstrip line dimensions found through simulation, this oscillator was fabricated and measured. Holes for vias between the top metal layer and the ground plane are first mechanically drilled using a drill bit 300 µm in diameter. Following this step, the existing 17 µm copper foil is chemically removed using a sodium persulfate solution. After the substrate has been prepared, the top metal layer and ground plane are printed using the above print parameters. Thermal sintering is performed after printing each complete metal layer, performed at 200 °C for 1 hour.

Critical to the operation of this circuit are conductive vias, which are necessary both for terminating the oscillator, as well as for providing conductive paths for the DC biasing network. The vias necessary for this circuit were formed by rotating the sample stage by 45° around one axis, exposing the walls of the drilled holes directly to the print head. A rectangular pattern was printed along the walls of each via, resulting in a conductive

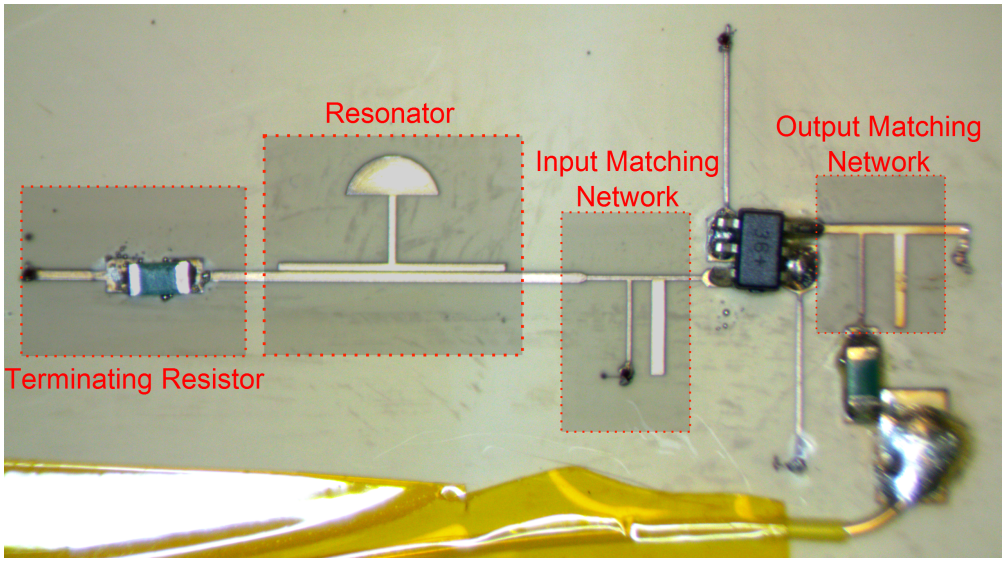

Figure 3.4: A photograph of the printed oscillator circuit.

path between the ground plane and the microstrip lines printed on the top layer of the substrate. After the final sintering step is performed for the printed vias, each of the necessary components (resistors, DC bias line, and transistor) were attached using solder paste (Kester ESP265), and hot air reflow soldering. The final fabricated circuit is shown in Figure 3.4.

3.3.3 Measurement

This circuit was measured using an HP 8562A spectrum analyzer, and a 425 µm pitch ground-signal (GS) probe. An external bias tee was used to block DC voltage from the RF input of the spectrum analyzer. At a bias point of $V_{gs} = 2.5$ V, the transistor drew approximately 20 mA of current. Output of the oscillator was measured to be 2.65 dBm at a resonant frequency of 8.513 GHz, with approximately 1 dB of loss across the GS probe tip and coaxial cable used. Fig. 3.5 shows the measured fundamental frequency of the printed oscillator. This measurement was performed with a resolution bandwidth of 10 kHz. The power in the second harmonic of the oscillator was found to be 22 dB lower than at the fundamental frequency at 17.03 GHz. The DC-RF conversion efficiency is approximately 3.68%. Initial phase noise measurements at 1 kHz offset from the carrier frequency is approximately -37 dBc/Hz. This

can likely be reduced through design modifications, as well as improvement in via fabrication techniques.

The measured frequency of oscillation of the fabricated circuit is lower than the frequency predicted through simulation. A possible cause of this is due to poor metallization of the via walls, which is likely a result of poor hole drilling quality. As a result of mechanically drilling the soft LCP material, tearing occurs throughout the via, as well as at the entry and exit of the LCP, resulting in poor metallic connection between the top and bottom layers of metal to the metal deposited on the via walls. To simulate the impact of poor quality metallization of the vias, the simulation has been modified to include an inductance of approximately 60 nH between the terminating 50 Ω resistor and ground, and 20 nH between the transistor gate bias line and ground. This has resulted in a significant deviation in the fundamental frequency of oscillation, shifting down from 10.1 GHz to 8.48 GHz. Additionally, the power of the second harmonic of the oscillator has decreased, to approximately 20 dB lower than at the fundamental frequency, which agrees well with the measured results.

3.4 Summary

In this chapter, aerosol jet printing is utilized in the rapid fabrication of an oscillator circuit. Two passive circuit elements have been presented: a 50 Ω transmission line, and a band-stop microstrip resonator. Transmission line measurements have supported printed metal conductivity and surface roughness approximations necessary for the accurate modeling and simulation of other printed microstrip structures.

An oscillator circuit has been presented, in which all metal layers have been printed using aerosol jet technology, including metallized vias. Measurement of this oscillator, and subsequent simulation, has demonstrated that via metallization quality can have a drastic impact on the circuit performance. While this process will require improvement in the future, this demonstrates the capability of aerosol jet printing systems to completely realize microwave and millimeter-wave circuits.

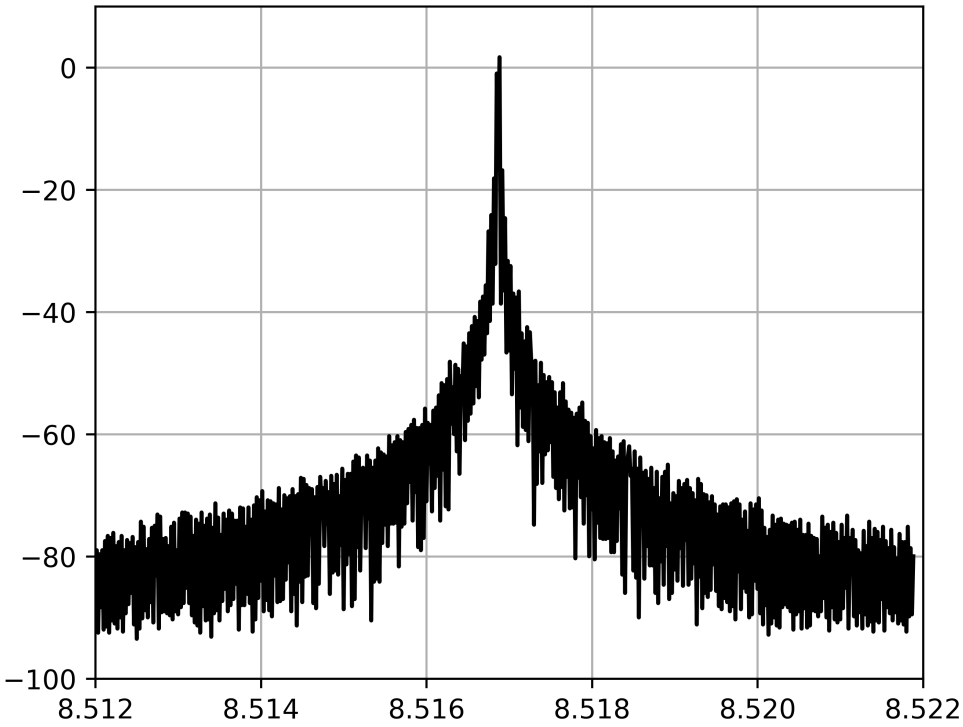

Figure 3.5: The measured power spectrum of the printed oscillator fundamental output frequency.

CHAPTER 4

HYBRID ADDITIVE AND SUBTRACTIVE PROCESSES FOR ELECTRONICS PACKAGING

4.1 Introduction

As operating frequencies continue to increase into the millimeter-wave range and beyond, unwanted parasitic effects of component packaging, such as added capacitance and inductance, becomes an obstacle which must be addressed. Conventionally, to overcome some of these limitations, unpackaged devices are directly wire- or ribbon-bonded to transmission lines and other circuit board traces necessary for proper device operation [7, 8]. While an improvement over typical packaged components, these bonding wires and ribbons present unwanted inductance and resistance, and are difficult to implement due to the special handling required to achieve good metal bonding. Furthermore, these techniques do not allow for high density integration of RF systems.

With the growing body of work over recent decades in applying AM techniques for fabrication of electronic circuits, interest has turned towards applying these processes for fabrication of high functional density systems operating in the microwave and millimeter-wave frequency range.

Over the last few years, there has been growing interest in the use of additive manufacturing (AM) for the fabrication of high functional density systems operating in the microwave and millimeter-wave frequency range. Towards this goal, many passive components such as transmission lines [92, 93], waveguides [37], antennas [45, 94], as well as capacitors, inductors and resistors [44, 95] have been demonstrated using AM. Direct printing of transmission lines on substrates through AM has also been explored. However, when combining active circuit elements with circuits fabricated by methods such as inkjet or aerosol jet printing, the forces necessary to attach a bond wire to these printed metals can present great difficulty

in achieving a quality bond [53]. To avoid direct bonding of chips on printed traces, there has been work focusing on the incorporation of active components with thick-film additively manufactured structures and circuits [96, 97].

By embedding active devices within the substrate of choice, interconnection lengths between bonding pads for both RF and DC lines can be reduced, significantly reducing unwanted parasitic inductance due to bonding wires. Chip-first processes have been developed, where devices are initially attached to an appropriate carrier, with dielectric materials subsequently deposited by lamination [98, 99, 21] or spin-coating [100, 18]. These dielectrics are then processed by means of laser ablation, or photolithography in the case of photosensitive dielectrics. Metal layers are deposited and processed by traditional lithographic processes. Chip-last approaches have also been developed, in which metal and dielectric layers are deposited and processed, with the active device attached at the end of the fabrication process [101], [102]. These processes provide device connections with very low insertion loss [17, 103, 104], and can be used to process many devices simultaneously. However, these processes require good planarization of devices, either by means of varied pocket depths in substrates, or by planarization of the deposited material.

Direct-write technologies of conductive films present a method by which chip-to-chip and chip-to-board connections can be fabricated through selective deposition of dielectric and metal materials, eliminating the requirement of planarization of devices to be encapsulated. Chip-to-chip connections for high-speed differential signaling [55], and chip-to-board connections [56], have been shown to reduce insertion loss over equivalent wire bonds [4], facilitating operation up through 110 GHz [105]. Dielectric ramp structures can also be reduced and/or eliminated by placing components in a pocket fabricated within the substrate, further reducing the unwanted parasitic effects of each interconnection [57]. While these preliminary results demonstrate a reduction in losses associated with connections between transmission lines, such performance has not been demonstrated with connection to a monolithic microwave integrated circuit (MMIC). A chip-first method, in which devices are attached to a

ground plane with substrate material and supporting circuitry subsequently deposited, has been shown to provide very low-loss performance through 67 GHz [106]. Among the many AM technologies, aerosol printing is attractive for such applications due to its ability to print fine resolution structures on planar and non-planar surfaces from a large standoff distance, enabling the integration of devices with varying thickness without the need for pre- or post-planarization. However, printing of thick structures (>100 µm) with good resolution using this approach is still a challenge due to slow printing speeds. By printing metal interconnections, bond wire height can be virtually eliminated, and a transmission line with a controlled impedance can be brought to the edge of the device, improving circuit performance and robustness.

This chapter demonstrates a hybrid process whereby a thick substrate having deep cavities to accommodate passive and active elements is fabricated using a conventional lithographic method, and interconnections and supporting circuitry are fully aerosol jet printed. To the best of our knowledge, this is the first demonstration of an aerosol jet printed interconnection to an embedded MMIC and a package. Printed interconnections to both passive and active devices, formed by depositing a constant width line to the edge of the device, is demonstrated operating through 60 GHz. The ability to iteratively deposit metal will be demonstrated, both to achieve desired circuit performance and to repair defects created during the fabrication process. Additionally, compatibility challenges of printed metals over semiconductor materials will be demonstrated and discussed.

4.2 Design and Fabrication

Utilizing a hybrid subtractive and additive manufacturing process, low-loss commercially available substrate materials can be used to quickly fabricate microwave and millimeter wave circuits. A liquid crystal polymer (LCP) substrate, Panasonic RF705T, is used here due to its low-loss characteristics over the frequency range of interest, with a dielectric constant (ϵ_r) of 3.1, and a loss tangent (tan-δ) of approximately 0.004. A substrate thickness of 100 µm

is used, equal to the thickness of each device to be embedded, eliminating the requirement of any additional fillets to be formed and minimizing losses associated with the transitions.

Substrate preparation consists of a two-step etching process, beginning with the patterning of the existing copper cladding by means of a standard photolithographic process. This patterned copper forms a hard mask, capable of withstanding the etchant solution utilized to selectively etch LCP. The exposed LCP material is etched using a solution consisting of 40 w.t. % potassium hydroxide, 30 w.t. % ethanolamine, and 30 w.t. % water [107]. This solution is heated to 85° C, providing an etch rate of approximately 2.5 µm per minute. After the exposed LCP has been etched, the substrate is rinsed in deionized water and blown dry using nitrogen gas. Each of the cavities are filled with an acetone-soluble resist material to preserve the RF ground plane, and the remaining exposed copper is chemically stripped away. After etching, through-substrate features, including all pockets as well as vias to ground, have a tapered wall of approximately 56°. This non-vertical feature provides an ideal surface on which metal can be deposited without the need for additional manipulation of the substrate to expose vertical surfaces. This tapered wall also provides a good transition between the surrounding LCP, and the epoxy used to fill the pocket around each device, resulting in a void-free surface onto which silver metal can be deposited.

After the substrate has been etched, devices are attached to the exposed ground plane using a silver epoxy, Ablestik 84-1LMISR4. After the epoxy has been cured, the remaining spaces around each die are filled with a UV curable epoxy, Formlabs High Temp resin, which has a heat deflection temperature T_g of 238° C at 0.45 MPa , enabling it to withstand the high temperature required to sinter the printed silver nanoparticle ink.

After curing this epoxy, silver ink structures are aerosol jet deposited to form transmission lines, interconnections to each device, and biasing lines for each active device to be measured. Diluted Clariant Prelect TPS 50 G2 silver nanoparticle ink is atomized using the ultrasonic atomization process, and is carried to the print head with a gas flow rate of 23 SCCM. In the print head, the ink stream is combined with a focusing sheath gas at a flow rate of 50 SCCM.

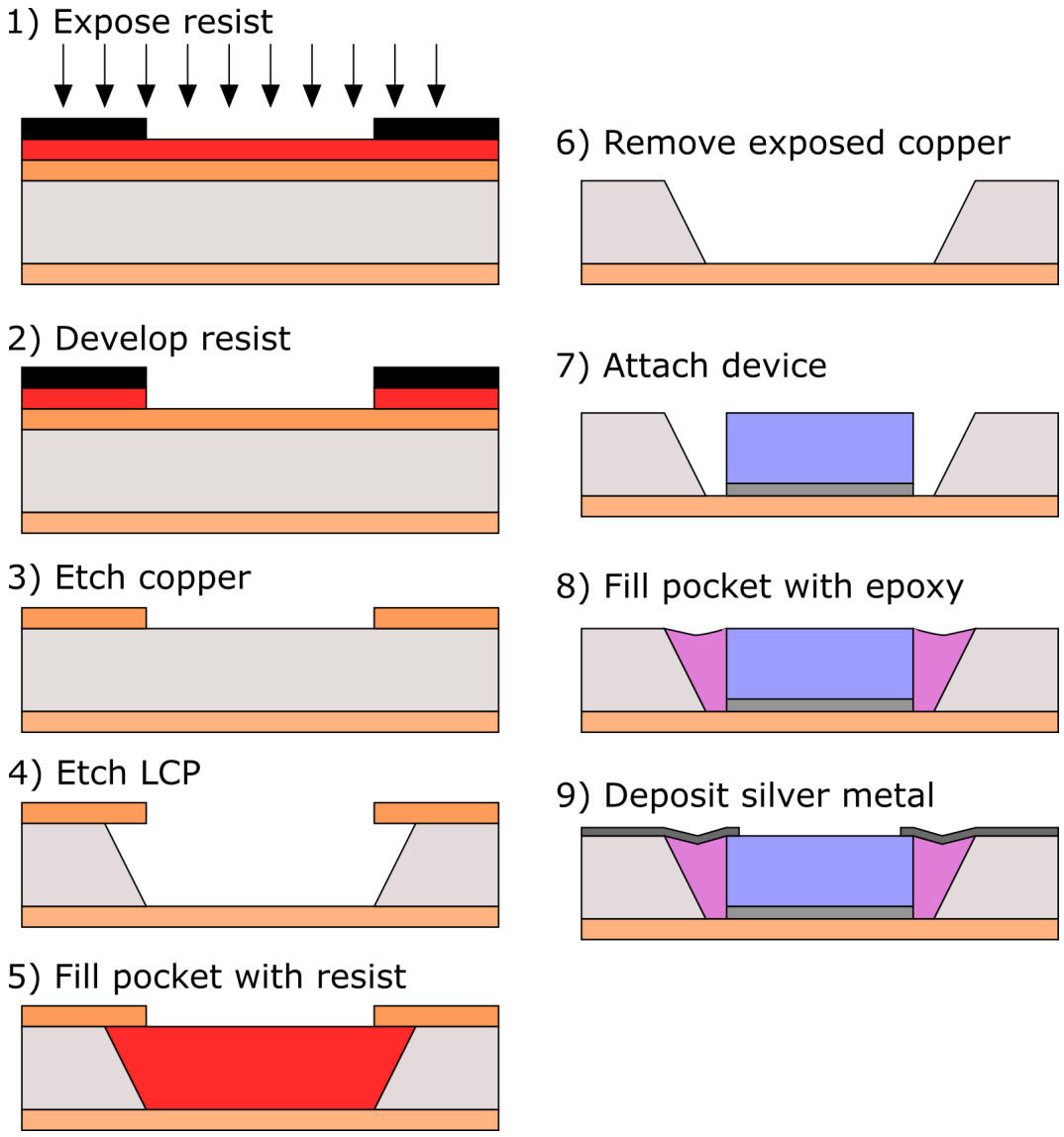

Figure 4.1: Substrate preparation process.

This column of ink is directed towards the substrate through a print nozzle with a 150 µm diameter, providing a line width of approximately 25 µm, with 1.5 µm thickness. Two layers are deposited, providing a final metal thickness of 3 µm. This ink is sintered at 180 °C for 3 hours. Figure 4.1 outlines the complete substrate preparation and metal deposition process.

A series of trenches have been fabricated to demonstrate the ability to form low-loss interconnections over the epoxy material to be deposited around each die. These trenches represent the anticipated gap between each die and the surrounding LCP material. While

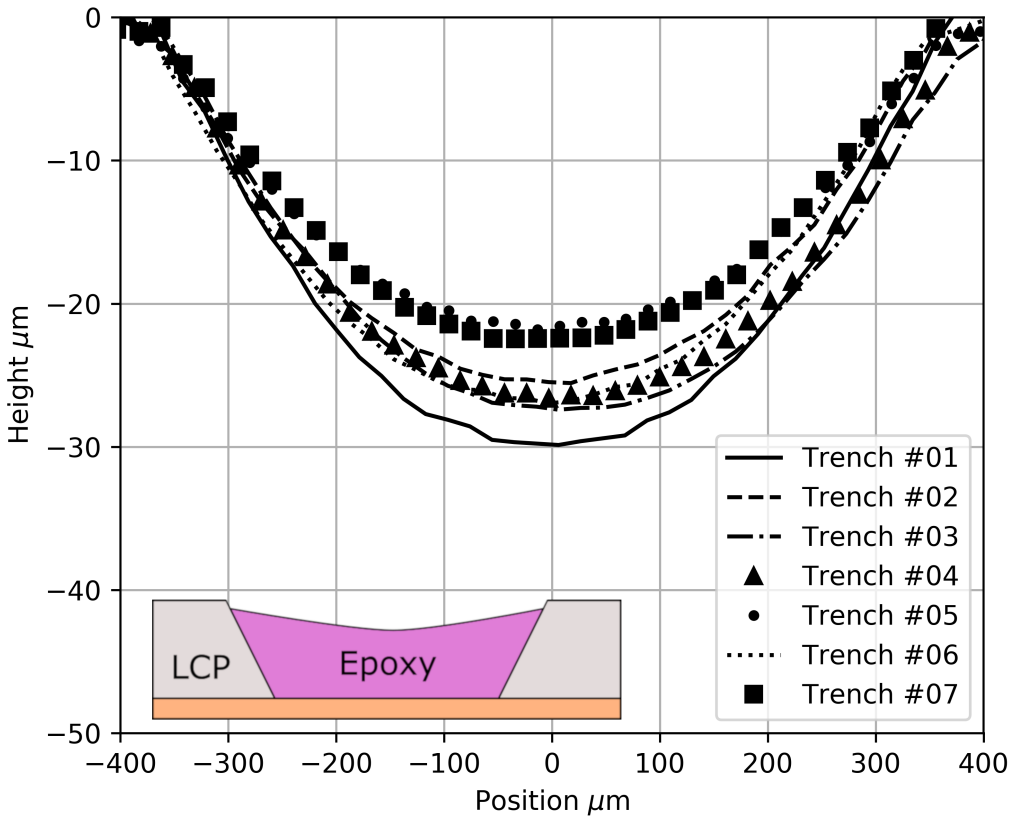

Figure 4.2: Profilometer measurement of trenches in LCP substrate. Inset shows cross-section representation of a filled trench.

the particular dielectric properties of this material have not been characterized, many printed materials have been shown to have a dielectric constant of approximately 3 [108] with a loss tangent ranging from 0.01 to 0.04. This material is assumed to have a dielectric constant of 3, and a loss tangent of 0.04. Due to lateral etching of the LCP during the wet-etching process as well as some over-etching to ensure all existing LCP has been eliminated from the cavity, the final widths of these trenches are significantly wider than the 200 µm gap which will surround each device, at approximately 650 µm.

Figure 4.2 shows a two-dimensional profile of each trench after filling with epoxy, measured using a NanoMap-500LS contact surface profilometer. As can be seen, each trench is slightly under filled, resulting in an average drop of approximately 25 µm from the surface of the LCP. Simulation of a 650 µm wide trench having a 265 µm wide transmission line

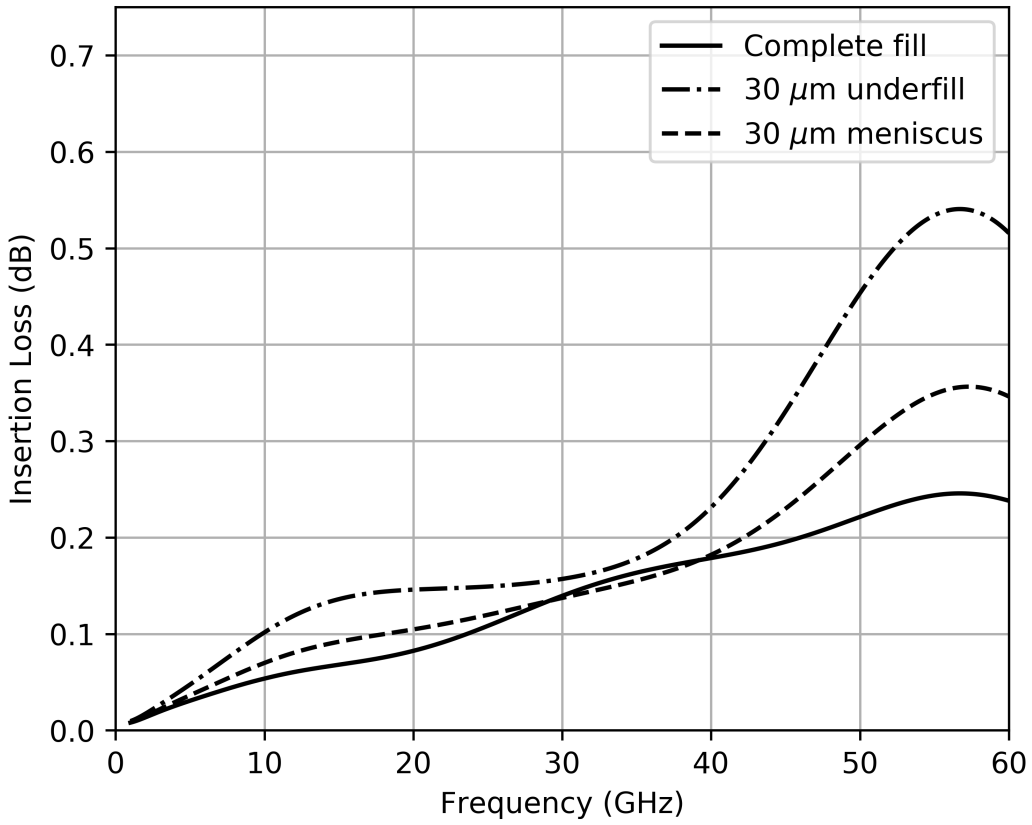

Figure 4.3: Simulated insertion loss of printed interconnection over trench.

passing over top is shown in Figure 4.3. Three configurations are considered: a fully filled trench, a trench exhibiting a concave meniscus 30 µm deep, and an under filled trench with the epoxy surface 30 µm below the surface of the surrounding LCP substrate. As can be seen, insertion loss of the fully filled configuration is low, remaining below 0.25 dB through 60 GHz. Insertion loss of a constant width line printed over a trench with a 30 µm concave meniscus increases to a maximum of 0.36 dB, and to a maximum of 0.55 dB for the under filled case. These losses are attributable to the changing transmission line impedance over this under filled section, and can be minimized by shaping the interconnection to maintain a 50 Ω impedance across the surface.

Two bare-die devices are used to demonstrate the ability to fabricate a low-loss wide-bandwidth connection by aerosol jet printing to devices embedded in the LCP substrate. A 0 dB attenuator capable of operating from DC to 40 GHz, Mini-Circuits KAT-0-DG+,

is used to evaluate the performance of each printed interconnection without introducing excessive additional losses. Finally, a low-noise amplifier (LNA), Quorvo TGA2512, is used to demonstrate the compatibility of this process with active components. An LNA is used in this application to reduce any potential unknown effects due to power dissipation in the printed silver transmission lines and interconnections. The maximum RF power considered here is -3 dBm, or 500 µW.

Each circuit is fabricated by printing a transmission line 255 µm wide to within 100 µm of the edge of each device, where the line width is reduced to slightly less than the width of each bond pad on the chip, and printed to completely cover each pad. To facilitate probing of this circuit, a coplanar waveguide (CPW) with a conductor width of 203 µm, and gap width of 60 µm, is used as a probe pad. Each ground strip of this CPW is connected to RF ground by pockets patterned into either side of the structure. This CPW line is transitioned to the microstrip transmission line over a length of 100 µm. Images of each of these fabricated circuits are shown in Figures 4.4, 4.6, and 4.8.

4.3 Measurement

Due to overspray which occurs during the fabrication process, the final dimensions for each line are slightly larger than the design goal. Each transmission line has been designed with a goal of 255 µm wide line, where the final fabricated width is approximately 265 µm. Each of the CPW pads used to facilitate probing of the circuits have a final conductor width of approximately 220 µm, with a gap of 40 µm. The deviation in final line dimensions does not significantly impact circuit performance, due to significantly reduced metal thickness at the edge of each printed feature.

Performance of each device has been measured on an MPI TS150-THZ probe station, and Keysight N5227A PNA Microwave Network Analyzer, using GSG probes with 250 µm pitch. An image of the final fabricated interconnection over a trench is shown in Figure 4.4. Insertion loss of each of these connections over a trench can be seen in Figure 4.5. This

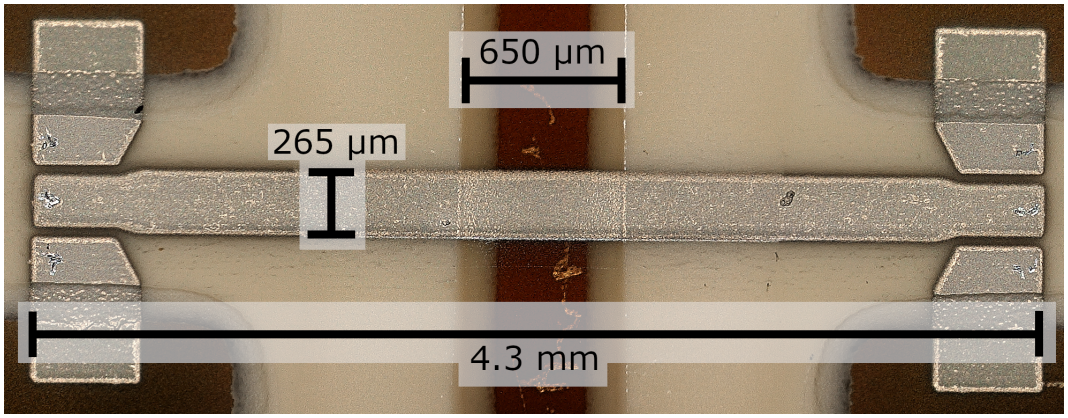

Figure 4.4: Fabricated interconnection over trench.

insertion loss is calculated as:

$$IL^{Trench} = S_{21}^{Thru} - S_{21}^{Meas} \tag{4.1}$$

where S_{21}^{Meas} is the total measured insertion loss of each transmission line with its associated interconnection with a total length of 4.3 mm, and S_{21}^{Thru} is the measured insertion loss of a 3.9 mm transmission line over LCP only. As is shown, the measured performance of each of these connections agrees well with simulation, with an average insertion loss of 0.15 dB at 40 GHz. At higher frequencies, the characteristic impedance of the interconnection changes due to the underfilled trench, resulting in an increase in effective loss. By tailoring the line dimensions to maintain a constant impedance throughout the transition region can greatly reduce this loss at high frequencies.

In Figure 4.6, the final fabricated circuit connecting a 0 dB attenuator is shown. The distance from the edge of the die the edge of the surrounding LCP is approximately 450 µm, shorter than the 650 µm distance considered for the individual interconnection over a trench. Insertion loss of each interconnection is shown in Figure 4.7. This insertion loss is calculated as:

$$IL^{Atten} = \frac{1}{2}\left(S_{21}^{Thru} + S_{21}^{Dev} - S_{21}^{Meas}\right) \tag{4.2}$$

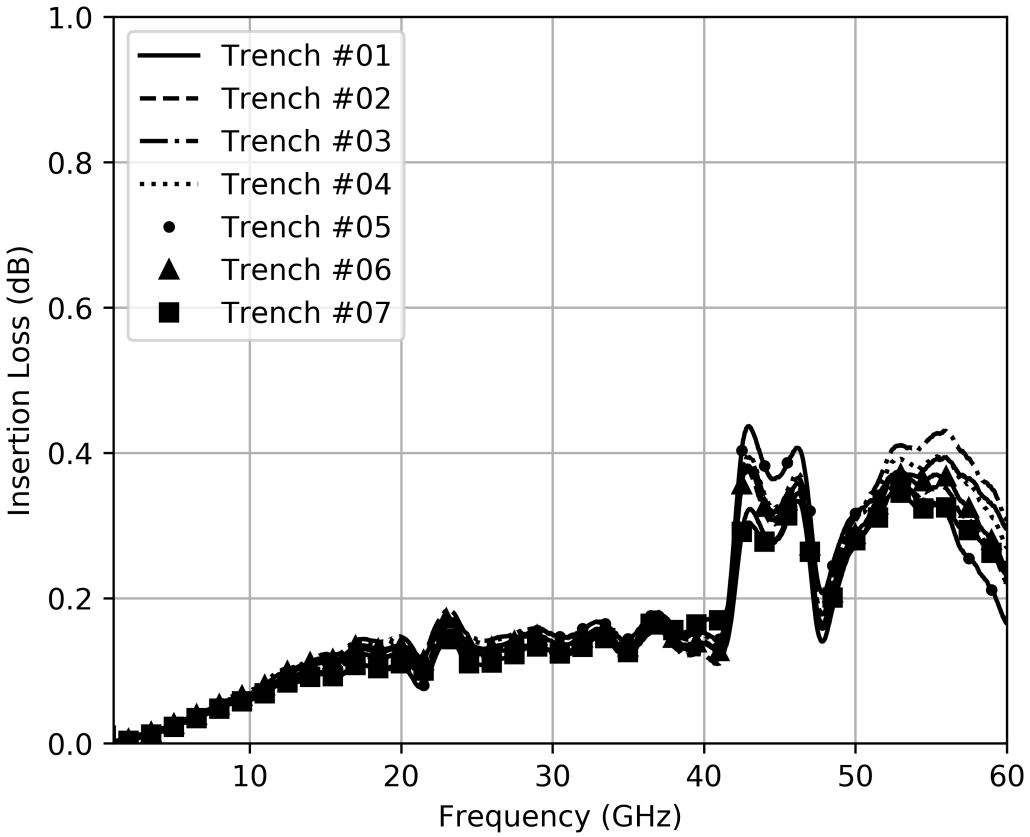

Figure 4.5: Insertion loss of interconnection over each trench, as calculated by Equation 4.1.

where S_{21}^{Meas} and S_{21}^{Thru} are the total measured insertion loss and the measured insertion loss of a zero-length through line respectively, and S_{21}^{Dev} is the device insertion loss as measured directly through a representative device with no external connections. As can be seen in Figure 4.7, each connection introduces approximately 0.15 dB of insertion loss at 23 GHz, and less than 0.2 dB at 40 GHz. The loss of each interconnection remains low throughout the measured frequency range, and can be further improved by reducing the gap surround each device, as well as by tailoring the line dimensions over the epoxy filler to maintain a constant impedance to the device edge.

Figure 4.8 shows one of the fabricated circuits connecting to an LNA. The RF input line can be seen in the lower left, with RF output in the lower right, and the DC biasing line connecting to the top of the die. The biasing line has been printed over a 100 pF capacitor, as specified by the device manufacturer. Additional leads have been attached to the board for

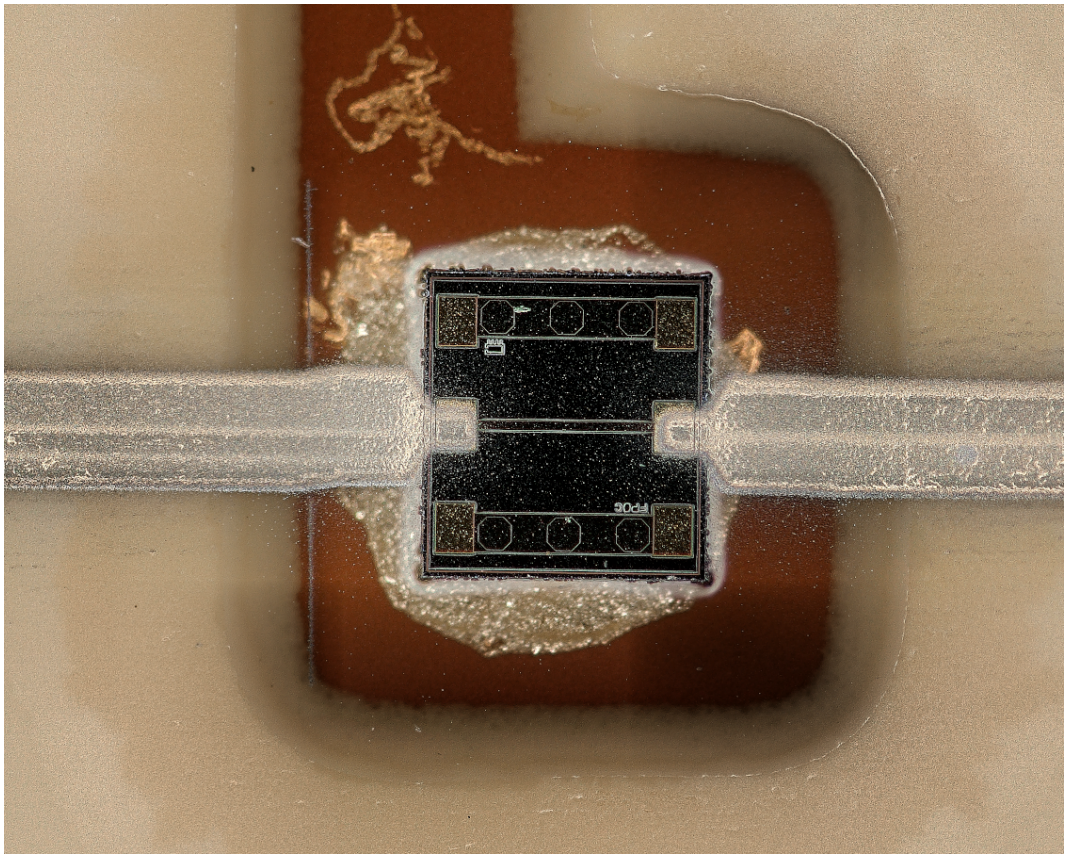

Figure 4.6: Fabricated interconnection to 0 dB attenuator.

connection to an external power supply for biasing of each amplifier. A ground lead, and a positive bias lead for each amplifier, are attached to the board by means of a conductive silver epoxy, MG Chemicals 8331S. Due to an offset of approximately 100 µm from their intended positions, each transmission line has a slight bend, allowing for a symmetric transition from the width of the transmission line to the width of the RF bonding pads.

Figure 4.9 shows the measured gain performance of two LNA circuits compared to the amplifier data sheet. A DC bias of 5 V is applied, drawing approximately 93 mA of current. Both fabricated circuits demonstrate similar gain, which is slightly less than the manufacturer provided data, due to several ohms of series resistance in the biasing circuit as a result of the various epoxies used for attaching leads and the die itself. RF input return loss and output return loss match well with the amplifier data sheet, as can be seen in Figures 4.10 and 4.11.

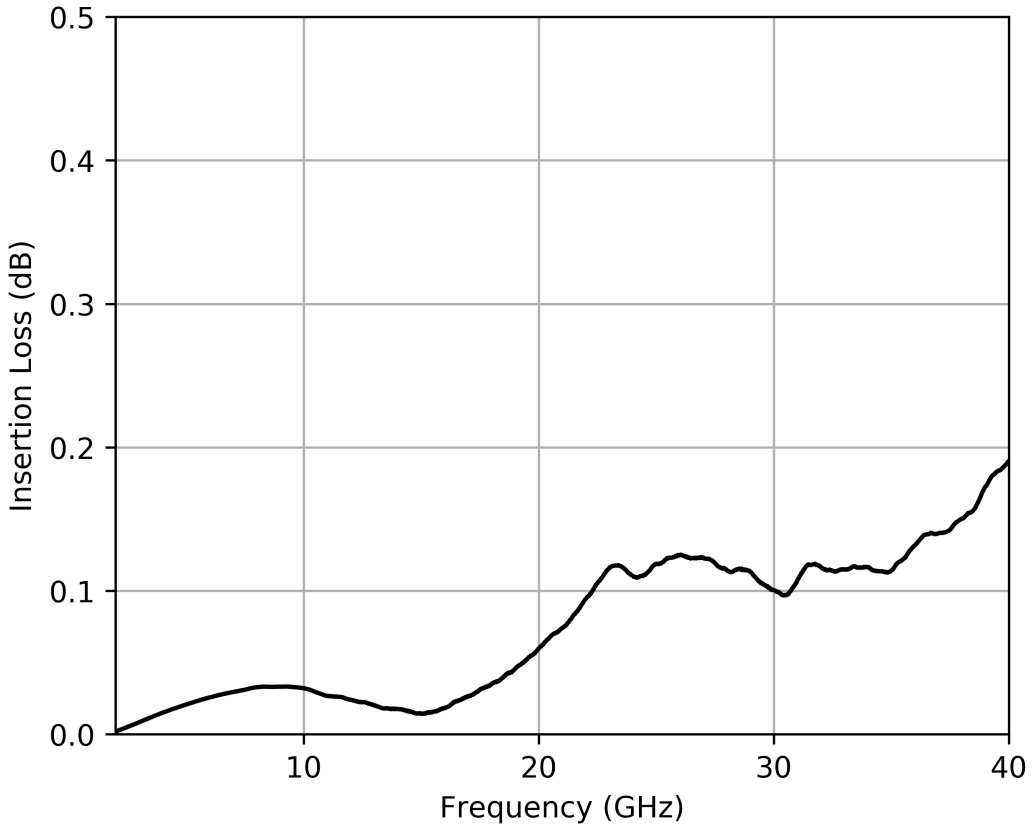

Figure 4.7: Per-interconnection loss measured through 0 dB attenuator, as calculated by Equation 4.2.

4.4 Rework of printed lines

One unique advantage of utilizing an additive process to deposit metal structures, either complete circuits or interconnections between devices and boards with existing metal traces, is the ability to iterate the deposition process to achieve desired performance characteristics. Figure 4.12 demonstrates the insertion loss of a 4.5 mm long transmission line printed over a trench, measured with different metal thicknesses. Initially, a very thin layer of silver metal was deposited, less than 1 µm thick. Measured performance of this line is rather poor due to high resistance, with an insertion loss of nearly 4.5 dB at 60 GHz. An additional 3 µm of silver was then deposited over the top of this line, and remeasured. Performance of this thickened line improved greatly, with total insertion loss at 60 GHz reduced to less than 1.75 dB. This ability to iteratively deposit material can also be applied to deposition of

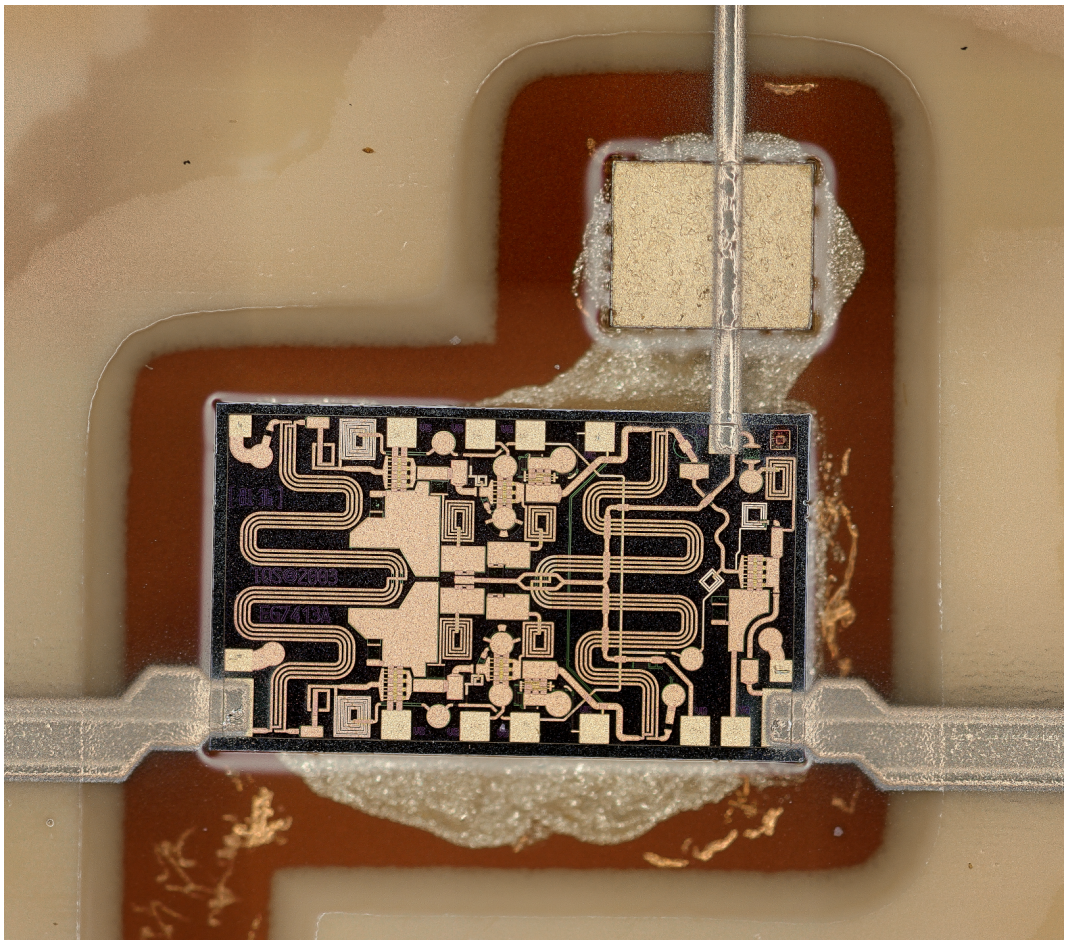

Figure 4.8: Fabricated connections to amplifier MMIC.

impedance matching circuits, as well as deposition of other materials, such as for fabrication of printed resistors or capacitors.

Another case in which this iterative deposition process can be useful is in the repair of interconnections which have failed due to thermal stress. The left image seen in Figure 4.13 shows an attenuator connection which has cracked due to thermal stress. This crack is approximately 2 µm wide, at the interface between the GaAs die and the surrounding epoxy material, resulting in an open circuit. An additional 3 µm of silver metal was deposited on top of the existing printed traces, and cured for 3 hours at 180 °C on a hot plate, with a heating and cooling temperature gradient of approximately 5 °C per minute. The repaired connection is shown in the right image of Figure 4.13. Measurement of this circuit after repair shows insertion loss through the device matches well to the device which did not

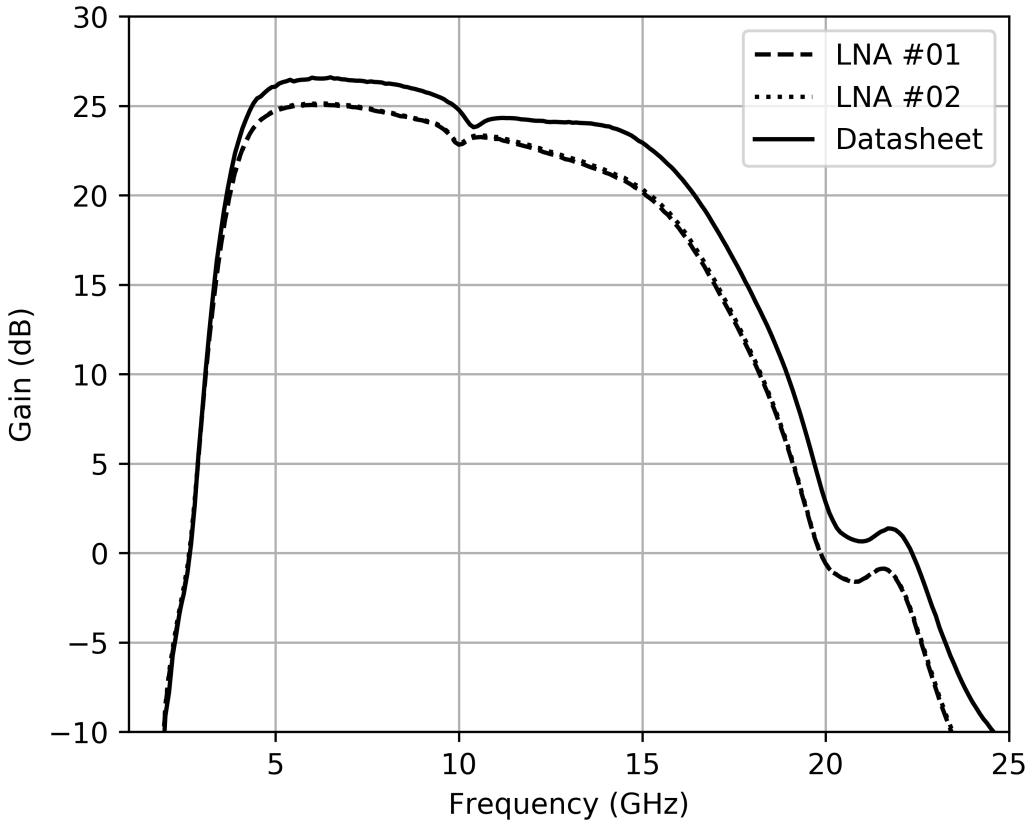

Figure 4.9: Gain performance of amplifier MMIC with printed connections.

exhibit any cracking, as can be seen in Figure 4.15.

4.5 Diode effects of Ag on GaAs

One possible unwanted effect which can be introduced through direct writing of interconnections to bonding pads is the unintentional formation of a Schottky diode due to a metal-semiconductor contact where silver is printed over an area lacking any passivation. Ag/GaAs diodes have been demonstrated by [109]. In this instance, the 0 dB attenuators considered are formed on a GaAs substrate, with an exposed area of GaAs at the edge of the die. By printing silver directly over this area of exposed semiconductor, a diode is unintentionally formed. Figure 4.16 shows the measured current vs applied voltage of the attenuator circuit shown in Figure 4.6. A schematic representation of this configuration is shown in Figure 4.17. This unintentional diode has the possibility of introducing unwanted

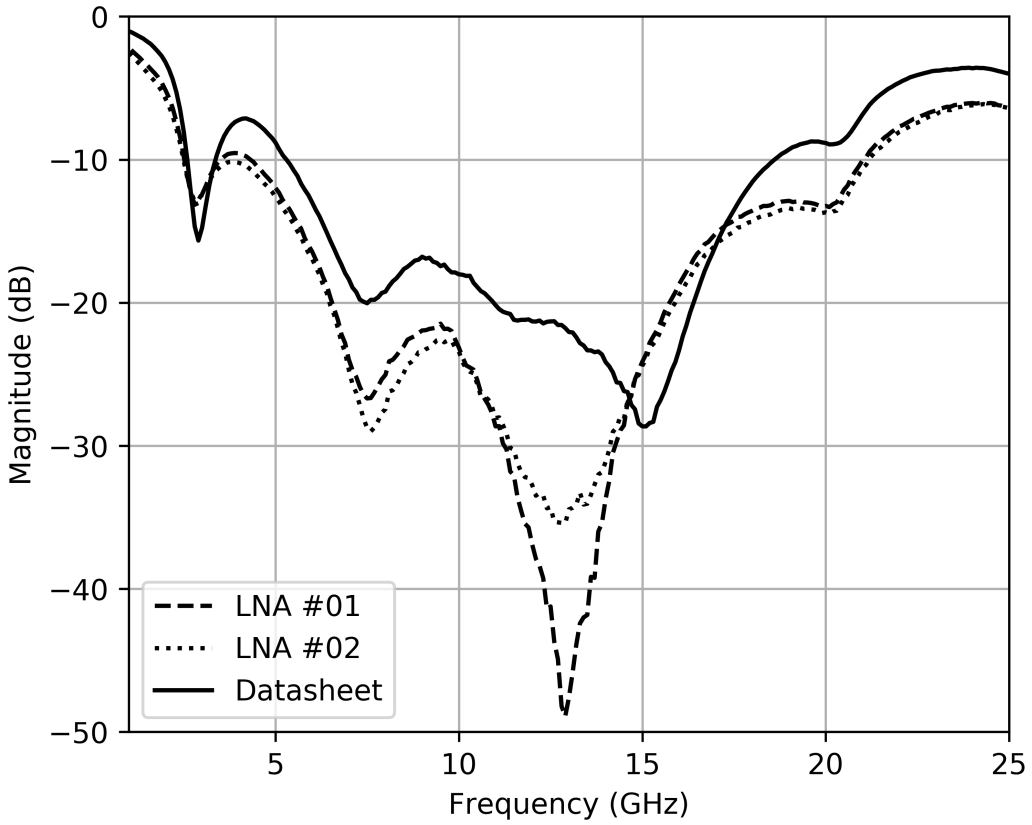

Figure 4.10: Amplifier circuit input return loss.

harmonic content in applications where voltages can exceed the diode turn-on voltage. However, this effect can be reduced or eliminated by the careful deposition of an insulating material over any exposed semiconductor material where metal is to be printed.

4.6 Summary

As operating frequencies continue to increase, unwanted parasitic effects of component packaging need to be mitigated and/or eliminated. By embedding devices in the substrate, as demonstrated here using a hybrid process, controlled impedance lines can be extended to the edge of the device, greatly reducing the losses associated with traditional wire bonding, providing a low cost path for device integration operating into the mm-wave frequency range and beyond. Interconnections have been demonstrated operating through 60 GHz, with insertion loss well below 0.5 dB, which can be further reduced by leveraging AM processes to tailor

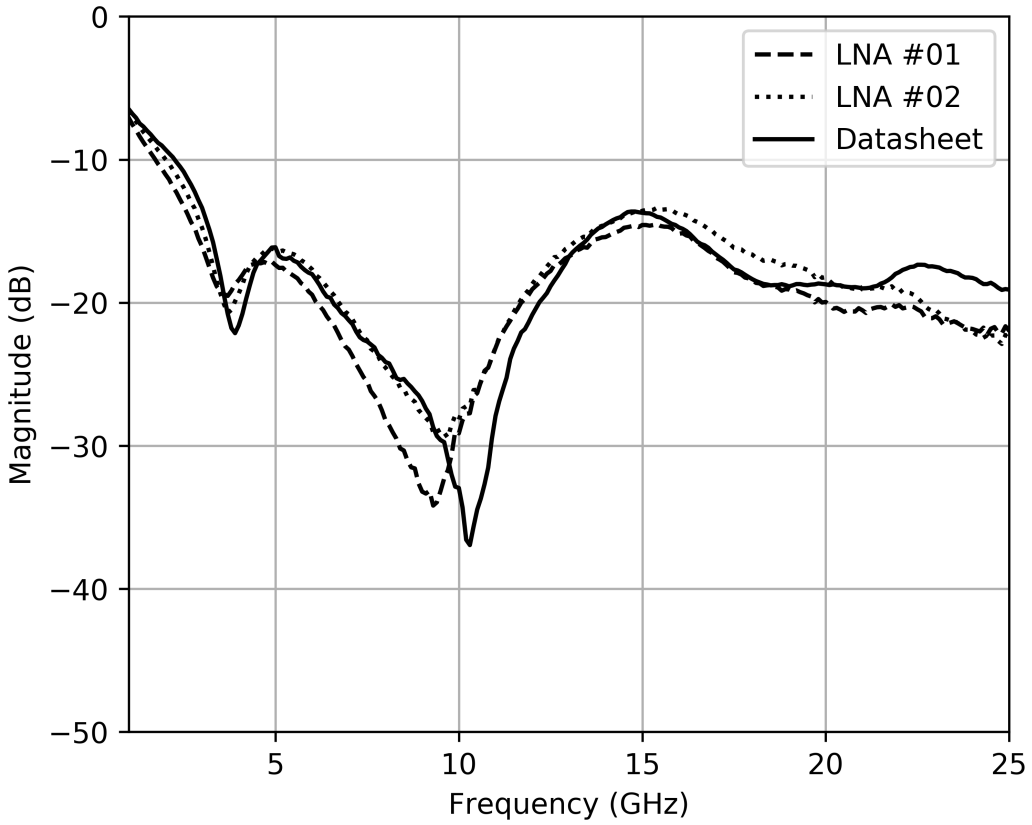

Figure 4.11: Amplifier circuit output return loss.

circuit geometry in real-time to achieve desired circuit performance. Compatibility with bare-die devices has been demonstrated operating through 40 GHz with per-interconnection insertion loss below 0.2 dB, as well as compatibility with active RF MMICs. With the flexibility of additive processes, requirements of device positioning can be relaxed and adjusted for in real-time. This per-interconnection loss compares well to that demonstrated in [106]. While there exists a possibility of the unintentional creation of a diode within the signal path by depositing metal directly over a semiconductor material, this effect can be reduced or eliminated entirely by depositing an insulating material (e.g., polyimide) between the conductive trace and the semiconducting substrate.

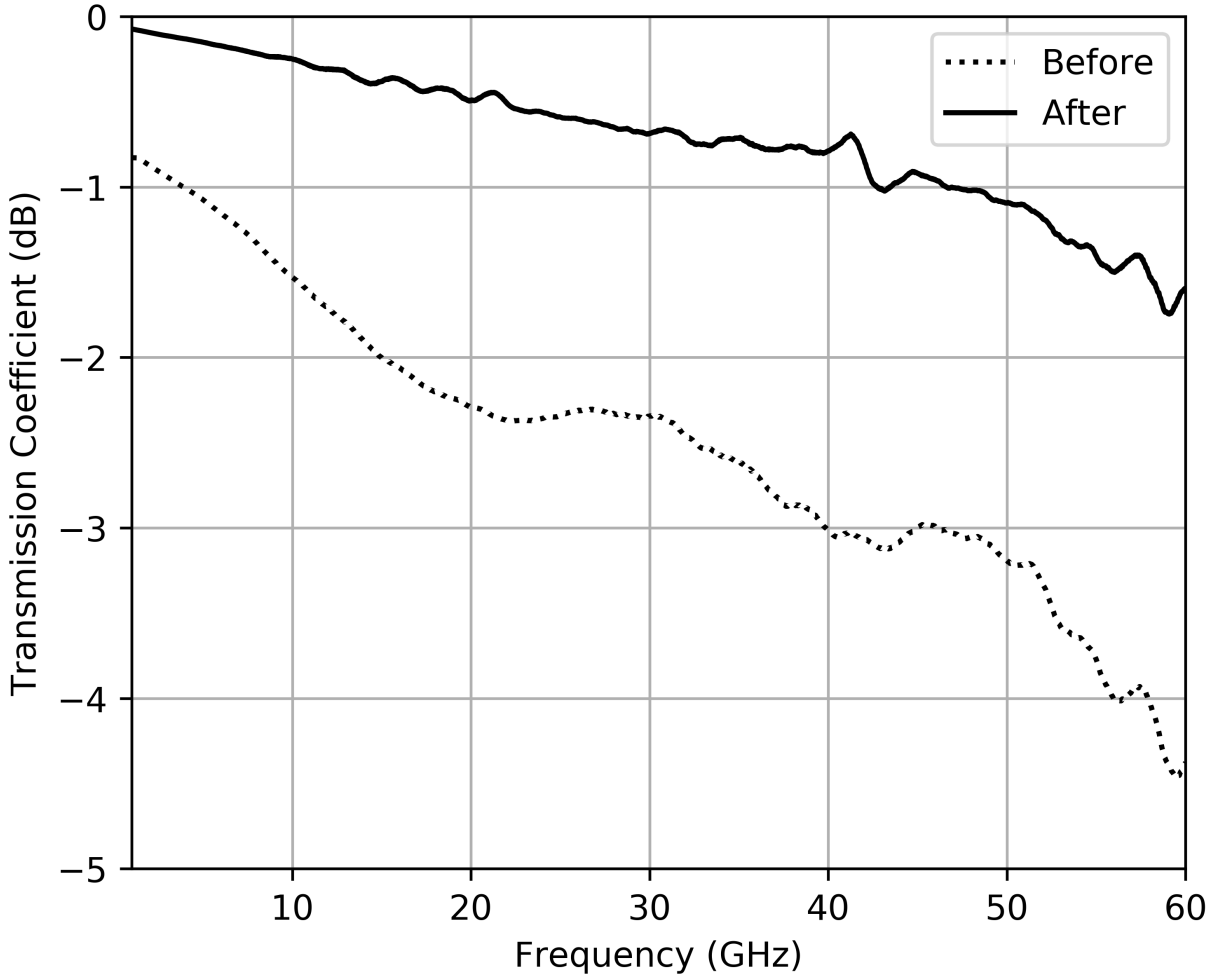

Figure 4.12: Measured transmission coefficient of 4.5 mm long transmission line printed over a trench, before and after printing additional silver.

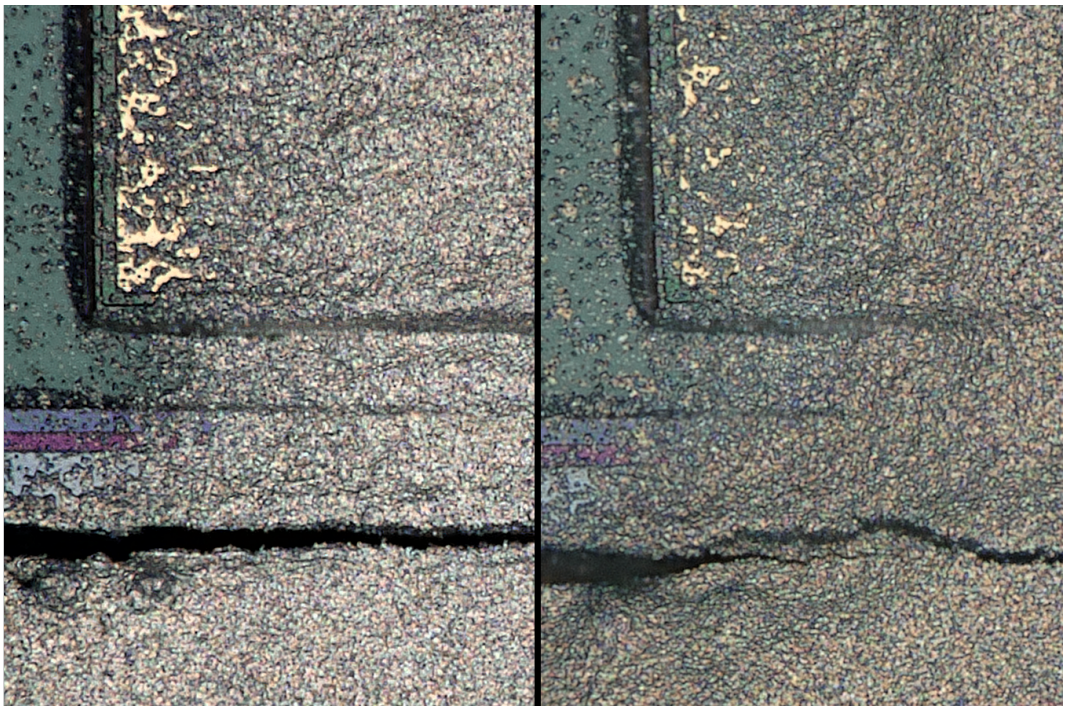

Figure 4.13: Image of die with cracking at Ag-GaAs interface before repair (left) and after repair (right).

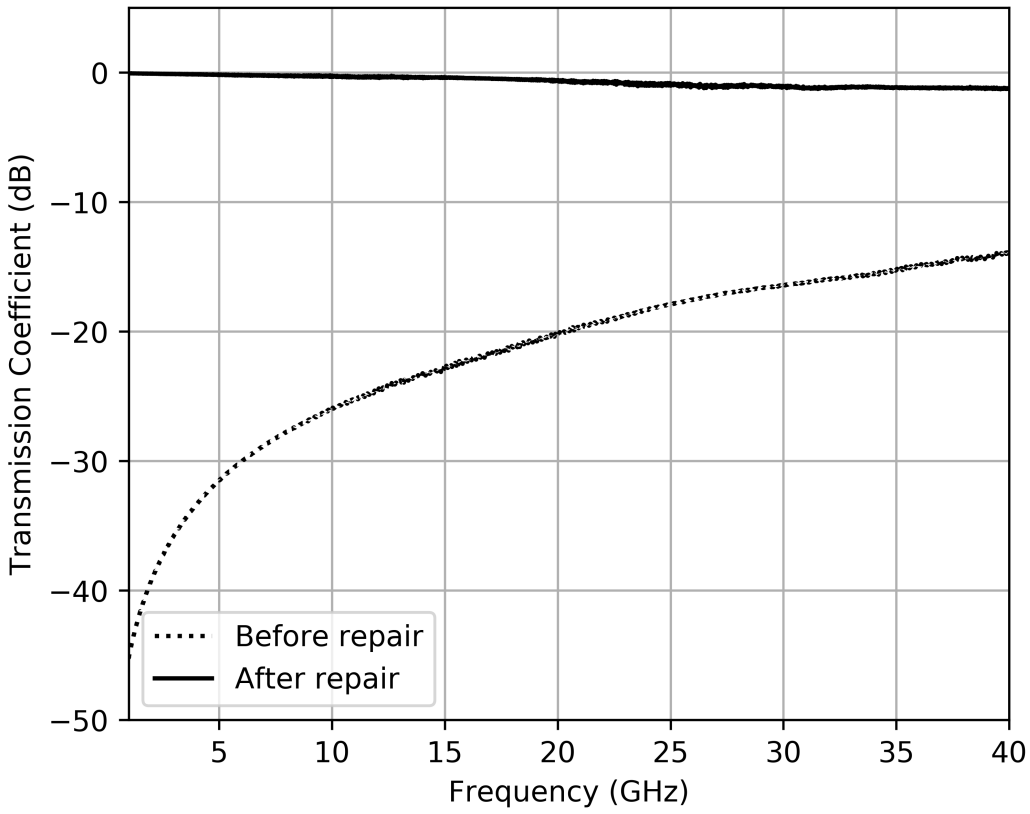

Figure 4.14: Measured transmission coefficient of attenuator circuit with cracked interface before and after repair.

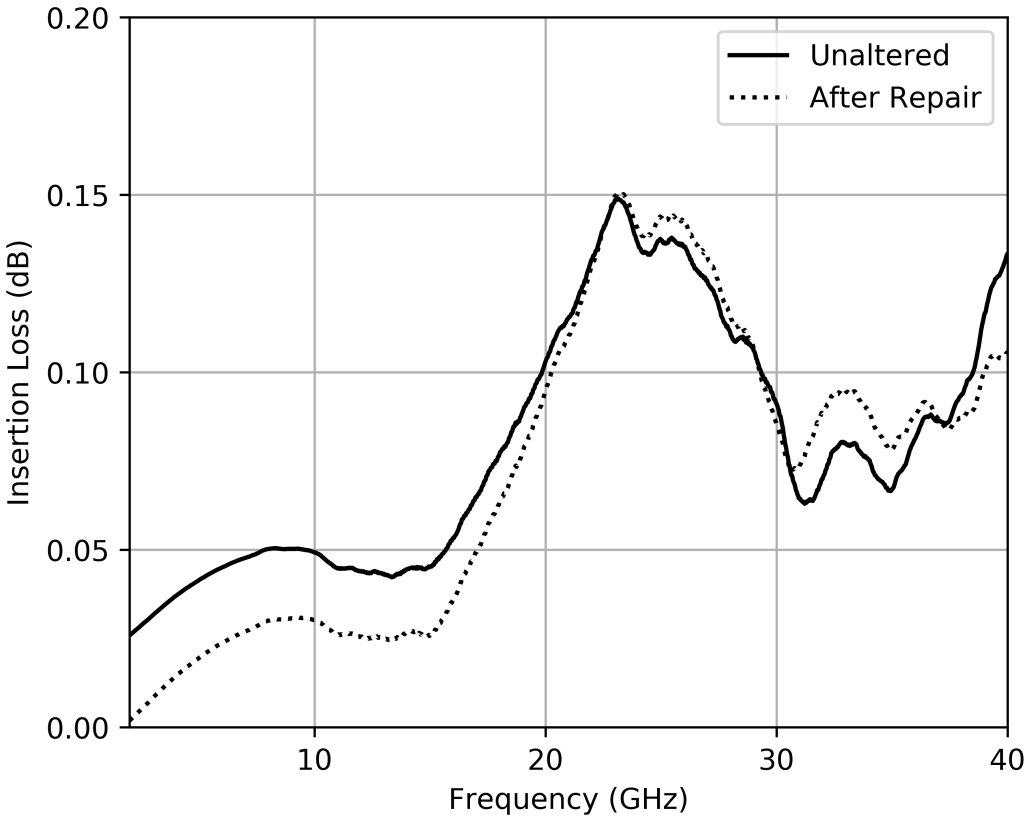

Figure 4.15: Measured insertion loss of interconnection to die after repair as calculated using equation 4.2, compared to one with no cracking.

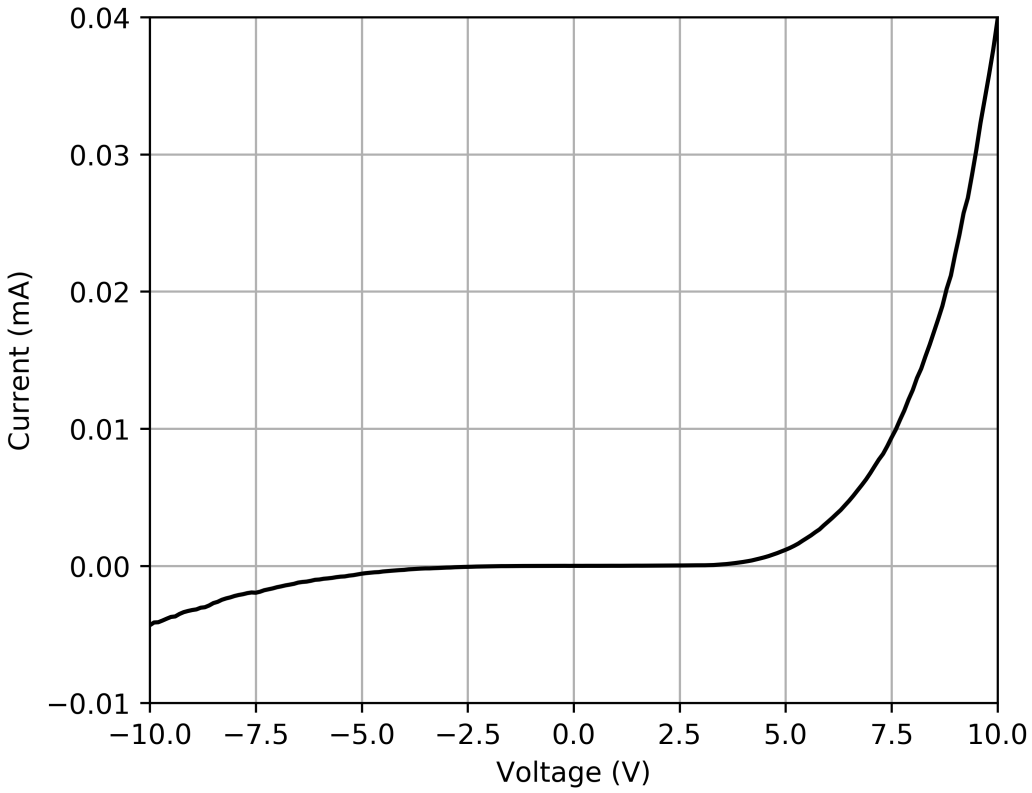

Figure 4.16: Measured I-V curve of Ag-GaAs interface on attenuator.

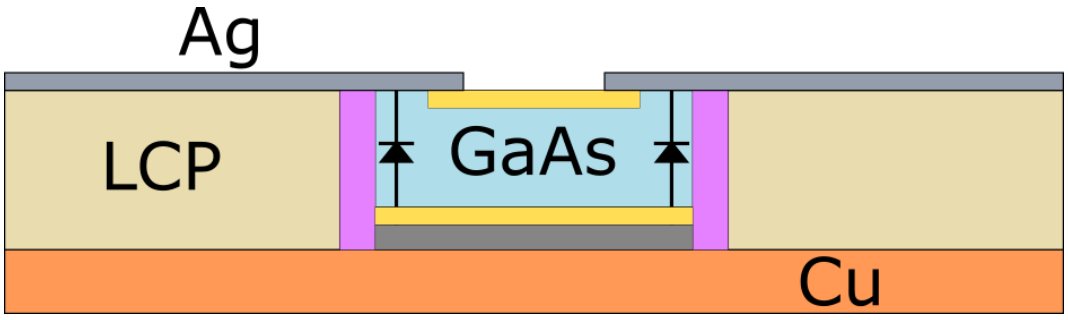

Figure 4.17: Schematic representation of Ag-GaAs diode.

CHAPTER 5

ADDITIVELY MANUFACTURED SELF-PACKAGED KU-BAND TRANSMITTER

5.1 Introduction

In this chapter, we address a key problem facing increased demand for wireless electronic systems. This demand ranges from applications such as automotive radar systems and vehicle-to-everything (V2X) communications, to consumer electronics, military and space-based platforms. As the operating frequencies of these systems continues to increase, from microwave to mm-wave and beyond, losses associated with electronics packaging, as well as long interconnection distances between active components and their associated antennas, introduces a bottleneck in system performance. By integrating transmit and receive (T/R) electronics with their respective antenna, these losses can be minimized, improving system efficiency and performance, while achieving a small overall size and reduced weight. By employing additive manufacturing processes, high levels of integration can be achieved while minimizing system losses associated with packaging, reducing production time and costs, as well as allowing for greater flexibility in component selection.

Many electronics packaging techniques have been developed which provide varying degrees of integration and functional density, such as System-on-Chip (SoC), System-on-Package (SoP) and System-in-Package (SiP). SoC provides a high level of system integration, incorporating analog, digital and RF electronics on a single die [110]. By including antennas on the same die, the shortest possible distance between the T/R electronics and the radiating element can be achieved [111]. However, below mm-Wave frequencies, the area required for such an antenna can make this approach cost-prohibitive. Performance of on-chip antennas can also be greatly degraded due to the substrates on which they are fabricated [112]. While SoC designs provide a high level of integration, their components are fixed at the design

stage, increasing development cost and time.

SiP and SoP technologies provide a lower cost alternative to SoC development while providing high functional density. By leveraging existing integrated circuits, non-recurring engineering costs are reduced, as well as the time required for development and testing. Through both SiP and SoP processes offer a reduction in size, at mm-wave frequencies and beyond, the chip-to-chip and chip-to-board interconnections traditionally fabricated by bond-wires presents a significant limitation to system performance. Connections between active circuits and their respective antennas may require expensive connectors and cables, increasing system complexity, cost and weight, while contributing additional losses to transmitted and received signals.

This chapter demonstrates a compact system-on-antenna utilizing a light-weight, low cost antenna with integrated transmit electronics operating in the Ku frequency band. By employing a hybrid additive and subtractive fabrication process, COTS substrate materials with good RF performance can be combined with aerosol jet printed interconnections, ensuring desired system performance, as well as providing the smallest footprint possible compared to traditionally packaged components. Combining a rigid 3D printed antenna with a flexible substrate, as demonstrated in [113, 114], the active devices can be readily integrated within the volume of the antenna, providing the shortest possible interconnection between the transmit electronics and the antenna feed location. By eliminating the need for additional RF connectors and cables, the mass of the transmitter can be minimized, while maximizing efficiency by eliminating cable and connector insertion losses.

5.2 Design and Fabrication

Design and fabrication of the antenna and active electronics can be performed in parallel. A Vivaldi antenna is designed and measured to ensure proper radiator performance over the required frequency band. The active electronics are designed to achieve desired system performance, and arranged to fit within a cavity formed inside the legs of the antenna. The

active electronics are then assembled and combined with the antenna to form a completed system. The substrate of choice for this work is Panasonic Felios RF705T liquid crystal polymer (LCP), due to its excellent RF characteristics over the frequency range considered, as well as its compatibility with a variety of fabrication techniques.

The circuit demonstrated in this work combines a commercially available voltage controlled oscillator (VCO) with a medium power amplifier. The VCO used is a United Monolithic Semiconductors CHV2270, offering a tunable output frequency of approximately 12 GHz to 13.5 GHz. Measured output power of this device varies over the tunable frequency range, from approximately -1 dBm around 12.1 GHz, to nearly 4 dBm at 13.5 GHz. This output is passed through an Analog Devices HMC451 medium power amplifier, providing approximately 20 dB of gain, with a measured saturated output power of approximate 21 dBm. A 0 dB attenuator, Mini-Circuits KAT-0-DG+, is placed before the RF input to the amplifier, providing flexibility for designs requiring attenuation of the RF signal before amplification without the need for additional alterations to the substrate. A schematic representation of this circuit can be seen in the top of Figure 5.6.

Fabrication of the antenna begins by printing the body and covers of the antenna on an Objet Connex350 polyjet printer. After removal of support material and cleaning, a 60 nm thick layer of titanium metal is deposited on the surface of the antenna to aid in the adhesion of subsequent metal layers. A 500 nm thick layer of copper metal is then sputter deposited over the titanium layer, providing a seed layer for plating. An additional 6 µm of copper metal is electroplated on top of the seed layer, providing a final metal thickness of approximately 6.5 µm.

The active circuits are fabricated on a 100 µm thick LCP substrate, providing a substrate surface level with the surfaces of both the VCO and amplifier. This material is prepared by removing existing copper cladding material from a 75 µm thick sheet of LCP material. This is then laminated to a 0.5 mm thick copper shim with a 25 µm thick bonding sheet, Panasonic R-BM17, providing a dielectric thickness of approximately 100 µm. The copper

shim serves as an RF and DC ground plane, as well as providing a degree of heatsinking for the active components. Pockets are then etched from this laminated LCP stack with the use of a laser cutter utilizing a 40 watt CO_2 laser. After etching of the pockets for the active devices, the substrate is cleaned in a KOH solution described in Chapter 4.

After substrate preparation, active devices are placed within their respective cavities. Active components, as well as bypass capacitors, are attached to the exposed copper ground plane with Epo-Tek H20E silver epoxy and cured at 150 °C for 1 hour. The remaining areas within each pocket are then filled with an ultraviolet light curable, high temperature epoxy, Formlabs High Temp resin. This epoxy is deposited by syringe and allowed to cure under UV light exposure for 5 hours.

As was shown in chapter 4, a Schottky diode was unintentionally formed when silver metal was deposited over the exposed semiconductor material of an IC. This diode may introduce additional harmonic content in a transmitted or received signal, as well as potentially drawing additional power, reducing system efficiency. By depositing an additional dielectric material over the exposed semiconductor, this effect can be minimized or eliminated.

A poly(methyl methacrylate) (PMMA) ink has been created to provide an insulating layer between each bare die IC used and the silver nanoparticle ink to be printed. This ink is prepared by combining 45 w.t.% dimethyl sulfoxide (DMSO) and 45 w.t.% toluene, into which 10 w.t.% PMMA powder is added. This solution is heated to approximately 65 °C and stirred for 6 hours until all solid material has dissolved. This ink is then aerosol jet printed using a pneumatic atomization process. A nozzle with a 300 µm diameter is used, with an atomizer gas flow rate of 555 SCCM, exhaust gas flow rate of 525 SCCM, and sheath gas flow rate of 80 SCCM, with a print stage velocity of 1 mm/s, yielding lines approximately 50 µm wide and 4 µm thick. During printing, the printer stage is heated to approximately 60 °C to remove some of the solvent, allowing multiple layers to be printed without significant deformation to previously deposited layers. After printing, each piece is dried on a hotplate at 120 °C for 30 minutes to completely remove any remaining solvent.

One advantage to using a thermoplastic polymer as a printed dielectric layer is that it can be melted to form a smooth surface. After initial printing of the PMMA ink, the ink surface exhibits significant roughness due to the printing process. After printing, this PMMA layer can be melted at a temperature greater than the melting temperature of the PMMA, and below the melting temperature of the LCP substrate. After drying of the PMMA material is complete, it is subsequently placed under vacuum at 180 °C for 12 hours. This vacuum environment removes any additional gas which may be held within the printed layer, as well as allowing the material to melt and self-level. Figure 5.1 shows a surface profile of a section of printed PMMA, before and after this final thermal leveling process.

By printing PMMA around each device, transitions from the die surface to the surrounding epoxy material can be improved, removing sharp features present from possible under-filling of the pocket surrounding each device. Figure 5.2 shows the transition from the surface of a 0 dB attenuator to the surrounding epoxy material, before and after deposition of a PMMA layer. As is shown, the PMMA layer remains thin, while providing a smooth transition from the exposed bonding pad, to the die surface, and finally to the surrounding pocket.

After printing and thermally treating the PMMA layer, silver metal is deposited to form transmission lines, device interconnections, and DC biasing lines. The silver ink used here is diluted Clariant Prelect TPS 50 G2, and aerosolized using an ultrasonic atomization process. The ink is printed using a print nozzle diameter of 150 µm, an atomizer carrier gas flow rate of 23 SCCM, and sheath gas flow rate of 50 SCCM, resulting in lines approximately 2 µm thick and 20 µm wide. Three layers of silver metal are printed to achieve a final metal layer thickness of 6 µm, and cured at 180 °C for 3 hours. Figure 5.3 shows the final cross-sectional stackup of the active components. Figure 5.4 shows an optical image of an interconnection formed by printed silver over printed PMMA to the input of a 0 dB attenuator.

With printing of the PMMA and silver metal layers complete, a 4 conductor ribbon cable connector is attached using the same die attach epoxy and curing schedule. This ribbon

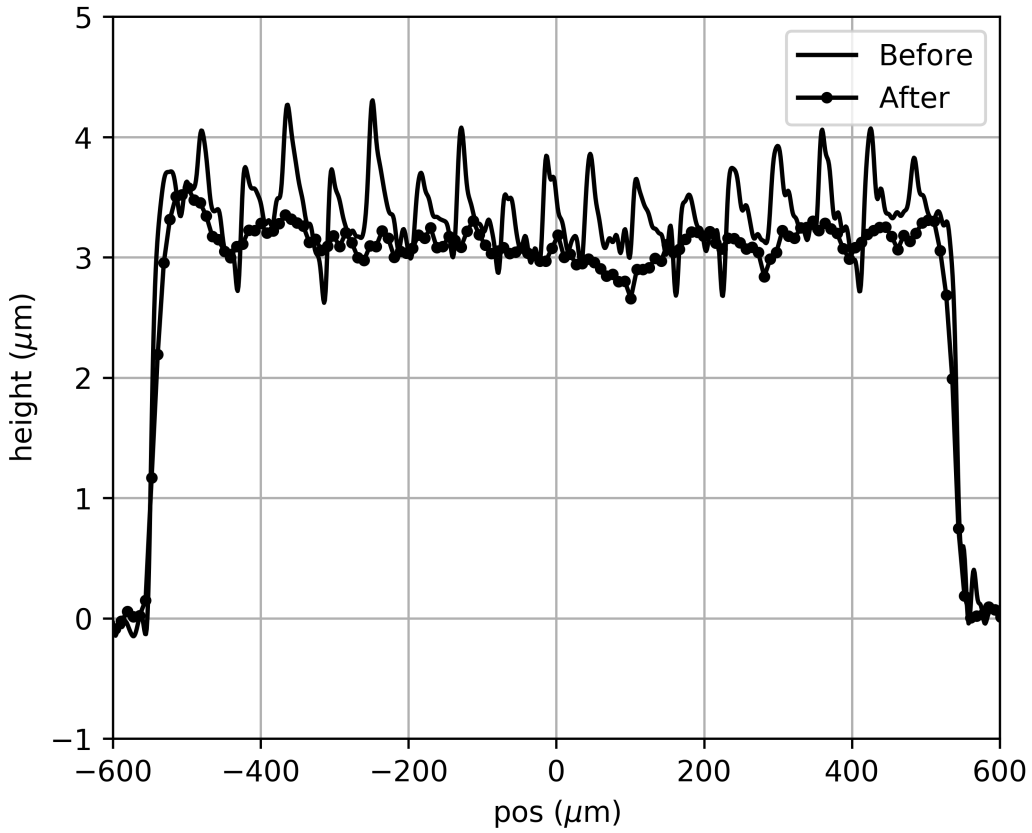

Figure 5.1: Surface profile plot of PMMA before and after thermal leveling.

cable provides DC power for the VCO and amplifier. The final assembled active components are mounted within the leg of the Vivaldi antenna. The copper sheet is attached to the antenna leg with MG Chemicals 8331 silver epoxy, and thermally cured at 65 °C for 3 hours. The antenna feed line is attached to a recess in the opposing leg using the same silver epoxy. The assembled antenna can be seen in Figure 5.6. Figure 5.5 summarizes the complete fabrication process.

5.3 Measurement

The received power spectrum was measured using an HP 8562A spectrum analyzer connected to a Cobham Sensor Systems H-1498 horn antenna by a 2 meter long coaxial cable. This antenna has a measured gain of 10.4 dBi at 13 GHz. Cable losses have been measured at 2.2 dB over the 2 meter length at 13 GHz. The transmitting antenna is placed at a

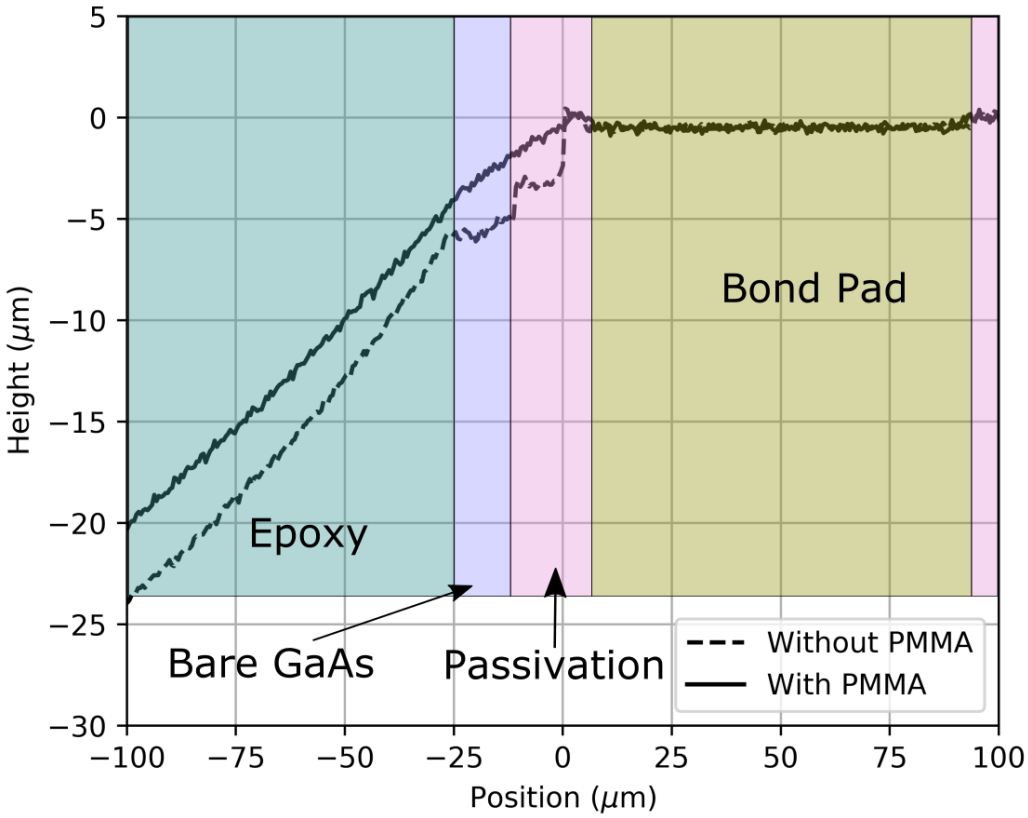

Figure 5.2: Surface profile plot of a transition from an attenuator to the surrounding epoxy resin, before and after PMMA deposition.

distance of 2 meters from the receiving antenna. Expected received power P_r is calculated from [84] as:

$$P_r = P_t - L_t + G_t - L_0 + G_r - L_r \ (dBm) \tag{5.1}$$

where P_t is the transmit power, L_t is the feed line loss, G_t is the transmitter antenna gain, L_0 is the free space path loss, G_r is the receiver antenna gain, and L_r is the loss in the receiver cable. Transmitter feed line loss L_t is approximately 0.2 dB, transmitter gain G_t at 12 GHz has been measured to be 8.9 dBi. Free space path loss is calculated from [84] as:

$$L_0 = 20log(\frac{4\pi d}{\lambda}) \tag{5.2}$$

where d is the distance from the transmitter to the receiver, and λ is the wavelength in free

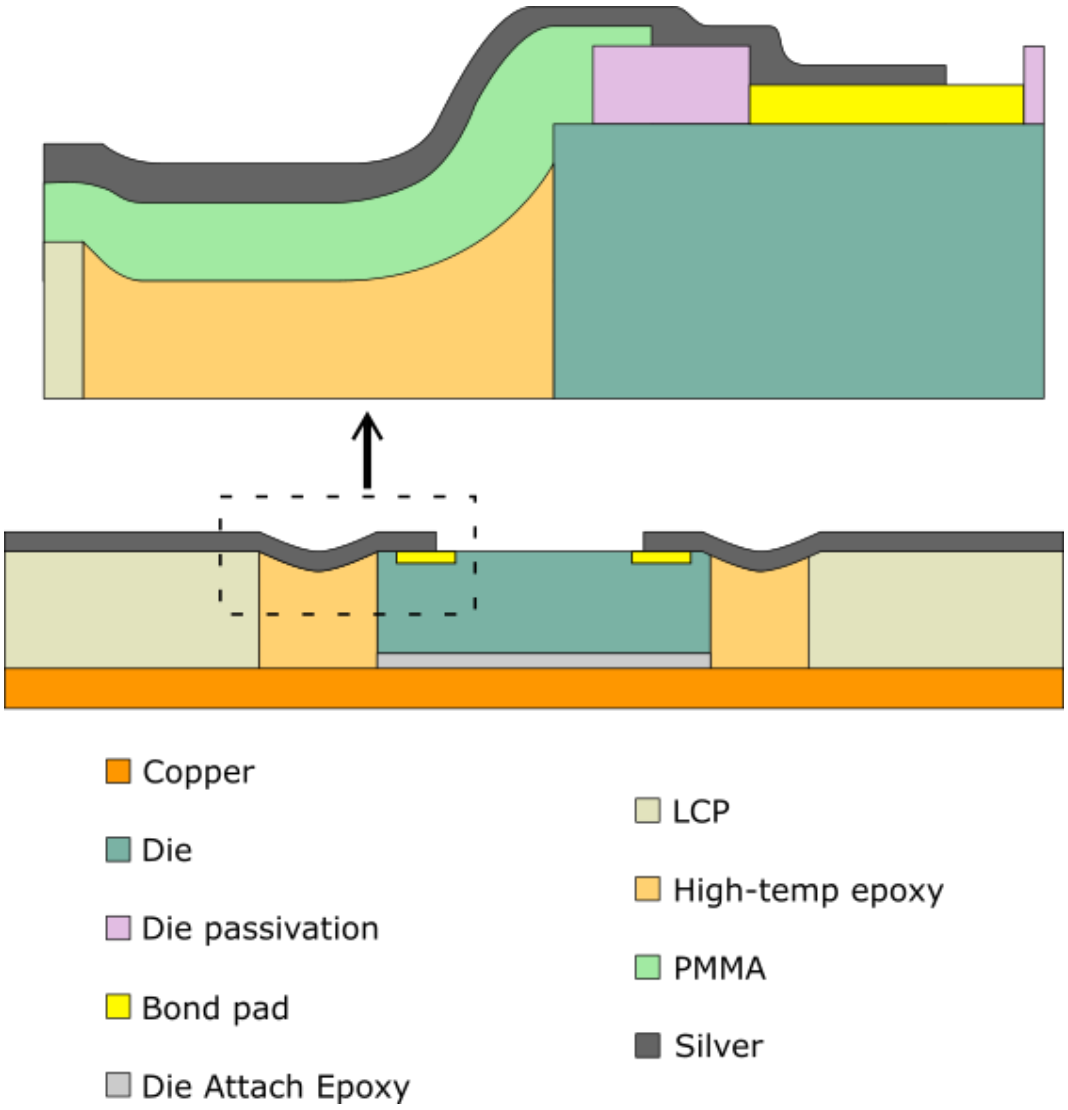

Figure 5.3: Stackup of completed active circuit.

space. At a distance of 2 meters, L_0 is approximately 60 dB. With a transmit power level P_t of 18.4 dBm, this corresponds to an expected received power level of -24.9 dBm. Received power, shown in Figure 5.7, is approximately -34 dBm, 10.6 dB less than that predicted by Equation 5.1. Figure 5.8 shows the expected received power spectrum. The spectrum shown in this picture has been measured from the output of the medium power amplifier, and scaled by Equation 5.1. This reduction in received power is currently being investigated, however it is most likely due to a poor electrical connection between the 0.5 mm copper sheet on which the active devices are mounted, and the copper metal of the antenna, resulting in a

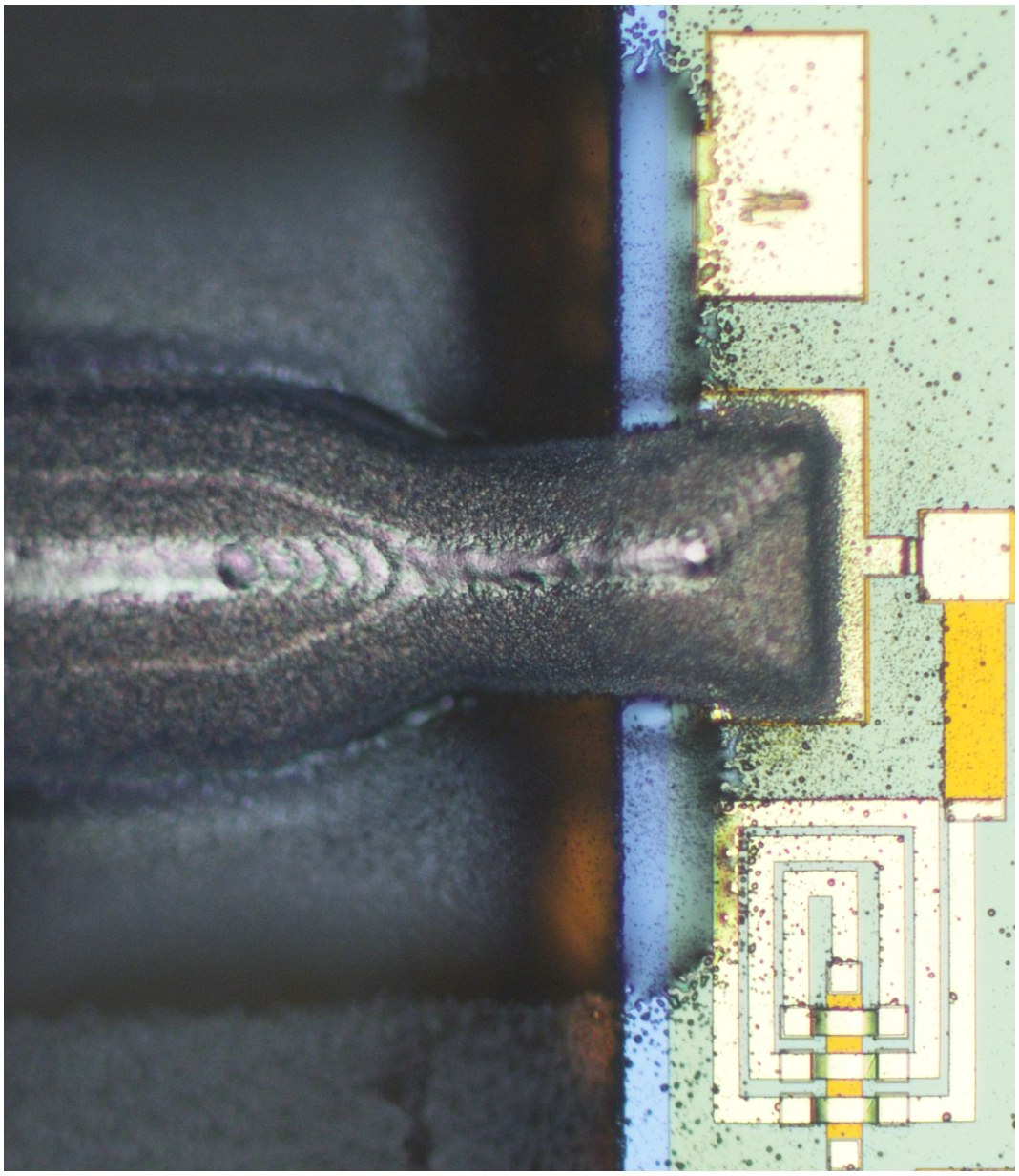

Figure 5.4: Aerosol jet printed interconnection, silver over PMMA to amplifier RF output.

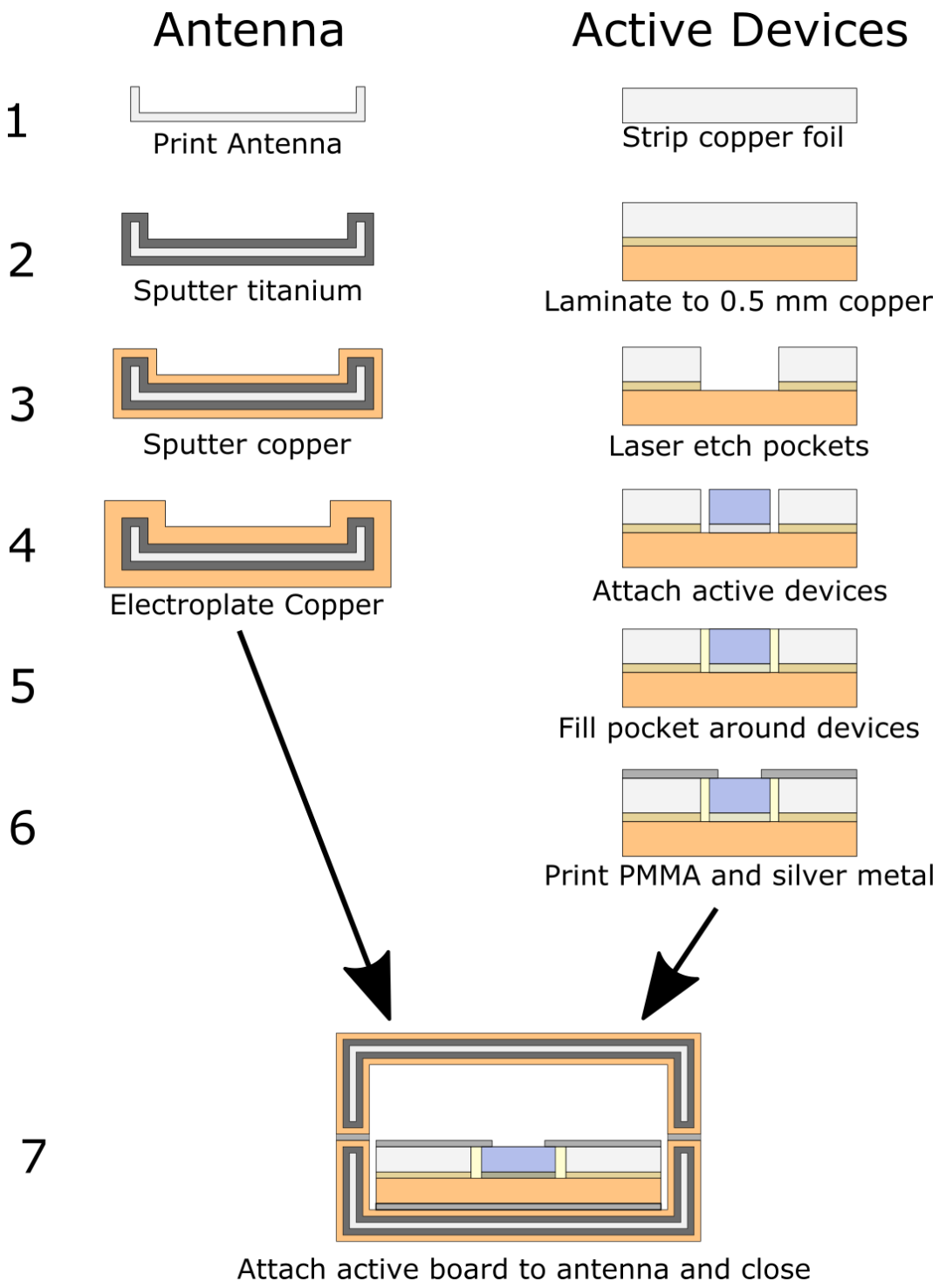

Figure 5.5: Fabrication process for the printed antenna and active circuit components.

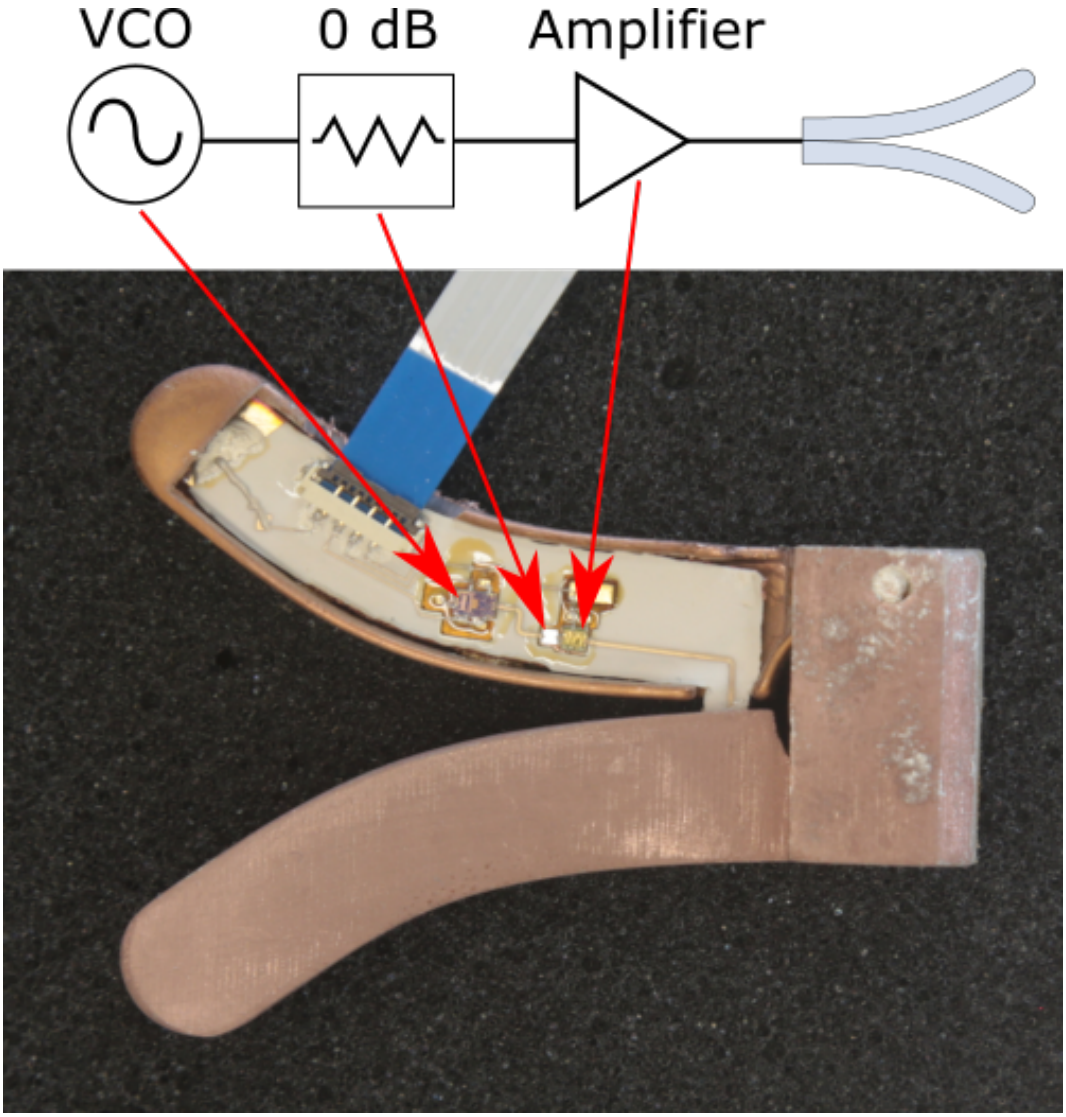

Figure 5.6: Top: schematic representation of the active circuit. Bottom: assembled antenna with integrated active electronics.

high inductance in the RF ground connection. Antenna modifications are currently being developed to improve the assembly process. Measurement results are pending, and will be published upon completion.

5.4 Summary

This chapter demonstrates a compact system-on-antenna capable of operating in the Ku band. By utilizing additive manufacturing techniques, active electronic components can be

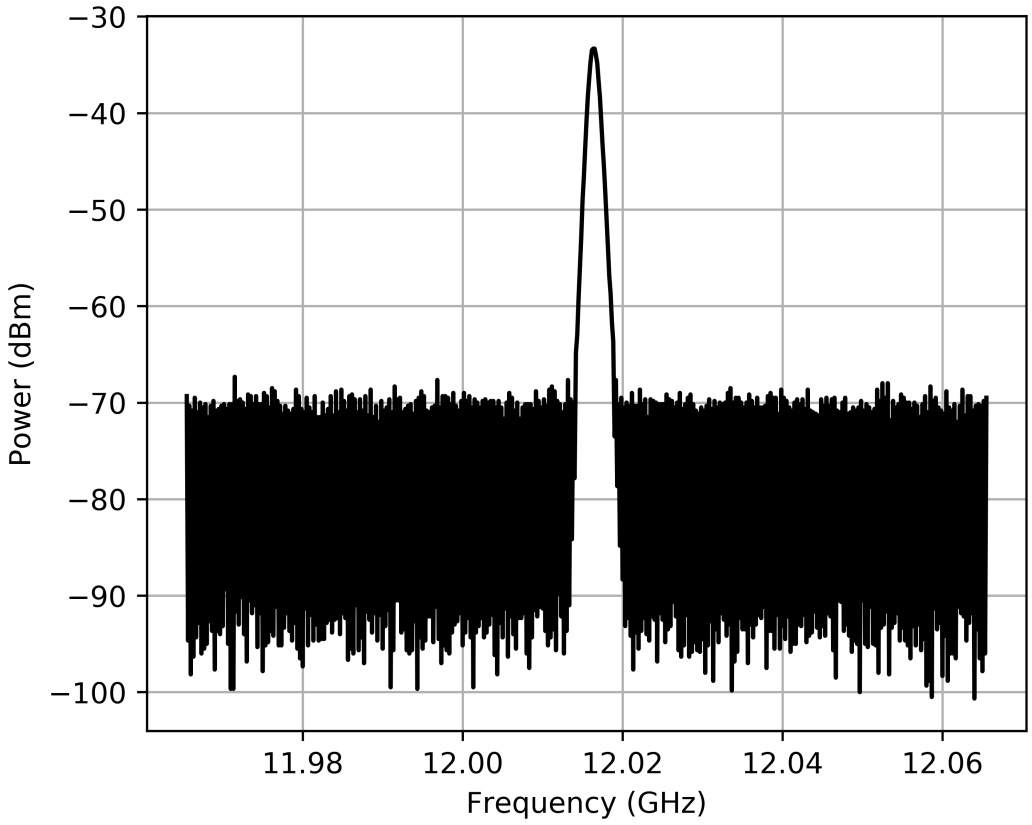

Figure 5.7: Received power spectrum.

easily integrated with antennas, providing a high degree of functionality with a minimum system footprint. Elimination of expensive and heavy connectors, as well as bonding wires typically associated with packaged electronics allows for low-loss operation well into the mm-wave frequency range, enabling a wide range of systems to be developed at low cost with short development times.

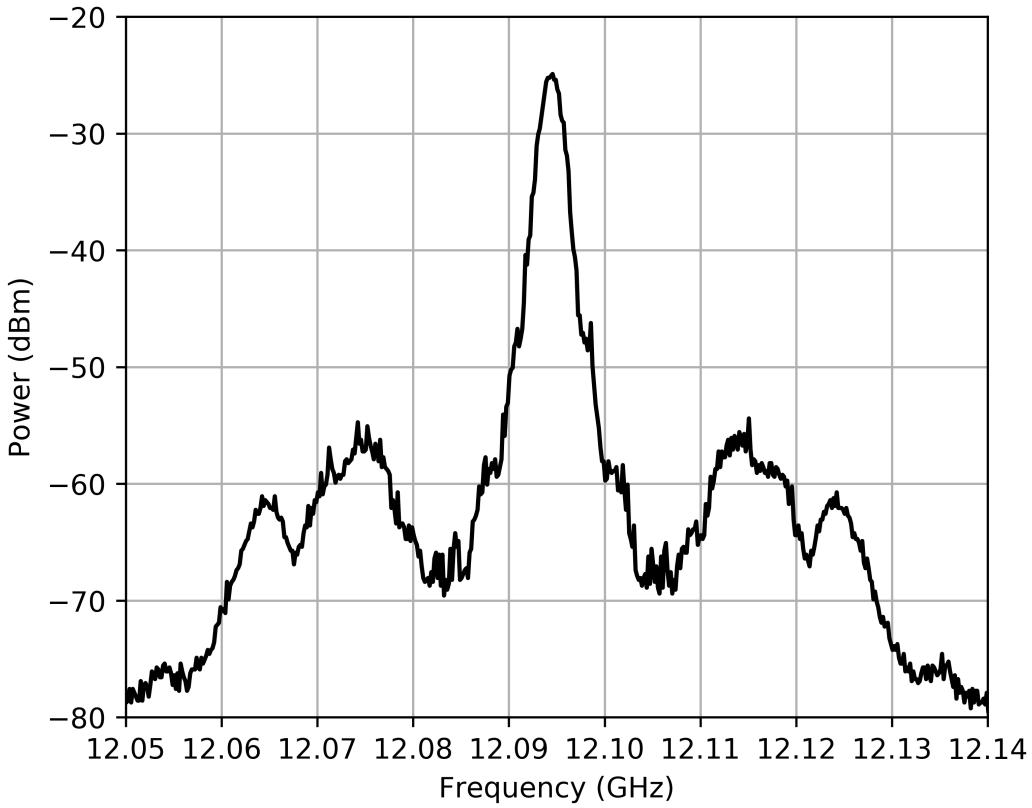

Figure 5.8: Anticipated received power spectrum, as measured from output of active devices, scaled by Equation 5.1.

CHAPTER 6

CONCLUSIONS

6.1 Conclusions

In this dissertation, a number of processes have been developed combining additive and subtractive manufacturing techniques to package RF electronics capable of operating into the mm-wave frequency range and beyond. By leveraging AM practices, fabrication time and cost can be reduced, while simultaneously eliminating the need for highly specialized equipment and facilities normally used to fabricate and package high frequency circuits and systems.

In chapter 2, aerosol jet printing was demonstrated as a viable alternative to traditional lithographic processes for fabrication of passive circuit elements capable of operating beyond 200 GHz. Polarizing screens, consisting of long parallel lines with narrow line widths and separations were demonstrated, taking advantage of the fine feature sizes which can be achieved with the aerosol jet printing process. The combination of printing a thin seed layer, onto which additional metal can be plated with an electroless plating solution was shown, reducing printing time and cost.

In chapter 3, aerosol jet printed circuits were combined with packaged components to form a functional high frequency oscillator circuit. Distributed circuit elements were designed, simulated and fabricated, forming the building blocks necessary for the complete circuit. By leveraging the long stand-off distance of the print nozzle from the substrate surface, complete metallization of the circuit, including vias connecting the top metal layer to the underlying ground plane, were demonstrated, as well as limitations due to via wall quality as a result of mechanical drilling operations. By combining aerosol jet printing with commercially available components, circuit designs can be rapidly iterated, reducing time between initial system concept and demonstration of a functional prototype.

Chapter 4 demonstrated a hybrid additive and subtractive process for packaging of bare die integrated circuits. By utilizing commercially available substrates, materials can be chosen with low-loss characteristics over the required frequency range, greatly improving system performance over the more lossy materials currently capable of being printed. Replacing bonding wires with printed interconnections provides much greater flexibility and control of the interconnection characteristics, allowing for low loss operation beyond 60 GHz, paving the way for system-level integration of circuits operating beyond mm-wave frequencies.

In chapter 5, multiple AM techniques were combined to package electronics operating from 12 GHz to 13.5 GHz. Using a polyjet printing process, a low cost, low-weight Vivaldi antenna can be readily combined with active electronics, using the antenna body as the system package. Printing additional polymer material, additional parasitic effects of printed interconnections can be reduced or eliminated, while providing a high quality transition from each die to its surrounding dielectric.

This work demonstrates the advantages of using additive manufacturing for RF circuit prototyping and device packaging. Combined with subtractive processes, commercially available materials and components can be brought together to create a functional system rapidly, without the need for complex machinery, sterile environments or highly skilled technicians.

6.2 Technical Limitations of Additive Manufacturing

Material compatibility poses a significant challenge for packaging electronic components. Many metal nanoparticle inks require thermal sintering at temperatures incompatible with most printable polymers. Additionally, different coefficients of thermal expansion can easily result in failures of interconnections, or complete assemblies. By tailoring materials to achieve desirable properties, these unwanted effects can potentially be minimized, greatly increasing the range of applications possible with additive manufacturing techniques.

Printed materials are subject to environmental stresses. When left untreated, printed silver metal oxidizes over time, degrading system performance. Traditional methods, such

as gold plating of conductors, have proven to be effective in mitigation of these factors. However, these processes require additional personnel skilled in safe and accurate operation of the systems necessary to carry out these tasks. By taking advantage of existing AM processes, encapsulation of printed metals using thin dielectric materials may present one method to combat these limitations.

The low conductivity of most printed metals can present a limitation to high power applications. Resistive losses encountered in these metals can lead to significant self-heating of the printed metal traces, ultimately resulting in destruction of the substrate onto which it has been printed. Self-heating of printed metals may also speed degradation due to interaction with atmospheric conditions. Dielectric and encapsulation materials must be compatible with the temperatures that will be encountered during normal operating conditions.

6.3 Future Work

Additive manufacturing techniques can be combined to achieve a wide range of goals. Taking advantage of metal and ceramic printing processes, a wide range of structures can be fabricated capable of withstanding high temperatures experienced with high power electronics. Combined with inkjet and aerosol jet printing, high power, high frequency circuits can be realized without the need for additional exotic materials and processes.

With the growing variety of printable polymer materials, low-loss substrate materials can be deposited with both inkjet and aerosol jet technologies, providing an additional avenue for fabrication of low-loss circuits operating well into the mm-wave frequency range. Using these materials, a chip-first packaging process can be developed using AM processes, reducing the cost and time necessary to fabricate systems operating at these high frequencies. By combining materials, functional substrates can be fabricated, incorporating filters, capacitors, resistors, inductors, as well as microfluidic channels for thermal cooling.

AM processes can be used to package both individual components, as well as complete systems. Chip-scale and wafer-level packaging processes can be replaced or augmented by

leveraging AM techniques, printing multi-layered fan-out circuitry directly to the bonding pads of a device, reducing the number of intermediate connections between devices and enabling an increase in functional density.

The fine print resolution of inkjet and aerosol jet printing can be combined with existing packaged components to fabricate complete systems rapidly and at low cost. Many digital and mixed-signal integrated circuits have a large number of connections, with fine pitch between each signal pad, typically requiring a multi-layer circuit board fabrication process to fan out these connections, potentially increasing development cost when these high density connections are localized to a few individual devices. By depositing metal and dielectric materials, these high density connections can be fanned out locally, reducing fabrication costs. When combined with RF integrated circuits, complete systems can be designed, fabricated and deployed quickly and inexpensively.

BIBLIOGRAPHY

BIBLIOGRAPHY

[1] C. Kim, D. Espalin, M. Liang, H. Xin, A. Cuaron, I. Varela, E. Macdonald, and R. B. Wicker. 3D Printed Electronics With High Performance, Multi-Layered Electrical Interconnect. *IEEE Access*, 5:25286–25294, 2017.

[2] K. Y. Park, M. I. M. Ghazali, N. Wiwatcharagoses, and P. Chahal. Thick 3D Printed RF Components: Transmission Lines and Bandpass Filters. In *2018 IEEE 68th Electronic Components and Technology Conference (ECTC)*, pages 2186–2191, May 2018.

[3] J. A. Paulsen, M. Renn, K. Christenson, and R. Plourde. Printing conformal electronics on 3D structures with Aerosol Jet technology. In *2012 Future of Instrumentation International Workshop (FIIW) Proceedings*, pages 1–4. IEEE, Oct 2012.

[4] K. Lomakin, M. Sippel, G. Gold, J. Ringel, D. Weiß, K. Helmreich, M. Ankenbrand, and J. Franke. Substituting bond wires by additively manufactured interconnections. In *2018 11th German Microwave Conference (GeMiC)*, pages 367–370, March 2018.

[5] J. S. Kilby. Miniaturized electronic circuits, February 06 1959. US Patent 3,138,743.

[6] T. S. Horng, S. M. Wu, H. H. Huang, C. T. Chiu, and C. P. Hung. Modeling of lead-frame plastic CSPs for accurate prediction of their low-pass filter effects on RFICs. *IEEE Transactions on Microwave Theory and Techniques*, 49(9):1538–1545, Sep. 2001.

[7] J. Y. Kim, H. Y. Lee, J. H. Lee, and D. P. Chang. Wideband characterization of multiple bondwires for millimeter-wave applications. In *2000 Asia-Pacific Microwave Conference. Proceedings (Cat. No.00TH8522)*, pages 1265–1268, Dec 2000.

[8] C. C. Wei, C. T. Fan, T. H. Chiang, M. K. Chiu, and S. P. Ru. A comparison study of high-frequency performance between ball bonding and ribbon bonding. In *2009 4th International Microsystems, Packaging, Assembly and Circuits Technology Conference*, pages 685–688, Oct 2009.

[9] J. Wolf, H Reichl, O Ehrmann, K Buschick, FJ Schmuckle, W Heinrich, M Toepper, and A Owzar. System integration for high frequency applications. In *PROCEEDINGS-SPIE THE INTERNATIONAL SOCIETY FOR OPTICAL ENGINEERING*, pages 29–36. SPIE INTERNATIONAL SOCIETY FOR OPTICAL, 1997.

[10] W. Heinrich. The flip-chip approach for millimeter wave packaging. *IEEE Microwave magazine*, 6(3):36–45, 2005.

[11] S. Lee, S. Song, Y. Kim, J. Lee, C. Cheon, K. Seo, and Y. Kwon. A V-Band Beam-Steering Antenna on a Thin-Film Substrate With a Flip-Chip Interconnection. *IEEE Microwave and Wireless Components Letters*, 18(4):287–289, April 2008.

[12] J. H. Lau, M. Li, Q. M. Li, I. Xu, T. Chen, Z. Li, K. H. Tan, Q. X. Yong, Z. Cheng, K. S. Wee, R. Beica, C. T. Ko, S. P. Lim, N. Fan, E. Kuah, W. Kai, Y. Cheung, E. Ng, C. Xi, J. Ran, H. Yang, Y. H. Chen, N. C. Lee, M. Tao, J. Lo, and R. Lee. Design, Materials, Process, Fabrication, and Reliability of Fan-Out Wafer-Level Packaging. *IEEE Transactions on Components, Packaging and Manufacturing Technology*, 8(6):991–1002, June 2018.

[13] R. A. Fillion. A forecast on the future of hybrid wafer scale integration technology. *IEEE Transactions on Components, Hybrids, and Manufacturing Technology*, 16(7):615–625, Nov 1993.

[14] R. Hahn, A. Kamp, A. Ginolas, M. Schmidt, J. Wolf, V. Glaw, M. Topper, O. Ehrmann, and H. Reichl. High power multichip modules employing the planar embedding technique and microchannel water heat sinks. In *Thirteenth Annual IEEE. Semiconductor Thermal Measurement and Management Symposium*, pages 49–56, Jan 1997.

[15] B. Lee, V. Sundaram, B. Wiedenman, C. K. Yoon, V. Kripesh, M. Iyer, and R. R. Tummala. Chip-last Embedded Active for System-On-Package (SOP). In *2007 Proceedings 57th Electronic Components and Technology Conference*, pages 292–298, May 2007.

[16] V. Sridharan, A. Goyal, S. Sitaraman, N. Kumbhat, N. Sankaran, H. Chan, F. Liu, D. Dawn, V. Nair, T. Kamgaing, F. Juskey, V. Sundaram, and R. Tummala. Ultra-miniaturized WLAN RF receiver with chip-last GaAs embedded active. In *2011 IEEE 61st Electronic Components and Technology Conference (ECTC)*, pages 1371–1376, May 2011.

[17] R. Carrillo-Ramirez and R. W. Jackson. A highly integrated millimeter-wave active antenna array using BCB and silicon substrate. *IEEE Transactions on Microwave Theory and Techniques*, 52(6):1648–1653, June 2004.

[18] X. Yang, A. Kaur, and P. Chahal. Embedded diodes for microwave and millimeter wave circuits. In *2014 IEEE 64th Electronic Components and Technology Conference (ECTC)*, pages 2144–2150, May 2014.

[19] R. R. Tummala. Packaging: past, present and future. In *2005 6th International Conference on Electronic Packaging Technology*, pages 3–7, Aug 2005.

[20] T. Siebolt Tevelde and A. Schmitz. Semiconductor circuit having active devices embedded in flexible sheet, October 10 1968. US Patent 3,579,056.

[21] R. A. Fillion, R. J. Wojnarowski, T. B. Gorcyzca, E. J. Wildi, and H. S. Cole. Development of a plastic encapsulated multichip technology for high volume, low cost commercial electronics. *IEEE Transactions on Components, Packaging, and Manufacturing Technology: Part B*, 18(1):59–65, Feb 1995.

[22] M. Topper, T. Baumgartner, M. Klein, T. Fritzsch, J. Roeder, M. Lutz, M. von Suchodoletz, H. Oppermann, and H. Reichl. Low cost wafer-level 3-D integration without

TSV. In *2009 59th Electronic Components and Technology Conference*, pages 339–344, May 2009.

[23] T. Duda and L. V. Raghavan. 3D metal printing technology. *IFAC-PapersOnLine*, 49(29):103–110, 2016.

[24] J. Zuniga, D. Katsavelis, J. Peck, J. Stollberg, M. Petrykowski, A. Carson, and C. Fernandez. Cyborg beast: a low-cost 3d-printed prosthetic hand for children with upper-limb differences. *BMC research notes*, 8(1):10, 2015.

[25] A. V. Do, B. Khorsand, S. M. Geary, and A. K. Salem. 3D printing of scaffolds for tissue regeneration applications. *Advanced healthcare materials*, 4(12):1742–1762, 2015.

[26] J. Wang, A. Goyanes, S. Gaisford, and A. W. Basit. Stereolithographic (SLA) 3D printing of oral modified-release dosage forms. *International journal of pharmaceutics*, 503(1-2):207–212, 2016.

[27] T. M. Rankin, N. A. Giovinco, D. J. Cucher, G. Watts, B. Hurwitz, and D. G. Armstrong. Three-dimensional printing surgical instruments: are we there yet? *Journal of Surgical Research*, 189(2):193–197, 2014.

[28] A. Bertsch, S. Heimgartner, P. Cousseau, and P. Renaud. Static micromixers based on large-scale industrial mixer geometry. *Lab on a Chip*, 1(1):56–60, 2001.

[29] M. Kasparova, L. Grafova, P. Dvorak, T. Dostalova, A. Prochazka, H. Eliasova, J. Prusa, and S. Kakawand. Possibility of reconstruction of dental plaster cast from 3D digital study models. *Biomedical engineering online*, 12(1):49, 2013.

[30] A. T. Gaynor, N. A. Meisel, C. B. Williams, and J. K. Guest. Multiple-material topology optimization of compliant mechanisms created via PolyJet three-dimensional printing. *Journal of Manufacturing Science and Engineering*, 136(6):061015, 2014.

[31] S. Tibbits. 4D printing: multi-material shape change. *Architectural Design*, 84(1):116–121, 2014.

[32] J. A. Gonzalez, J. Mireles, Y. Lin, and R. B. Wicker. Characterization of ceramic components fabricated using binder jetting additive manufacturing technology. *Ceramics International*, 42(9):10559–10564, 2016.

[33] J. P. Kruth, X. Wang, T. Laoui, and L. Froyen. Lasers and materials in selective laser sintering. *Assembly Automation*, 2003.

[34] O. S. Kim. Rapid Prototyping of Electrically Small Spherical Wire Antennas. *IEEE Transactions on Antennas and Propagation*, 62(7):3839–3842, July 2014.

[35] C. R. Garcia, R. C. Rumpf, H. H. Tsang, and J. H. Barton. Effects of extreme surface roughness on 3D printed horn antenna. *Electronics letters*, 49(12):734–736, 2013.

[36] D. Espalin, D. W. Muse, E. MacDonald, and R. B. Wicker. 3D Printing multifunctionality: structures with electronics. *The International Journal of Advanced Manufacturing Technology*, 72(5-8):963–978, 2014.

[37] E. G. Geterud, P. Bergmark, and J. Yang. Lightweight waveguide and antenna components using plating on plastics. In *2013 7th European Conference on Antennas and Propagation (EuCAP)*, pages 1812–1815, April 2013.

[38] M. I. M. Ghazali, K. Y. Park, V. Gjokaj, A. Kaur, and P. Chahal. 3D printed metalized plastic waveguides for microwave components. In *International Symposium on Microelectronics*, volume 2017, pages 000078–000082. International Microelectronics Assembly and Packaging Society, 2017.

[39] M. I. M. Ghazali, E. Gutierrez, J. C. Myers, A. Kaur, B. Wright, and P. Chahal. Affordable 3D printed microwave antennas. In *2015 IEEE 65th Electronic Components and Technology Conference (ECTC)*, pages 240–246, May 2015.

[40] J. A. Byford, M. I. M. Ghazali, S. Karuppuswami, B. L. Wright, and P. Chahal. Demonstration of RF and Microwave Passive Circuits Through 3-D Printing and Selective Metalization. *IEEE Transactions on Components, Packaging and Manufacturing Technology*, 7(3):463–471, March 2017.

[41] J Ebert, E Özkol, A Zeichner, K Uibel, Ö Weiss, U Koops, R Telle, and H Fischer. Direct inkjet printing of dental prostheses made of zirconia. *Journal of dental research*, 88(7):673–676, 2009.

[42] H Sirringhaus, T Kawase, RH Friend, T Shimoda, M Inbasekaran, W Wu, and EP Woo. High-resolution inkjet printing of all-polymer transistor circuits. *Science*, 290(5499):2123–2126, 2000.

[43] D. Redinger, S. Molesa, Shong Yin, R. Farschi, and V. Subramanian. An ink-jet-deposited passive component process for RFID. *IEEE Transactions on Electron Devices*, 51(12):1978–1983, Dec 2004.

[44] B. S. Cook, J. R. Cooper, and M. M. Tentzeris. Multi-Layer RF Capacitors on Flexible Substrates Utilizing Inkjet Printed Dielectric Polymers. *IEEE Microwave and Wireless Components Letters*, 23(7):353–355, July 2013.

[45] G. McKerricher, D. Titterington, and A. Shamim. A Fully Inkjet-Printed 3-D Honeycomb-Inspired Patch Antenna. *IEEE Antennas and Wireless Propagation Letters*, 15:544–547, 2016.

[46] H. Kao, C. Cho, and L. Chang. Inkjet-Printed Interdigital Coupled Line Filter on Liquid Crystal Polymer Substrate. *IEEE Electron Device Letters*, 34(12):1584–1586, Dec 2013.

[47] B. S. Y. Ung, B. Weng, R. Shepherd, D. Abbott, and C. Fumeaux. Inkjet printed conductive polymer-based beam-splitters for terahertz applications. *Opt. Mater. Express*, 3(9):1242–1249, Sep 2013.

[48] M. Walther, A. Ortner, H. Meier, U. Löffelmann, P. J. Smith, and J. G. Korvink. Terahertz metamaterials fabricated by inkjet printing. *Applied Physics Letters*, 95(25):251107, 2009.

[49] F. Cai, Y. H. Chang, K. Wang, W. T. Khan, S. Pavlidis, and J. Papapolymerou. High resolution aerosol jet printing of D-band printed transmission lines on flexible LCP substrate. In *2014 IEEE MTT-S International Microwave Symposium (IMS2014)*, pages 1–3. IEEE, 2014.

[50] M. T. Craton, J. Sorocki, I. Piekarz, S. Gruszczynski, K. Wincza, and J. Papapolymerou. Realization of Fully 3D Printed W-Band Bandpass Filters Using Aerosol Jet Printing Technology. In *2018 48th European Microwave Conference (EuMC)*, pages 1013–1016, Sep. 2018.

[51] Y. He, C. Oakley, P. Chahal, J. Albrecht, and J. Papapolymerou. Aerosol Jet printed 24 GHz end-fire quasi-Yagi-Uda antenna on a 3-D printed cavity substrate. In *2017 International Workshop on Antenna Technology: Small Antennas, Innovative Structures, and Applications (iWAT)*, pages 179–182, March 2017.

[52] A. A. Gupta, A. Bolduc, S. G. Cloutier, and R. Izquierdo. Aerosol Jet Printing for printed electronics rapid prototyping. In *2016 IEEE International Symposium on Circuits and Systems (ISCAS)*, pages 866–869, May 2016.

[53] C. Kaestle, J. Hoerber, F. Oechsner, and J. Franke. Prospects of wire bonding as an approach for contacting additive manufactured Aerosol Jet printed structures. In *2015 European Microelectronics Packaging Conference (EMPC)*, pages 1–6, Sep. 2015.

[54] M. I. M. Ghazali, S. Karuppuswami, S. Mondal, A. Kaur, and P. Chahal. Embedded Actives Using Additive Manufacturing for High-Density RF Circuits and Systems. *IEEE Transactions on Components, Packaging and Manufacturing Technology*, 9(8):1643–1651, Aug 2019.

[55] A. Elmogi, W. Soenen, H. Ramon, X. Yin, J. Missinne, S. Spiga, M. Amann, A. Srinivasan, P. De Heyn, J. Van Campenhout, J. Bauwelinck, and G. Van Steenberge. Aerosol-Jet Printed Interconnects for 2.5 D Electronic and Photonic Integration. *Journal of Lightwave Technology*, 36(16):3528–3533, Aug 2018.

[56] Y. Gu, D. R. Hines, V. Yun, M. Antoniak, and S. Das. Aerosol-Jet Printed Fillets for Well-Formed Electrical Connections between Different Leveled Surfaces. *Advanced Materials Technologies*, 2(11):1700178, 2017.

[57] F. X. Röhrl, J. Jakob, W. Bogner, R. Weigel, and S. Zorn. Bare Die Connections via Aerosol Jet Technology for Millimeter Wave Applications. In *2018 48th European Microwave Conference (EuMC)*, pages 1033–1036, Sep. 2018.

[58] M. Tonouchi. Cutting-edge terahertz technology. *Nat Photon*, 1(2):97–105, Feb 2007.

[59] P. H. Siegel. Terahertz technology in biology and medicine. *IEEE Transactions on Microwave Theory and Techniques*, 52(10):2438–2447, Oct 2004.

[60] M. C. Kemp, P. F. Taday, B. E. Cole, J. A. Cluff, A. J. Fitzgerald, and W. R. Tribe. Security applications of terahertz technology. *Proc.SPIE*, 5070:44 – 52, 2003.

[61] J. F. Federici, B. Schulkin, F. Huang, D. Gary, R. Barat, F. Oliveira, and D. Zimdars. THz imaging and sensing for security applications—explosives, weapons and drugs. *Semiconductor Science and Technology*, 20(7):S266, 2005.

[62] S. Biber, J. Schur, A. Hofmann, and L. P. Schmidt. Design of new passive THz devices based on micromachining techniques. In *The Fifth International Kharkov Symposium on Physics and Engineering of Microwaves, Millimeter, and Submillimeter Waves (IEEE Cat. No.04EX828)*, volume 1, pages 26–31 Vol.1, June 2004.

[63] A. E. Costley, K. H. Hursey, G. F. Neill, and J. M. Ward. Free-standing fine-wire grids: Their manufacture, performance, and use at millimeter and submillimeter wavelengths. *J. Opt. Soc. Am.*, 67(7):979–981, Jul 1977.

[64] P.A.R. Ade, A.E. Costley, C.T. Cunningham, C.L. Mok, G.F. Neill, and T.J. Parker. Free-standing grids wound from 5 μ m diameter wire for spectroscopy at far-infrared wavelengths. *Infrared Physics*, 19(5):599 – 601, 1979.

[65] N. Born, R. Gente, I. Al-Naib, and M. Koch. Laser beam machined free-standing terahertz metamaterials. *Electronics Letters*, 51(13):1012–1014, 2015.

[66] D. Jahn, M. Weidenbach, J. Lehr, L. Becker, F. Beltrán-Mejía, S. F. Busch, J. C. Balzer, and M. Koch. 3D Printed Terahertz Focusing Grating Couplers. *Journal of Infrared, Millimeter, and Terahertz Waves*, 38(6):708–716, Jun 2017.

[67] B. Zhu, S. Vanloocke, J. Stiens, D. De Zutter, A. Elhawil, C. De Tandt, and R. Vounckx. A novel 3D printed focusing probe in scattering-type scanning near-field millimetre amp; Terahertz wave microscope. In *Proceedings of the 5th European Conference on Antennas and Propagation (EUCAP)*, pages 745–748, April 2011.

[68] A. I. Hernandez-Serrano, M. Weidenbach, S. F. Busch, M. Koch, and E. Castro-Camus. Fabrication of gradient-refractive-index lenses for terahertz applications by three-dimensional printing. *J. Opt. Soc. Am. B*, 33(5):928–931, May 2016.

[69] A. Kaur, J. C. Myers, M. I. M. Ghazali, J. Byford, and P. Chahal. Affordable terahertz components using 3D printing. In *2015 IEEE 65th Electronic Components and Technology Conference (ECTC)*, pages 2071–2076, May 2015.

[70] K. Y. Park, N. Wiwatcharagoses, and P. Chahal. Wafer-level integration of micro-lens for THz focal plane array application. In *2013 IEEE 63rd Electronic Components and Technology Conference*, pages 1912–1919, May 2013.

[71] J. A. Byford, Z. Purtill, and P. Chahal. Fabrication of Terahertz Components Using 3D Printed Templates. In *2016 IEEE 66th Electronic Components and Technology Conference (ECTC)*, pages 817–822, May 2016.

[72] T. Kondo, T. Nagashima, and M. Hangyo. Fabrication of Wire-Grid-Type Polarizers for THz Region Using a General-Purpose Color Printer. *Japanese Journal of Applied Physics*, 42(4A):L373, 2003.

[73] A. Das, T. M. Schutzius, C. M. Megaridis, S. Subhechha, T. Wang, and L. Liu. Quasi-optical terahertz polarizers enabled by inkjet printing of carbon nanocomposites. *Applied Physics Letters*, 101(24):243108, 2012.

[74] K. Takano, T. Kawabata, C. F. Hsieh, K. Akiyama, F. Miyamaru, Y. Abe, Y. Tokuda, R. P. Pan, C. L. Pan, and M. Hangyo. Fabrication of Terahertz Planar Metamaterials Using a Super-Fine Ink-Jet Printer. *Applied Physics Express*, 3(1):016701, 2010.

[75] H. Kim, J. S. Melinger, A. Khachatrian, N. A. Charipar, R. C. Y. Auyeung, and A. Piqué. Fabrication of terahertz metamaterials by laser printing. *Opt. Lett.*, 35(23):4039–4041, Dec 2010.

[76] H. T. Yudistira, A. P. Tenggara, S. S. Oh, V. Nguyen, M. Choi, C. Choi, and D. Byun. High-resolution electrohydrodynamic jet printing for the direct fabrication of 3D multilayer terahertz metamaterial of high refractive index. *Journal of Micromechanics and Microengineering*, 25(4):045006, 2015.

[77] A. P. Tenggara, S. J. Park, H. T. Yudistira, Y. H. Ahn, and D. Byun. Fabrication of terahertz metamaterials using electrohydrodynamic jet printing for sensitive detection of yeast. *Journal of Micromechanics and Microengineering*, 27(3):035009, 2017.

[78] F. Cai, S. Pavlidis, J. Papapolymerou, Y. H. Chang, K. Wang, C. Zhang, and B. Wang. Aerosol jet printing for 3-D multilayer passive microwave circuitry. In *2014 44th European Microwave Conference*, pages 512–515, Oct 2014.

[79] F. Cai, Y. h. Chang, K. Wang, W. T. Khan, S. Pavlidis, and J. Papapolymerou. High resolution aerosol jet printing of D- band printed transmission lines on flexible LCP substrate. In *2014 IEEE MTT-S International Microwave Symposium (IMS2014)*, pages 1–3, June 2014.

[80] C. Oakley, A. Kaur, J. A. Byford, and P. Chahal. Aerosol-Jet Printed Quasi-Optical Terahertz Filters. In *2017 IEEE 67th Electronic Components and Technology Conference (ECTC)*, pages 248–253, May 2017.

[81] D. Jahn, R. Eckstein, L. M. Schneider, N. Born, G. Hernandez-Sosa, J. C. Balzer, I. Al-Naib, U. Lemmer, and M. Koch. Digital Aerosol Jet Printing for the Fabrication of Terahertz Metamaterials. *Advanced Materials Technologies*, 3(2):1700236, 2018.

[82] J. A. Hejase, P. R. Paladhi, and P. Chahal. Terahertz Characterization of Dielectric Substrates for Component Design and Nondestructive Evaluation of Packages. *IEEE Transactions on Components, Packaging and Manufacturing Technology*, 1(11):1685–1694, Nov 2011.

[83] M. Abt, A. Roch, J. A. Qayyum, S. Pestotnik, L. Stepien, A. Abu-Ageel, B. Wright, A. C. Ulusoy, J. Albrecht, L. Harle, J. Papapolymerou, and T. Schuelke. Aerosol-printed highly conductive Ag transmission lines for flexible electronic devices. *IEEE Transactions on Components, Packaging and Manufacturing Technology*, 8(10):1838–1844, Oct 2018.

[84] D.M. Pozar. *Microwave Engineering*. Wiley, 2004.

[85] M. I. M. Ghazali, K. Y. Park, J. A. Byford, J. Papapolymerou, and P. Chahal. 3D printed metalized-polymer UWB high-gain Vivaldi antennas. In *2016 IEEE MTT-S International Microwave Symposium (IMS)*, pages 1–4, May 2016.

[86] B. S. Cook and A. Shamim. Inkjet Printing of Novel Wideband and High Gain Antennas on Low-Cost Paper Substrate. *IEEE Transactions on Antennas and Propagation*, 60(9):4148–4156, Sept 2012.

[87] G. McKerricher, J. Gonzalez, and A. Shamim. All inkjet printed 3D microwave capacitors and inductors with vias. In *Microwave Symposium Digest (IMS), 2013 IEEE MTT-S International*, pages 1–3, June 2013.

[88] C. Mariotti, M. M. Tentzeris, and L. Roselli. Demonstration and charaterization of fully 3D-printed RF structures. In *Microwave Symposium (MMS), 2015 IEEE 15th Mediterranean*, pages 1–4, Nov 2015.

[89] F. Cai, A. Ç Ulusoy, and J. Papapolymerou. 2.4 GHz low cost low noise amplifier on flexible organic substrate. In *2013 Asia-Pacific Microwave Conference Proceedings (APMC)*, pages 270–272, Nov 2013.

[90] O. Azucena, J. Kubby, D. Scarbrough, and C. Goldsmith. Inkjet printing of passive microwave circuitry. In *Microwave Symposium Digest, 2008 IEEE MTT-S International*, pages 1075–1078, June 2008.

[91] D. C. Thompson, O. Tantot, H. Jallageas, G. E. Ponchak, M. M. Tentzeris, and J. Papapolymerou. Characterization of liquid crystal polymer (LCP) material and transmission lines on LCP substrates from 30 to 110 GHz. *IEEE Transactions on Microwave Theory and Techniques*, 52(4):1343–1352, April 2004.

[92] F. Cai, Y. H. Chang, K. Wang, C. Zhang, B. Wang, and J. Papapolymerou. Low-Loss 3-D Multilayer Transmission Lines and Interconnects Fabricated by Additive Manufacturing Technologies. *IEEE Transactions on Microwave Theory and Techniques*, 64(10):3208–3216, Oct 2016.

[93] M. Craton, J. A. Byford, V. Gjokaj, J. Papapolymerou, and P. Chahal. 3D Printed High Frequency Coaxial Transmission Line Based Circuits. In *2017 IEEE 67th Electronic Components and Technology Conference (ECTC)*, pages 1080–1087, May 2017.

[94] V. Gjokaj, P. Chahal, J. Papapolymerou, and J. D. Albrecht. A novel 3D printed Vivaldi antenna utilizing a substrate integrated waveguide transition. In *2017 IEEE*

International Symposium on Antennas and Propagation USNC/URSI National Radio Science Meeting, pages 1253–1254, July 2017.

[95] B. J. Kang, C. K. Lee, and J. H. Oh. All-inkjet-printed electrical components and circuit fabrication on a plastic substrate. *Microelectronic Engineering*, 97:251–254, 2012.

[96] M. I. Mohd Ghazali, S. Karuppuswami, S. Mondal, and P. Chahal. Embedded Active Elements in 3D Printed Structures for the Design of RF Circuits. In *2018 IEEE 68th Electronic Components and Technology Conference (ECTC)*, pages 1062–1067, May 2018.

[97] C. Oakley, P. Chahal, J. Papapolymerou, and J. D. Albrecht. Fabrication of X-band Oscillator on LCP Substrate Using Aerosol Printing. In *International Symposium on Microelectronics*, volume 2017, pages 000052–000055. International Microelectronics Assembly and Packaging Society, 2017.

[98] R. W. Johnson, J. L. Davidson, R. C. Jaeger, and D. V. Kerns. Silicon hybrid wafer-scale package technology. *IEEE Journal of Solid-State Circuits*, 21(5):845–851, Oct 1986.

[99] M. Gdula, A. Yerman, V. Krishnamurthy, and R. Fillion. The GE high density overlay MCM interconnect method solves high power needs of GaAs system design. In *1993 Proceedings Fifth Annual IEEE International Conference on Wafer Scale Integration*, pages 339–345, Jan 1993.

[100] M. Topper, K. Buschick, J. Wolf, V. Glaw, R. Hahn, A. Dabek, O. Ehrmann, and H. Reichl. Embedding technology-a chip-first approach using bcb. In *Proceedings 3rd International Symposium on Advanced Packaging Materials Processes, Properties and Interfaces.*

[101] W. Cheng, M. A. Beiley, and S. S. Wong. Membrane multichip module technology on silicon. In *Proceedings 1993 IEEE Multi-Chip Module Conference MCMC-93*, pages 69–73, May 1993.

[102] C. H. J. Poh, C. E. Patterson, S. K. Bhattacharya, S. D. Philips, N. E. Lourenco, J. D. Cressler, and J. Papapolymerou. Packaging Effects of Multiple X-Band SiGe LNAs Embedded in an Organic LCP Substrate. *IEEE Transactions on Components, Packaging and Manufacturing Technology*, 2(8):1351–1360, Aug 2012.

[103] F. Geng, X. Ding, and L. Luo. Study on a 3D packaging structure with benzocyclobutene as a dielectric layer for radio frequency application. In *2009 International Conference on Electronic Packaging Technology High Density Packaging*, pages 85–90, Aug 2009.

[104] J. Tang, H. Wang, X. Chen, W. Ning, G. Xu, X. Sun, and L. Luo. An mcm package process for 24 ghz driver amplifier using photosensitive bcb. In *2010 11th International Conference on Electronic Packaging Technology High Density Packaging.*

[105] J. A. Qayyum, M. Abt, A. Roch, A. C. Ulusoy, and J. Papapolymerou. Ultra wideband 3D interconnects using aerosol jet printing up to 110 GHz. In *2017 12th European Microwave Integrated Circuits Conference (EuMIC)*, pages 372–375, Oct 2017.

[106] M. T. Craton, J. D. Albrecht, P. Chahal, and J. Papapolymerou. A Chip-First Approach to Millimeter-Wave Circuit Packaging. *IEEE Microwave and Wireless Components Letters*, pages 1–3, 2019.

[107] R. Yang and G. Mao. Liquid crystal polymer for flexible circuits, June 11 2002. US Patent 6,403,211.

[108] P. I. Deffenbaugh, R. C. Rumpf, and K. H. Church. Broadband Microwave Frequency Characterization of 3-D Printed Materials. *IEEE Transactions on Components, Packaging and Manufacturing Technology*, 3(12):2147–2155, Dec 2013.

[109] Z. Zhai, L. Ma, Y. Jiang, Q. Xie, F. Zhang, X. Wu, and J. Gao. Giant photosensitivity of aC: Co/GaAs/Ag pn-metal junctions. *Optical Materials Express*, 5(11):2667–2674, 2015.

[110] H. J. Ng, J. Wessel, D. Genschow, R. Wang, Y. Sun, and D. Kissinger. Miniaturized 122 GHz system-on-chip radar sensor with on-chip antennas utilizing a novel antenna design approach. In *2016 IEEE MTT-S International Microwave Symposium (IMS)*, pages 1–4, May 2016.

[111] S. Pan, F. Caster, P. Heydari, and F. Capolino. A 94-GHz Extremely Thin Metasurface-Based BiCMOS On-Chip Antenna. *IEEE Transactions on Antennas and Propagation*, 62(9):4439–4451, Sep. 2014.

[112] W. T. Khan, A. Çağrı Ulusoy, G. Dufour, M. Kaynak, B. Tillack, J. D. Cressler, and J. Papapolymerou. A D-Band Micromachined End-Fire Antenna in 130-nm SiGe BiCMOS Technology. *IEEE Transactions on Antennas and Propagation*, 63(6):2449–2459, June 2015.

[113] V. Gjokaj, J. Papapolymerou, J. D. Albrecht, B. Wright, and P. Chahal. A Compact Receive Module in 3D Printed Vivaldi Antenna. *IEEE Transactions on Components, Packaging and Manufacturing Technology*, pages 1–1, 2019.

[114] V. Gjokaj, J. Papapolymerou, J. D. Albrecht, and P. Chahal. Design and Fabrication of Additively Manufactured Hybrid Rigid-Flex RF Components. *IEEE Transactions on Components, Packaging and Manufacturing Technology*, 9(4):779–785, April 2019.